AERODYNAMIC CONTROL USING DISTRIBUTED ACTIVE BLEED

A Dissertation
Presented to
The Academic Faculty

by

John Michael Kearney

In Partial Fulfillment
Of the Requirements for the Degree
Doctor of Philosophy in Mechanical Engineering

Georgia Institute of Technology
George W. Woodruff School of Mechanical Engineering

August 2015

AERODYNAMIC CONTROL USING DISTRIBUTED ACTIVE BLEED

Approved by:

Professor Ari Glezer, Advisor
School of Mechanical Engineering
Georgia Institute of Technology

Professor Marilyn Smith
School of Aerospace Engineering
Georgia Institute of Technology

Professor Mark Costello
School of Aerospace Engineering
Georgia Institute of Technology

Dr. Bojan Vukasinovic
School of Mechanical Engineering
Georgia Institute of Technology

Professor Marc K. Smith
School of Mechanical Engineering
Georgia Institute of Technology

Approved: June 26, 2015

Dedicated to my Jo

ACKNOWLEDGEMENTS

It is sometimes remarked that Professor Ari Glezer has two personas – one he embodies while inside the lab and one while outside. As his student, I have been fortunate to witness and learn from both. The first persona, marked by unquenchable curiosity and relentless drive, has taught me that perseverance begets results, whether through countless alpha-sweeps, grueling qualifying exams, manifold document revisions, or the distillation of ideas into experiments. With care, such effort can kindle into discovery. The second of his personas, recognizable from its wry wisdom and (sometimes nostalgic) stories, has taught me to never count a single moment as wasted. Thank you, Ari, for investing so much time as my advisor and for shaping my approach to life.

I am also indebted to my thesis committee for their time and their guidance in the direction of this research. I owe particular thanks to Professor Marilyn Smith for the insights she revealed through her (quite demanding) Unsteady Aerodynamics course. And to Dr. V.: thank you for your advice in everything from best LabVIEW coding practices to best comedy sketches to watch for a laugh. Your presence greatly enlivened my time in lab.

Throughout my tenure, the past and present members of the Fluid Mechanics Research Lab (FMRL) balanced the gravity of research with an atmosphere of friendship, energy, and optimism. Dr. Slava Yorish, thank you for teaching me the importance of careful, elegant design, and for sharing your interests with me. Dr. Pablo Hidalgo, thank you for your cheerful (nay, jingling) presence in lab. John Culp, thank you for the many ways in which you have stretched my mind – your passion for ingenuity has taught me to

constantly challenge the quality of my solutions. Dr. Dan Brzozowski, Dr. George Woo, Dr. Abe Gissen, and Dr. Michael DeSalvo, I have enjoyed learning so much from each of you and would have struggled endlessly had you not paved the way. Thank you for maintaining an excitement about fluid mechanics that is, after all, the reason we joined the FMRL in the first place. To Mark Simpson: we have filled many long years studying and struggling and sharing successes and failures together. Thank you for being a buoy for me in the ocean of grad school. Tom Boziuk and Tom Lambert, your inquisitive and sharp minds have been a pleasure to engage with, and lab would have been a far gloomier place without your reliable senses of humor. Sourabh Jha, Yuehan Tan, Zicheng Gong, Curtis Peterson, and Travis Burrows, thank you for bringing refreshing energy and new perspectives to lab. Continue to ask hard questions and demand quality from your work. Good luck to all!

I am so deeply grateful to my parents, Mary Grace, Noel, and Carla, and to my siblings for their unwavering support, encouragement, and love. Thank you all for counseling perseverance and helping me keep perspective. Finally, it is impossible to overstate the abundance of love and gratitude I have for Jordan, my wife, who has what seem to be lifetimes of wisdom and patience. You are cherished, and I am sure that whatever contributions I have made in this document would not exist without you.

TABLE OF CONTENTS

LIST OF TABLES

LIST OF FIGURES

SUMMARY

A novel approach for controlling the global aerodynamic loads on lifting surfaces using regulated distributed active bleed that is driven by pressure differences across the surfaces is investigated in wind tunnel experiments. The experiments focus on the flow mechanisms that govern the interaction between the bleed and the local cross flow over a wide range of pre- and post-stall angles of attack. Particle image velocimetry (PIV) and load cell measurements indicate that low momentum quasi-steady and time-periodic bleed [$C_\mu \sim O(10^{-4})$] lead to bi-directional deflections of the time-averaged vorticity layer and effect increases or decreases in lift, drag, and pitching moment. High-speed PIV and proper orthogonal decomposition (POD) of the vorticity flux show that the bleed engenders trains of discrete vortices that advect along the surface and are associated with a local instability that is manifested by a time-averaged bifurcation of the vorticity layer near the bleed outlets. The vortices advect over several convective times and alter the vorticity flux over the airfoil and thereby the aerodynamic loads. Active bleed is also investigated on a dynamically pitching airfoil (reduced frequencies up to $k = 0.42$) to study the effects of modulating the evolution of vorticity concentrations during dynamic stall. Time-periodic bleed mitigates adverse pitching moment behavior ("negative damping") that can precipitate structural instabilities while maintaining the cycle-average loads to within 5% of the base levels by segmenting the vorticity layer during upstroke and promoting early flow attachment during downstroke. The present investigations demonstrate that active bleed can be implemented for direct lift control, maneuvering, or stabilization of flexible aerostructures (airframes, flexible wings, and rotor blades).

CHAPTER I

INTRODUCTION AND LITERATURE REVIEW

This thesis focuses on investigations of the fundamental mechanisms of aerodynamic flow control using distributed active bleed and of its effects on the aerodynamic loads of static and dynamically pitching airfoils. To establish a context for this work, this chapter begins with a literature survey of passive and active flow control over static aerodynamic surfaces. The concept of distributed active bleed is then described. Then, a brief summary of relevant research on the flow physics of dynamically pitching airfoils is presented with particular emphasis on control techniques that mitigate the effects of dynamic stall. Finally, the thesis objectives and its organization are outlined.

1.1 Aerodynamic Flow Control

The traditional objective of flow control for external aerodynamics is to manipulate the energy and momentum of wall-bounded and free shear layers. The purposes are myriad: to augment lift, reduce drag, induce moments, suppress or enhance separation, amplify or eliminate instabilities, intensify vorticity concentrations, or initiate or delay transition to turbulence, to name a few. The spatial and temporal time scales of the induced changes in the flow due to actuation are just as diverse. This section situates the findings most relevant to the present work within that context; reviews of progress in this field can be found in, e.g., Lachmann (1961), Gad-el-Hak (2000), and Joslin and Miller (2009).

1.1.1 Manipulation of Vorticity Concentrations

Alteration of the production and shedding of vorticity concentrations by active flow

control has been explored for modifying aerodynamic loads without moving control surfaces in a number of earlier investigations. DeSalvo and Glezer (2007) and Brzozowski et al. (2008) demonstrated that surface-mounted hybrid actuators each consisting of a miniature obstruction [$h \sim \mathrm{O}(0.01c)$] coupled with a momentum source (e.g., synthetic jets) can be used to regulate the strength of trapped vorticity concentrations on the pressure and suction surfaces near the trailing edge of an airfoil and thereby enable bi-directional changes in the pitching moment. In a typical implementation, the vorticity is formed within a recirculating bubble that scales with the characteristic cross stream dimension of the obstruction and a local synthetic jet is used to vary the extent of recirculating flow downstream of the obstruction and regulate the advection of shed vorticity concentrations into the wake. The bi-directional actuation at the trailing edge alters the Kutta condition and the induced pitching moment. DeSalvo, Whalen, and Glezer (2010) later demonstrated the manipulation of vorticity concentrations over the flap of a high-lift configuration to achieve lift increases of ΔC_{L} up to 1.05. Here fluidic oscillators at momentum coefficients up to $C_{\mu} = 1.6\%$ produced a Coandă-like deflection of the outer flow over the extent of the flap, displacing the separation point towards the trailing edge and leading to significant flow attachment. Woo and Glezer (2013) utilized pulsed actuation [$\mathrm{O}(0.05T_{\mathrm{conv}})$] issuing $0.15c$ from the leading edge of an airfoil held statically at 20° to dramatically alter the accumulation and shedding vorticity concentrations. In this study, the high-momentum pulse severed the separated shear layer, causing it to roll into a vortex that scaled with the airfoil chord as it advected into the wake. Meanwhile, the vorticity layer upstream of the jet extended towards the trailing edge and resulted in a circulation increase of over 20%. Bursts of

successive pulses about one convective time scale (T_{conv}) apart increased circulation above 50% by the accumulated effect of the vorticity concentrations of each pulse.

1.1.2 Passive Porosity-Based Flow Control

The use of passive bleed for aerodynamic control of moving bodies by exploiting inherent pressure differences across their surfaces is not new and has been explored in a number of earlier investigations. In a typical application, fluid is bled from high- to low-pressure domains through porous surface segments using internal passages. The ensuing ejection or suction interactions with the outer flow can result in local modifications of pressure distribution and the flow over the surface, and, in some cases, lead to global changes in aerodynamic forces. Passive porosity using surface slots or perforations has been investigated since the 1920s (Page, 1921, Lachmann, 1921, 1924, Abbott, 1931; see Abbott and von Doenhoff, 1959). Weick and Shortal (1932), for example, demonstrated that one slot of width 0.15c located on the suction surface near the leading edge of a Clark-Y airfoil yielded significant improvements to post-stall lift performance ($\Delta C_{L,max} = 0.48$ relative to the baseline at $\alpha = 23°$). Passive porosity has since shown promise for a number of applications including reduction of base drag on bluff bodies (Tanner, 1975), mitigation of shock waves on transonic airfoils (Savu and Trifu, 1984), stabilization of Tollmien-Schlichting waves (Carpenter and Porter, 2001), tip-vortex control (Han and Leishman, 2004), control of flow separation (Kraushaar and Chokani, 1997, Krzysiak, 2008), and attenuation of roll oscillations (Hu, Wang, and Gursul, 2014).

Two applications of passive porosity that are of particular interest to the present investigations are control of aerodynamic forces for maneuvering and direct lift control (DLC). In extensive investigations of passive porosity (dubbed PassPorT) for alteration

of the aerodynamic forces on projectiles and aircraft surfaces, the characteristic dimensions of surface pores was selected to be small relative to the boundary layer thickness and less than half of the skin thickness (Frink, Bauer, and Hunter, 2002). Bauer and Hemsch (1994) alleviated asymmetries in aerodynamic forces on a tangent-ogive forebody using patches of porous surface sections (22% porosity with hole diameters less than 0.07% of the body length) to drive flow between high- and low-pressure domains through an internal plenum. The bleed effectively reduced the respective variations in normal and yaw force coefficients from 0.8 and ±2.0 for solid models to 0.1 and ±0.2, respectively. In a related numerical investigation, Hunter et al. (2001) demonstrated a passive porosity control system distributed over the nose and wing surfaces of a generic tailless fighter aircraft that was capable of generating linear variations in the longitudinal pitching moment and yaw force coefficients of up to -0.3 and ±0.05, similar to that of conventional control surfaces. Passive porosity was also investigated numerically for reduction of the unsteady lift force on an airfoil moving through a wake similar to the unsteady forces associated with rotor-stator interactions in turbomachinery (Tinetti et al., 2001). Here, porosity over a surface segment measuring 0.1c downstream of the leading edge on the suction surface coupled with porosity on different segments of the pressure surface resulted in attached flow and could reduce the magnitude of the unsteady lift by as much as 18% without significant losses in time-averaged performance. Krzysiak (2008) compared the performance of leading-edge air-jet vortex generators supplied by an external compressor to those that were "self-supplied" (i.e., the jet momentum was provided by the static pressure difference between upper and lower airfoil surfaces acting through a conduit) and concluded that the latter was capable of delaying stall and thereby

increasing lift, though to a lesser extent than the former. In this work, inlets to the self-supplying vortex generators were placed near the leading edge on the pressure side to exploit the nearby stagnation point, and outlets were set at pitch and skew angles of 30° and 60°, respectively, to promote the formation of streamwise vortices that mixed with the outer flow to enhance momentum transfer to the boundary layer, increasing C_L by up to 0.3 post-stall. The study also found that the presence of the surface orifices had no effect on the aerodynamic forces below stall.

Passive porosity has also been utilized for direct lift control (DLC), namely for control of the flight path and lift of an aircraft without altering its angle of attack, which is important in approach and landing, rapid maneuvers, and gust alleviation. Investigations of the effects of varying the location and shape of slot spoilers for DLC by Andrisani and Gentry (1972) achieved a reduction of 78% in lift by using bleed through a 0.03*c*-wide flap slot (an equivalent spoiling effect using conventional flaps requires a rapid 20° or larger deflection at significant power input). DLC flaps integrated into a twin-engine passenger aircraft showed that they were less effective at generating lift than predicted due to transient aerodynamic effects of the flap deflections, and concluded that DLC could benefit from faster actuation (Jategaonkar, 1993). More recently, Merat (2008) assessed the impact of DLC spoiler implementation on the handling qualities, landing performance, and ride comfort of an Airbus A380 and determined that a DLC system capable of generating ±0.1g in acceleration could reduce the standard deviations of the touchdown point and vertical velocity upon landing by 38% and 50%, respectively. These earlier investigations indicate that implementation of rapid DLC without the use of external control surfaces could result in enhanced performance. The present

investigations demonstrate the utility of controlled bleed for large variations in the aerodynamic loads of a lifting airfoil and indicate its potential suitability for DLC.

1.1.3 Flow Control using Active Porosity

Few studies of aerodynamic bleed have attempted to actively regulate the interactions between the bleed and the cross flow. Williams, El-Khabiry, and Papazian (1989) and Williams and Papazian (1991) introduced the method of unsteady base bleed by way of experiments on a hollow cone-cylinder forebody. In this work, a vibration exciter was used to pump fluid between between two small holes ($d/D_{\text{forebody}} = 0.08$) on the base and two on the cone at Strouhal numbers of $St_{\text{act}} = 0.4\text{-}0.6$ and momentum coefficients of 0.013-0.227 in an effort to mitigate asymmetric forces. At high angles of attack (30-60°), the unsteady bleed imparted symmetry on the vortices shed from the body, marked by a recirculating zone, and eliminated the strong tip vortex shed from the cone. It should be noted that unlike the active bleed approach presented in this thesis, the base bleed technique relies on the formation of unsteady fluctuating regions of fluid near the surface to effect flow control and lacks the ability to regulate the flow driven between bleed holes by surface pressure differences. In more recent efforts, Patel et al. (2003) and Lopera, Ng, and Patel (2004) perforated the fins of an axisymmetric munitions model with small holes (diameters were 1% of the chord) and integrated microfabricated microvalve arrays to enable reconfigurable patterns of porosity between surfaces. Perforations upstream of separation produced variations in the normal force coefficient of 0.1 over angles ranging from 0° to 20°, which was sufficient for steering. A later numerical investigation that sought to steer a small-caliber projectile by actively controlling transpiration through holes in its rear circumference concluded that pitching moments up to ±0.01 could be

obtained even at high angles of attack up to Mach numbers of $M_\infty = 2$ (Patil, Ng, and Patel, 2007). Although this control approach could in theory effect temporal changes in forces, the authors did not discuss any time-dependent results. Ho et al. (2003) developed electrostatically actuated 1 mm^2 check-valves that were integrated near the leading edge of a flapping MAV wing and actuated such that they were open during upstroke motion and closed during downstroke. The authors were able to manipulate the unsteady leading-edge vortex and reported increases of 31% and 17% in the time-averaged lift and thrust, respectively.

1.1.4 Distributed Active Bleed

Building upon the previous work discussed above, this thesis introduces a new approach to active porosity in which the time scale of the actuation may be continuously varied between quasi-steady and time-periodic with frequencies on order of the shear layer instability, i.e. $St_{act} \sim O(1)$. The bleed flow is engendered by pressure differences across lifting surfaces and driven between porous surface segments that are connected by an internal flow path, and it can be regulated using integrated low-power actuators (e.g., piezoelectric louvers). Owing to advances in rapid-prototyping fabrication techniques, the porous segments can be positioned nearly anywhere on the airfoil surface and in any orientation, enabling a wide range of bleed configurations that may be used in arbitrary combinations. The use of this approach for aerodynamic flow control is attractive because the mechanical energy that is necessary to drive the bleed is derived from the motion of the vehicle while the regulation requires little additional power. That the interaction between the relatively low-momentum bleed and the outer flow has strong effects on vorticity production, accumulation, and transport over aerodynamic surfaces

suggests its utility for manipulation and control of the evolution of unsteady vorticity concentrations that are associated with static stall (Kearney and Glezer, 2011, 2012a, 2012b, 2013a, 2013b) and dynamic stall (Kearney and Glezer, 2013a, 2013b, 2014a, 2014b) and therefore unsteady forces. Bleed's effectiveness in these areas will be investigated in detail in §3, 4, and 5.

1.2 Pitching Airfoil Aerodynamics

In 1935, Theodorsen introduced a general theory of aerodynamic instability by combining potential flow analysis and the Kutta condition to yield the aerodynamic forces on an airfoil oscillating in a uniform stream (discussed further in §5). Theodorsen argued that the reduced oscillation frequency k, a ratio between the oscillation rate and convective time ($k = \omega c/2U_\infty$), was a critical parameter in the development of circulation about the airfoil and in the inception of flutter. The reduced frequency therefore contributed significantly to excursions in aerodynamic loads relative to values measured at static angles. Leishman (2006) defines the following bounds of unsteadiness:

- $k = 0$. Static airfoil. The effective angle of attack relative to the free stream may be considered steady (as long as the flow over the airfoil is nominally steady).
- $0 \leq k \leq 0.05$. Flow is "quasi-steady," and the pitch dynamics do not significantly affect the aerodynamic loads for excursions well below the static stall angle.
- $0.05 < k < 0.2$. Flow is "unsteady" (or "quasi-unsteady"), and information regarding the airfoil's acceleration and the time-dependence of the velocity field is required to fully describe the aerodynamic loads.
- $k \geq 0.2$: "Highly unsteady." Detailed information about the airfoil's acceleration and apparent mass effects are required to accurately describe the forces that arise.

The analytical rationale for these boundaries stems from an order of magnitude consideration of the unsteady pressure coefficient equation derived from incompressible flow over a flat plate; this procedure will not be addressed here. Note that the regime boundaries listed above are approximate [e.g., McAlister, Carr, and McCroskey (1978) report a quasi-steady upper bound of $k = 0.004$ in pitching experiments on a NACA 0012 airfoil], and oscillation unsteadiness in the present investigation will be addressed in §5.1.

1.2.1 Dynamic Stall

When oscillations in pitch occur near or beyond the static stall margin, the airfoil experiences alternating flow attachment and separation (i.e., "dynamic" stall), resulting in highly unsteady and nonlinear aerodynamic loads which can induce unstable structural vibrations, severe torsion, and can precipitate flutter (e.g., Rainey, 1956, Johnson and Ham, 1972, Carta, Commerford, and Carlson, 1973, McCroskey, Carr, and McAlister, 1976, McCroskey, 1981). In practical realizations, time-dependent structural oscillations leading to flutter may arise in response to variations of the free stream conditions including transient gusts, periodic vortex shedding, or due to underdamped structural members. Dynamic stall and flow-induced structural vibrations can therefore severely limit the performance of maneuvering aircraft, horizontal- and vertical-axis wind turbines, rotary compressors and turbines, and even insect wings (Carr, 1988). Though a number of comprehensive reviews detail the flow physics of dynamic stall (e.g., McCroskey, 1982, Ericsson and Reding, 1988, Bousman, 2000, Lee and Gerontakos, 2004), the phenomenon encompasses sufficient unsteadiness, large-scale turbulent separated zones, and range of Reynolds and Mach numbers to render an exact analysis difficult to obtain (Leishman, 2006).

Among the many factors that produce dynamic loads during pitching that overshoot (and undershoot) their static counterparts, Ericsson and Reding (1988) identified two phenomena as critical through investigations of ramp-wise changes in angle of attack: the delay of flow separation during the upstroke motion, and the upstream migration of the separation point towards the leading edge that causes the formation and "spillage" of a large dynamic stall vortex. The former is due to time lag effects, which result in a phase difference between the static loads and the angle of attack (and are therefore quasi-steady), and transient boundary layer improvement effects, including the favorable pressure gradient developed by the upwardly accelerating wall (or "leading-edge jet"). The latter occurs as the airfoil stalls. With increasing angle, the dynamic stall vortex grows at the leading edge before advecting (or "spilling") at $U_{\text{celerity}} \sim 0.5U_{\infty}$ and producing peaks in the normal force and pitching moment after additional time lags. An earlier review by McCroskey (1982) concluded that the reduced oscillation rate k, the oscillation amplitude α_{A}, and the maximum angle of incidence α_{max} play critical roles in the evolution of the dynamic stall vortex and consequently in its impact on the aerodynamic loads. Based primarily on these parameters, a distinction may be drawn between "light" and "deep" dynamic stall. In light stall, the viscous zone scales with the airfoil thickness, and the forces and the pitching moment begin to exhibit hysteresis between the upstroke and downstroke motions of the oscillation cycle. In deep dynamic stall (typically initiated when $\alpha_{\text{max}} > \alpha_{\text{static stall}}$ and α_{A} or k is large), the shedding of the dynamic stall vortex results in a separated zone that scales with the airfoil chord, and C_{L}, C_{D}, and C_{M} may diverge far from their static values at a given angle.

An important consequence of the variations in C_{M} during the cycle is "negative

damping," which occurs when the airfoil extracts energy from the flow and pitch oscillations increase in amplitude unless restrained. Negative net damping over the cycle can promote aeroelastic divergence or quickly lead to flutter (e.g., Liiva, 1969, McCroskey, 1982, Leishman, 2006). Carta (1967) first related the work exchange between the airfoil and flow to the pitching moment through the two-dimensional damping coefficient,

$$E_\alpha = -\oint C_{\mathrm{M}} d\alpha \Big/ \pi a_A^2 \tag{1.1}$$

$E_\alpha > 0$ indicates suppressive or stable damping and is evident when the C_{M} versus α curve is traversed in a counterclockwise direction, i.e. the pitching moment is more nose-down during the upstroke motion than the downstroke and vice versa. In the present investigation (§5), the damping coefficient will be extensively used to characterize cycle performance in the absence and presence of bleed actuation.

1.2.2 Flow Control on Pitching Airfoils

Although significant strides have been made in the analysis of dynamic stall since the 1960s, it continues to impose the primary limitations on rotorcraft forward flight speed and pitch link loading (Raghav and Komerath, 2013, Gardner et al., 2014), on the load factors of maneuvering aircraft (Visbal, 2011, Marpu et al., 2014), and on the power extraction capabilities of horizontal- and vertical-axis wind turbines (Schreck and Robinson, 2002, Simão Ferreira et al., 2009). Therefore, a considerable number of numerical and experimental efforts have sought to mitigate its unfavorable effects, particularly negative damping and lift hysteresis, using passive and active flow control. Recent approaches to dynamic stall control using passive means focus primarily on manipulating the unsteady separated zone near the leading edge or affecting the pitching

moment directly via changes to the trailing edge. Martin et al. (2003) computationally and experimentally investigated the effects of a variable-droop leading edge on a VR-12 airfoil pitching between $0 < x/c < 0.25$ for k up to 0.1 and for $0.2 < M_\infty < 0.45$. By decreasing the suction peak associated with the formation of the dynamic stall vortex, the modified leading edge reduced the maximum drag and pitching moment by up to 63% and 37%, respectively, as well as eliminated negative damping that occurred on the baseline airfoil between $8° < \alpha < 18°$. Manipulation of the formation of the dynamic stall vortex was also demonstrated in experiments by Mai et al. (2008) by placing cylindrical leading-edge vortex generators less than $0.01c$ tall and $0.02c$ in diameter within $0.0017c$ from the leading edge on the pressure side of the airfoil. The vortex generators appeared to induce longitudinal vortices that suppressed the dynamic stall vortex, and at reduced frequencies (based on the full chord) up to 0.2 and $M_\infty = 0.31$, reduced the peak drag and nose-down pitching moment by up to 28% and 50%, respectively. Heine et al. (2013) extended this work by investigating several "disturbance" generator shapes placed near the same leading-edge pressure-side location as Mai et al. (2008) and reported up to a 96% improvement in damping due to the interaction of the weak counter-rotating vortices shed from the disturbances and the stronger dynamic stall vortex. Using a similar approach, Martin et al. (2008) fitted a "glove" over the leading edge of a VR-7 airfoil and investigated dynamic stall loadings with and without rectangular vortex generators. At k up to 0.1 and $M_\infty = 0.3$, the authors showed nearly complete removal of the nose-down peak in C_M during light and deep dynamic stall, although the approach lost effectiveness outside of a given range of M_∞. Combinations of leading-edge and trailing-edge modifications have also been experimentally and numerically investigated [e.g., Gurney

flaps (Chandrasekhara, Martin, and Tung, 2004, Joo et al., 2006) and deformable trailing edges (Andersen et al., 2009)] and shown to alleviate peak pitching moment and drag loads while reducing negative damping.

Ever-increasing performance goals, particularly for rotorcraft, have driven the development of advanced concepts for controlling aerodynamic loads (Carr et al., 1998) including active flow control approaches that modify the flow when desired and do not compromise performance otherwise (Gerontakos and Lee, 2006). A detailed parametric study undertaken by Greenblatt and Wygnanski (2001) investigated the effects of steady and oscillatory blowing near the leading edge for $0.05 < k < 0.3$ and over a range of light and deep pitch excursions. They observed that steady blowing could alternatively exacerbate lift hysteresis or (for momentum coefficients of $C_\mu > 3\%$) dramatically improve the maximum lift and drag performance, yet oscillatory blowing (at a nondimensional actuation frequency $F^+ = 0.6$ and $C_\mu = 0.1\%$) consistently improved maximum lift and reduced hysteresis. Similar findings using active bleed (albeit with reduced C_μ) will be presented in §5. The effects of steady and pulsed blowing were also assessed by Weaver, McAlister, and Tso (2004) using a VR-7 airfoil with a 3° trailing-edge tab. These authors found that steady blowing at $x/c = 0.25$ and high C_μ (over 50%) trapped a separation bubble near the leading edge during upstroke and inhibited the formation of the dynamic stall vortex, resulting in a re-shaping of the C_M versus α curve such that lift stall and moment stall (and consequently negative pitch damping) were eliminated. At $k = 0.05$ and $0° < \alpha < 20°$, pulsed blowing at $F^+ = 0.9$ slightly improved upon the peak lift near 18° and degree of reattachment on the downstroke compared to steady blowing at the same C_μ of 2.4%. Florea and Wake (2003) computationally

performed a parametric analysis of the effects of synthetic jet actuation during dynamic stall in which they varied the slot angle, slot width, and excitation level. This work focused on improving the stall and post-stall lift coefficients and found that during deep stall from $0.05 < k < 0.15$, unsteady blowing at $C_\mu \sim 0.5\%$ and $F^+ \sim 1$ with an optimized two-slot configuration near the leading edge resulted in up to a 140% increase in the cycle-averaged lift. Deliberate triggering of streamwise vortices from $x/c = 0.12$ using air-jet vortex generators from a pressurized plenum at $C_\mu \leq 1\%$ was shown by Singh et al. (2006) to delay the upstream migration of the separation point and thereby disrupt the strength of the leading edge vortex during upstroke into deep dynamic stall at $k = 0.1$. This resulted in reductions of the peak moment load up to 20% and closure of the lift hysteresis loop. Woo and Glezer (2013), discussed above in connection with separation control at static angles, also demonstrated transitory control of flow over a pitching airfoil ($k = 0.07$) using momentary high-momentum pulses. This work showed that a single pulse during the pitch cycle could delay the onset of dynamic stall by affecting the vorticity flux and thereby increase lift relative to the baseline throughout the entire cycle. Furthermore, bursts of up to 50 pulses were applied during the cycle to exploit the accumulation of vorticity for a sustained increase in lift (ΔC_L up to 10% relative to the baseline) and improvement to the damping coefficient ($\Delta E_\alpha = 0.05$). Finally, it is noted that non-fluidic approaches to actively controlling dynamic stall, such as plasma actuation (Post and Corke, 2006) and deployable leading-edge vortex generators (Le Pape et al., 2012), have also reported significant improvements in lift hysteresis and peak moment loads and, in some cases, done so without affecting the formation process of the dynamic stall vortex [e.g., using transient flap actuation (Feszty, Gillies, and Vezza,

2004, Gerontakos and Lee, 2006)].

The present investigation builds on the insights gained in the above studies by focusing control efforts on the manipulation of the formation and advection of the dynamic stall vortex and of the vorticity flux from the airfoil during the pitch cycle. It is shown in §5 that quasi-steady and time-periodic bleed actuation can be used to segment the separating vorticity layer during pitching, disrupting the buildup of the dynamic stall vortex, and to promote the formation of small-scale vortices that induce flow reattachment earlier during the downstroke than for the base flow, reducing lift hysteresis. This is accomplished using actuation on the order of the convective time and with flow rates up to an order of magnitude smaller than those discussed above.

1.3 Thesis Objectives and Structure

This thesis has two overarching goals: ***i.*** Characterize the flow control capabilities of distributed active bleed on lifting aerodynamic surfaces, and ***ii.*** Identify the flow mechanisms by which this control is realized. These goals are achieved by accomplishing the following three primary objectives:

- Investigate the effects and relevant time scales of quasi-steady and time-dependent bleed configurations on the aerodynamic loading of static airfoils.
- Elucidate the interactions between the bleed and cross flows, with particular emphasis on their effects on the production, advection, and shedding of vorticity concentrations.
- Investigate the effect of active bleed for control of dynamic stall on a dynamically pitching airfoil, with specific attention to the effects of the actuation on the formation and evolution of the dynamic stall vortex.

The thesis is organized as follows. The experimental setup and procedures for data acquisition and analysis are described in §2 and in Appendices A-C. A preliminary investigation of the time-averaged effects of quasi-steady and time-periodic bleed on a common general-purpose static airfoil model is presented in §3. Building on these findings, §4 explores the range of aerodynamic loads that can be affected using bleed on a static airfoil model, including a detailed investigation of the time-resolved interaction between the bleed and cross flows. In §5 this control approach is extended to a dynamically pitching airfoil to assess the interactions of the bleed with the unsteady flow and the dynamic stall vortex. Finally, §6 summarizes this work and presents the summary of the contributions and their discussion along with suggestions for future research.

CHAPTER II

EXPERIMENTAL SETUP AND PROCEDURES

2.1 Wind Tunnel and Traverses

The present investigations are conducted in a closed-return atmospheric wind tunnel driven by an 11.2 kW (15 hp) motor and 8-blade centrifugal fan and described in detail by Honohan (2003). The components of the wind tunnel facility are shown in a CAD rendering in Figure 2.1 and include the motor, centrifugal blower, heat exchanger, honeycomb, contraction (9.25:1 area ratio), test section (measuring 25 x 47 x 132 cm) having optical access from all sides, external traverse, and a commercial fog generator. The calibrated free stream speed ($3 < U_\infty < 35$ m/s) varies linearly with motor speed. An external chilled water supply with and a PID controlled valve maintains the test section at 71°F using a heat exchanger in the tunnel's settling section.

Two traverses were utilized during this work. In experiments using a Clark-Y airfoil (cf. §2.2.1 below), an aluminum traverse mounted on a 1.52 x 0.91 m (5′ x 3′) optical table surrounds the test section and supports two precision rotational stages for angle of attack adjustment (0.017° resolution), upon which load cells (cf. §2.4.1) are mounted. The Clark-Y airfoil assembly is secured to adapter plates on the load cell measurement surfaces for determination of aerodynamic loads. For experiments conducted on the static and pitching VR-7 airfoil (cf. §2.2.2), a steel traverse supports a pair of servomotors (0.44 N·m max torque, one on each side of the test section) and 10:1 gearboxes with augmented gearing to 20:1 via a belt system. The airfoil position and

trajectory during pitching experiments are specified in software and executed through a dedicated DAQ PC (cf. §2.4.1). Optical encoders (10,000 counts per revolution) provide angular position feedback to the servomotors through a PID controller designed for high bandwidth and accurate position tracking (250 μs update period).

2.2 Airfoil Models

Two airfoil models are used to investigate aero-effected bleed in the present work. The Clark-Y model is an efficient general-purpose airfoil section common for fixed-wing aircraft, propeller designs, and model-scale planes (Picirrillo, 2000), that may be appropriate for MAV or UAV-scale aircraft owing to its ease of manufacture (the pressure side is flat between $0.30 < x/c < 0.70$). The second airfoil model has a Boeing-Vertol VR-7 profile designed for high-lift rotorcraft and low drag at Mach numbers above 0.4 (Dadone, 1978). The use of two airfoil models in this investigation provides verification that the effects of active bleed are not geometry-limited and emphasizes the potential of bleed to effect changes in aerodynamic forces over a wide range of applications. The coordinates of the Clark-Y and VR-7 airfoil profiles are listed in Tables A.1 and A.2 in Appendix A, respectively.

2.2.1 Clark-Y Airfoil Model

The Clark-Y airfoil model has a 200 mm chord, 240 mm span, maximum thickness of $0.12c$ at $x/c = 0.30$, is hollow (except for a 3.64 mm-thick structural support running chordwise at mid-span), and has a nominal skin thickness of 4 mm. The model is fabricated using a lightweight thermoplastic stereolithography (SLA) resin designed to for rigidity (elastic modulus to density ratio is $E/\rho \approx$ 5-18) and dimensional stability of millimeter-scale features. The model skin includes a perforated grid of multiple spanwise

rows of slots through the pressure and suction surfaces as shown in Figure 2.2. The grid of slots is designed to maintain the structural integrity of the model while enabling rapid testing of various spanwise bleed configurations between high and low surface pressures by simply sealing any unused slots with smooth, thin tape (0.08 to 0.18 mm thick) that easily withstands the pressure differences across the surface of the airfoil. Each of the spanwise-segmented bleed slots measures 10 mm in the spanwise direction, and they are 3.6 mm apart. The slots are designed to minimize pressure losses as the bleed flow passes through them, and depending on the surface curvature, their streamwise opening and streamwise spacing vary between 2.5 and 3.8 mm and 1.5 and 5.0 mm, respectively (there are 802 surface ports in total). A magnified view of the bleed slots near the leading edge is shown in Figure 2.3.

Bleed flow is regulated using a spanwise array of six piezoelectric louvers (visible in Figure 2.2b and discussed in §2.3) that are flush-mounted in a recess within a removable section of the pressure surface between $0.59 < x/c < 0.84$. Each are attached (side by side) to the model and cantilevered at their aft (downstream) end (i.e., with the free end pointing upstream). Each louver is mounted using high-strength double-sided tape that covers their aft 6 mm streamwise section. The effects of the deflected louvers on the aerodynamic characteristics of the airfoil are assessed in the absence of bleed (i.e. when the airfoil is sealed). Figures 2.4a-c show the percent changes in lift [$\widetilde{C}_L = (C_L - C_{L,0})/C_{L,0}$], drag ($\widetilde{C}_D$), and pitching moment ($\widetilde{C}_M$) with fractional louver opening Λ relative to the base (sealed) airfoil over a range of angles of attack. These data show that the maximum changes in drag, lift, and pitching moment induced by the statically actuated louvers are 1.6%, 2.6%, and 3.3%, respectively, which, as will be

discussed in §3, are small compared to the induced changes in the presence of bleed. Acrylic fences (6.35 mm thick) are fastened to the model at its spanwise extents to minimize flow three-dimensionality (cf. Appendix B). Steel shafts in the *c*/4 axis extend from aluminum flanges that are attached to the fences out of the tunnel and are supported by adapter plates connected to the load cells (§2.4.1).

2.2.2 VR-7 Airfoil Model

The VR-7 airfoil model shares many structural features with the Clark-Y model (Figure 2.5), including a 20 cm chord, 24 cm span, maximum thickness of 0.12*c* at $x/c = 0.33$, and skin thickness of nominally 4 mm. For the results presented in §4 (where the airfoil is held at static angles of attack), the VR-7 model is mounted to the load cells and external traverse using steel shafts terminating at the spanwise ends of the airfoil and supported by the load cell adapter plates. In the oscillatory pitching experiments (§5), the torsional stiffness of the model is enhanced with a perforated precision steel shaft running spanwise through *c*/4. To balance the fore-aft weight distribution about *c*/4 and to facilitate flow field measurements under various conditions, a number of end fences of varying sizes are used with the VR-7 models. A perspective section view of the VR-7 model along with a magnified schematic of flow entering the pressure-side louvers are shown in Figures 2.6a-b. Surface ports near the leading edge of the VR-7 are contoured to direct bleed flow in the streamwise direction following its passage through the suction side skin (Figure 2.7). Each spanwise row of the VR-7 bleed grid is comprised of 16 ports each 10 mm wide, and their streamwise extent increases with streamwise distance from the leading edge from 2.0 mm (at $x/c = 0$) to 2.5 mm (at $x/c = 0.95$) for a total of 1,184 ports. Figures 2.8a-c show the variations with angle of attack of the changes in lift,

drag, and pitching moment relative to the base airfoil, respectively, for several fractional louver openings Λ. These data show that the extension of the louvers into the outer flow over the pressure surface results in minimal interference and changes in aerodynamic forces. The maximum changes in C_L, C_M, and C_D relative to the base airfoil that are induced by the louver actuation are 0.012, 0.003, and 0.005, respectively.

2.3 Louver Actuation

The louver actuators utilized in the present work are commercial piezoelectric reeds that measure 51 mm long by 38 mm wide and 0.76 mm thick. Six reeds are mounted side by side on the airfoil's pressure surface so that in the rest position they cover and seal the inlet bleed ports underneath (cf. Figure 2.2b) while the ports on the suction surface remain open to the internal volume within the airfoil. The louvers are each cantilevered along their downstream edges, and, when actuated, their tips are displaced away from the surface and regulate the inlet flow through the inlet ports underneath. The louvers are connected in parallel to a DC amplifier with an amplitude response of 200 V at 1 kHz [power of O(1 mW)]. Actuation waveforms are synthesized using the laboratory computer and can maintain the louvers at a fixed offset displacement from the airfoil surface and drive them time-dependently. In the present investigations, the louvers in the array are driven simultaneously by waveforms generated in software on the laboratory computer such that their displacement is spanwise uniform. As shown in Figure 2.9a, the displacement of the cantilevered louvers, characterized by the fractional opening Λ, varies linearly with the applied voltage (δ_{max} = 2.12 mm). Figure 2.9b shows that as the driving frequency approaches 70 Hz, a resonance peak results in tip displacements that are over four times the maximum static displacement. During pitching experiments,

time-periodic actuation is unsynchronized to the airfoil's motion.

2.4 Diagnostics and Data Acquisition

The aerodynamic loads on the airfoil during static and dynamic experiments are assessed using load cells that are mounted to the external traverse and support the weight of the model. Additional diagnostics, including flow field measurements using particle image velocimetry (PIV) and static pressure measurements, provide insight into the mechanisms that lead to changes in loading in the absence and presence of bleed actuation.

2.4.1 Force Measurement Method using Load Cells

Load Cells

Aerodynamic loads are measured using two monolithic aluminum strain-gage load cells with external amplifiers and signal conditioners (including full Wheatstone bridges) that are mounted between each spanwise edge of the airfoil model and the support frame and traverse (Figure 2.10) and thereby measure the total load. Each load cell has a reference face and a measurement face and detects loads by comparing the strain developed between them. Analog voltage signals from the strain-gages are decomposed using a factory-calibrated 6x6 matrix into forces along and torques about three orthogonal axes at rates up to 500 Hz. Two pairs of load cells are used in the present investigations. In the experiments using the Clark-Y model, the load cells' full-scale sensing range is 44.48 N in the x and y directions (corresponding to drag and lift in the airfoil reference frame, respectively) with a resolution of 0.011 N and 3.39 N·m about the z axis (corresponding to the airfoil pitching moment) with a resolution of 0.0085 N·m. In experiments using the VR-7 model, where dynamic motion results in higher peak loads, the load cells used have full-scale ranges of 111.20 N (with a resolution of 0.014 N) in x and y and

11.30 N·m about z (with a resolution of 0.0014 N·m). In the present experiments, the load cells' resolutions in aerodynamic loads (C_L and C_D) and moments (C_M) correspond to 0.002 and 0.001, respectively. The load cells' *x*-axes are aligned to the airfoil chordline so that changes in angle of attack require rotation of the load cells; however, all force and moment measurements in the present investigations are transformed to the wind tunnel reference frame (the transformation procedure is outlined in Appendix C).

Data Acquisition (DAQ) and Master Trigger

Experiment control and data acquisition are accomplished using PC-based custom LabVIEW and MATLAB routines along with a number of National Instruments (NI) components with embedded A/D and D/A converters. Analog inputs from the load cells, servomotor encoder positions, actuator voltage, camera status during PIV, and various synchronization triggers are typically sampled and/or generated at a rate of 4 kHz. A "master trigger" generated in real-time during pitching experiments outputs a TTL pulse when the airfoil crosses a specified angle of attack $\alpha(t) = \alpha_{mean} + \alpha_{amplitude} \cdot \sin(\omega t)$ (typically α_{mean}). The master trigger is used to track and synchronize measurements, e.g., for phase-averaging forces and phase-locking PIV. Phase-locking to multiple sources simultaneously is achieved by combining timing signals using off-the-shelf logic circuits including AND gates and operational amplifiers.

During pitch oscillations, load cell sampling initiates on the master trigger and runs continuously for the experiment's duration, typically at least 200 oscillation cycles (in the experiments conducted at static angles of attack, quantities are time-averaged over at least 20-60 s until the root-mean-square error reaches an asymptote). To minimize extraneous noise present in the facility (e.g., MHz-frequency EM emitted from the tunnel

motor drive and servo amplifiers), an 8th-order Butterworth low-pass filter is implemented in software (f_{cutoff} = 100 Hz) and applied to each of the sampled signals.

Data Reduction of Aerodynamic Loads

Determination of the aerodynamic loads is carried out in several stages. In the load cell reference frame (cf. Appendix C), equations of motion for the airfoil are (prime notation is dropped for clarity):

$$m\ddot{x} = F_{\mathrm{x_{aero}}} + mg\sin(\alpha) + R_{\mathrm{x}} \tag{2.1}$$

$$m\ddot{y} = F_{\mathrm{y_{aero}}} - mg\cos(\alpha) + R_{\mathrm{y}} \tag{2.2}$$

$$I\ddot{\alpha} = M_{\mathrm{z_{aero}}} - r \cdot mg\sin(\alpha) + R_{\mathrm{M_z}} \tag{2.3}$$

α is the angle between the free stream velocity and airfoil chordline, $\boldsymbol{R}$ (R_{x}, R_{y}) and R_{Mz} are the reaction force and moment, respectively, measured by the load cells, I is the model moment of inertia, r is the moment arm from the pitch axis to the center of mass, and the subscript *aero* denotes aerodynamic loads. In the present investigations, accelerations in the x and y directions are absent. Load cell measurements are first recorded in the absence of a free stream velocity (i.e. the wind tunnel is off) while the airfoil tracks a specified pitch trajectory $\theta(t) = \theta_{\text{mean}} + \theta_{\text{amplitude}} \cdot \sin(\omega t)$, where θ is a rotation angle based on a predetermined encoder position set such that $\theta(t) \equiv \alpha(t)$ in the presence of the free stream. In the absence of air flow in the tunnel, there are no aerodynamic loads, and the reactions measured by the load cells are:

$$R_{\mathrm{x_{off}}} = -mg\sin(\theta) \tag{2.4}$$

$$R_{\mathrm{y_{off}}} = mg\cos(\theta) \tag{2.5}$$

$$R_{\mathrm{M_{z,off}}} = r \cdot mg\sin(\theta) + I\ddot{\theta} \tag{2.6}$$

where the subscript "off" denotes the absence of air flow in the tunnel. In the presence of

air flow, the airfoil is commanded to repeat the prescribed pitch motion [i.e., $\alpha(t) \equiv \theta(t)$] while the load cells sample a record identical in size to the tunnel-off record. The difference between tunnel-on and tunnel-off load cell data is computed:

$$R_{\mathrm{x_{on}}} = -F_{\mathrm{x_{aero}}} - mg\,[\sin(\alpha) - \sin(\theta)] \tag{2.7}$$

$$R_{\mathrm{x_{on}}} = -F_{\mathrm{y_{aero}}} + mg\,[(\cos(\alpha) - \cos(\theta)] \tag{2.8}$$

$$R_{\mathrm{M_{z,on}}} = -M_{\mathrm{z_{aero}}} + I(\ddot{\alpha} - \ddot{\theta}) + r \cdot mg\,[\sin(\alpha) - \sin(\theta)] \tag{2.9}$$

Equations (2.7)-(2.9) indicate that the aerodynamic loads can be resolved if the pitch trajectory and acceleration in the absence [$\theta(t)$ and $\ddot{\theta}(t)$, respectively] and presence [$\alpha(t)$ and $\ddot{\alpha}(t)$] of air flow are nearly identical. In the present experiments, this is realized by tuning the high-bandwidth PID controller to track the commanded airfoil motion and acceleration as closely as possible for a given air speed and by phase-averaging the loads.

The precision of this approach is demonstrated using an example representative of the experiments discussed in §5 in which the airfoil is commanded to pitch sinusoidally between $14° < \alpha < 22°$ at a rate of 4 Hz (reduced frequency $k = \omega c/2U_\infty = 0.17$). In this case, the mean of the difference $|\,\alpha(t) - \theta(t)\,|$ phase-averaged over a 200 oscillation-cycle record is 0.01° and arises because aerodynamic loading on the model increases the motor torque required to track the position. This difference is small, and therefore the trigonometric terms on the RHS of Equations (2.7)-(2.9) nearly vanish, such that the load cell reactions $R_{\mathrm{x_{on}}}$ and $R_{\mathrm{y_{on}}}$ are equal to the aerodynamic forces along the x and y directions (in the load cell frame), respectively. Furthermore, the record mean of the phase-averaged difference $|\,\ddot{\alpha} - \ddot{\theta}\,|$ is 37.54°/s^2 (the signals are processed using a low pass Butterworth filter with $f_{\mathrm{cutoff}} = 200$ Hz to remove structural noise at 330 Hz), resulting in a maximum contribution of 0.003 N·m to $M_{\mathrm{z_{aero}}}$ in Equation (2.9). This contribution is

smaller than 3% of typical aerodynamic loads ($C_M \sim 0.1$) and is neglected. Therefore, $R_{x_{on}}$, $R_{y_{on}}$, and $R_{M_{z,on}}$ in Equations (2.7)-(2.9), respectively, are equal to the aerodynamic loads with estimated errors of less than 1%, 1%, and 3%. The loads are transformed to the wind tunnel coordinate frame (cf. Appendix C) to resolve the lift, drag, and pitching moment.

2.4.2 Pressure Measurements

The Clark-Y model is instrumented with 32 circumferentially-spaced static pressure taps about midspan (at locations specified in Table A.3 of Appendix A) that are connected through conduits embedded in the airfoil skin. Each SLA conduit is connected to a hypodermic stainless steel tube segment (1.1 mm OD) in an endplate at the spanwise edge of the airfoil and to flexible Tygon tube that is routed through the mounting shaft to an external high-speed pressure scanner. The resolution of the pressure measurements is better than 1.25 Pa, and the pressure readings are sampled at 100 Hz and averaged over at least 50 s.

2.4.3 Flow Field Measurements using Particle Image Velocimetry (PIV)

The flow over the airfoil's suction surface and in its near wake is measured in the cross stream plane using low- and high-speed (time-resolved) planar PIV. The low-speed system is primarily used to acquire phase-locked measurements while the high-speed system is used to elucidate the evolution of vortical structures that are not fully locked to the airfoil's motion (such as the formation of the dynamic stall vortex). A typical PIV configuration is shown schematically in Figure 2.11. These systems and the corresponding post-processing routines are described in this section.

Low-speed PIV System

The low-speed PIV system consists of a TSI MiniLase III Nd:YAG laser (532 nm, 50 mJ peak energy per pulse, 15 Hz maximum firing rate, 5-7 ns pulse width) and commercially available LaVision PIV components, including an CCD camera (1600 x 1200 pixel, 14-bit resolution), DaVis software, a programmable timing unit, 5 x 5 cm and 20 x 20 cm calibration plates, and a Scheimpflug adapter for perspective correction. The laser is focused into a 1-2 mm thick sheet using spherical and cylindrical optics mounted to the optical table and illuminates fog particles (nominally 0.25-0.60 μm in diameter) in the wind tunnel test section produced by a commercial theatrical fog dispenser. For calibration, the image plane of the camera is aligned using the calibration plate and laser sheet, and a perspective correction algorithm is applied using the DaVis software. Typical time intervals Δt between frames in the experiments presented here range from 20 to 75 μs depending on the field of view and magnification.

The experimental uncertainty inherent in the PIV system is estimated by comparing measurements of the free stream velocity made with PIV to measurements from a pitot-static tube (cf. §2.1). For this, a 70 mm x 90 mm domain in the middle of the tunnel center-plane and upstream of the airfoil is interrogated (with a magnification of 16 px/mm) at three tunnel speed settings (15, 20, and 25 m/s). Three hundred image pairs are time-averaged at each speed to ensure convergence of the time-averaged data. The velocity magnitudes $|V|$ computed from spatial averages of the streamwise (u) and cross stream (v) components at 15, 20, and 25 m/s differ by 0.9, 0.4, and 0.7% from the pitot-static measurements. The respective spatial-averaged RMS fluctuations of $|\vec{V}|$ at 15, 20, and 25 m/s are 0.3% , 0.2%, and 0.2 m/s. Note that these RMS levels account for

both the uncertainty of the PIV measurements and the turbulent fluctuations in the free stream.

High-speed PIV System

The high-speed PIV system consists of a Photonics Nd:YLF laser (527 nm, 25 mJ peak energy per pulse, 0-10 kHz firing rate, 200-250 ns pulse width), a Vision Research Phantom v12.1 high-speed CMOS camera (1280 x 800 pixel, 12-bit resolution), and a high-speed LaVision PTU. The high-speed PIV system shares components with the low-speed system. In the present investigations, high-speed measurements are obtained at 2,000 frames per second.

PIV Processing

All velocity fields are computed using DaVis software which uses a standard double-frame FFT cross-correlation method (e.g., Raffel, Willert, and Kompenhans, 1998), and the specific parameters tend to vary with the magnification, surface reflections, and laser intensity. Typically the contrast of particles in the raw camera images is enhanced by subtracting the average (or minimum) pixel intensity from the data set at each spatial location in the frame. A mask is applied if necessary to remove reflections from the airfoil's surfaces. The cross-correlation algorithm is applied in multiple passes over incrementally smaller interrogation windows (e.g., 32 x 32 pixels to 16 x 16 pixels, with a 50% overlap) with a circular Gaussian weighting function for increased accuracy. Spurious vectors are rejected based on correlation peak ratios ("Q ratio" typically > 3), RMS thresholds, and comparison to neighboring points.

This process is demonstrated in Figure 2.12 with a sample set of time-resolved PIV taken in flow over the VR-7 airfoil at $\alpha = 16°$ and with bleed actuation. Figure 2.12a-b

show each raw camera frame, and Figure 2.12c-d show the result of subtracting the set average particle intensity at each point. The particles in these frames are cross-correlated as described above to yield a field containing 17,441 vectors (Figure 2.12e). The present investigations make extensive use of time-averaged and time-resolved PIV vector fields to compute the (spanwise) vorticity $\vec{\omega} = \nabla \times \vec{V}$. This is accomplished using a MATLAB routine adapted from Brzozowski (2011) which uses the local circulation in combination with Stokes' Theorem:

$$\Gamma = \oint \vec{V} \cdot d\vec{l} = \iint_A \nabla \times \vec{V} dA = \iint_A \vec{\omega}\, dA \tag{2.10}$$

The routine relies on each vector in the field having a small characteristic area defining its proximity to neighboring points, $dA = dx\, dy$, such that the magnitude of the vorticity may be estimated as $|\vec{\omega}| = \Gamma/A$. Figure 2.12f shows distributions of velocity vectors and spanwise vorticity concentrations derived from the vector field in Figure 2.12f as well as a mask defining the edges of the airfoil. Throughout the thesis, PIV data will be presented as in Figure 2.12f.

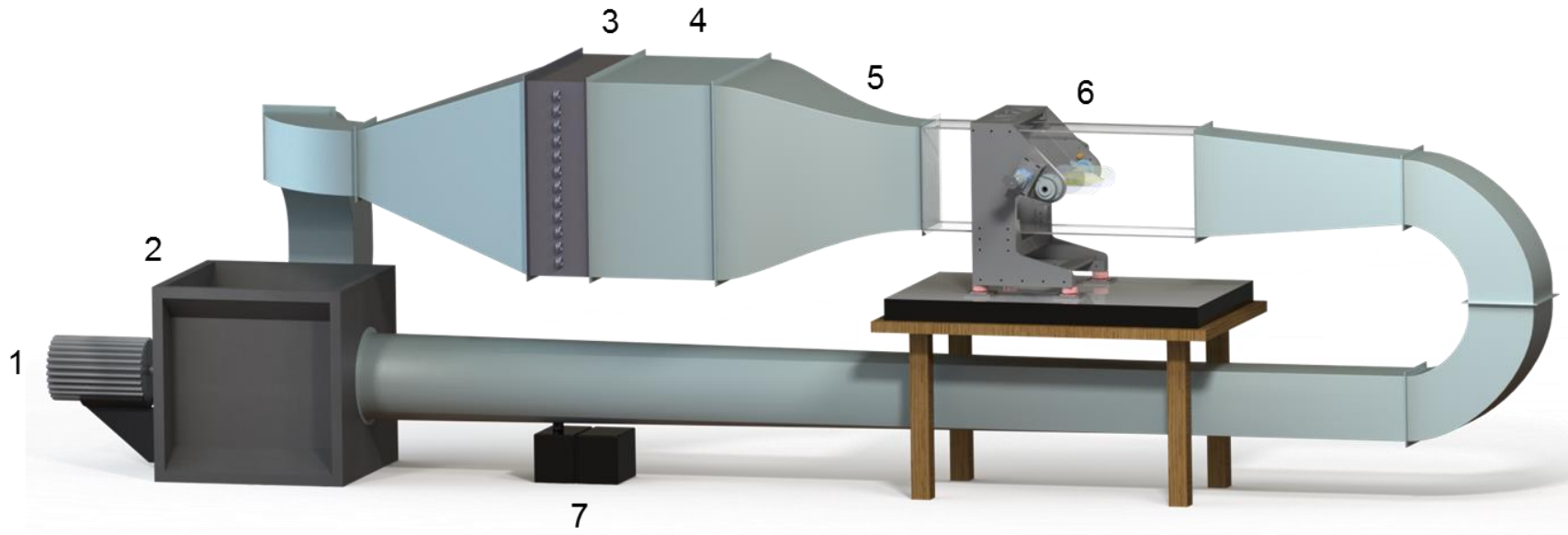

Figure 2.1. Schematic of closed-return wind tunnel facility, including motor (1), centrifugal fan (2), heat exchanger (3), settling section (4), contraction (5), test section and traverse (6), and PIV particle seeder (7).

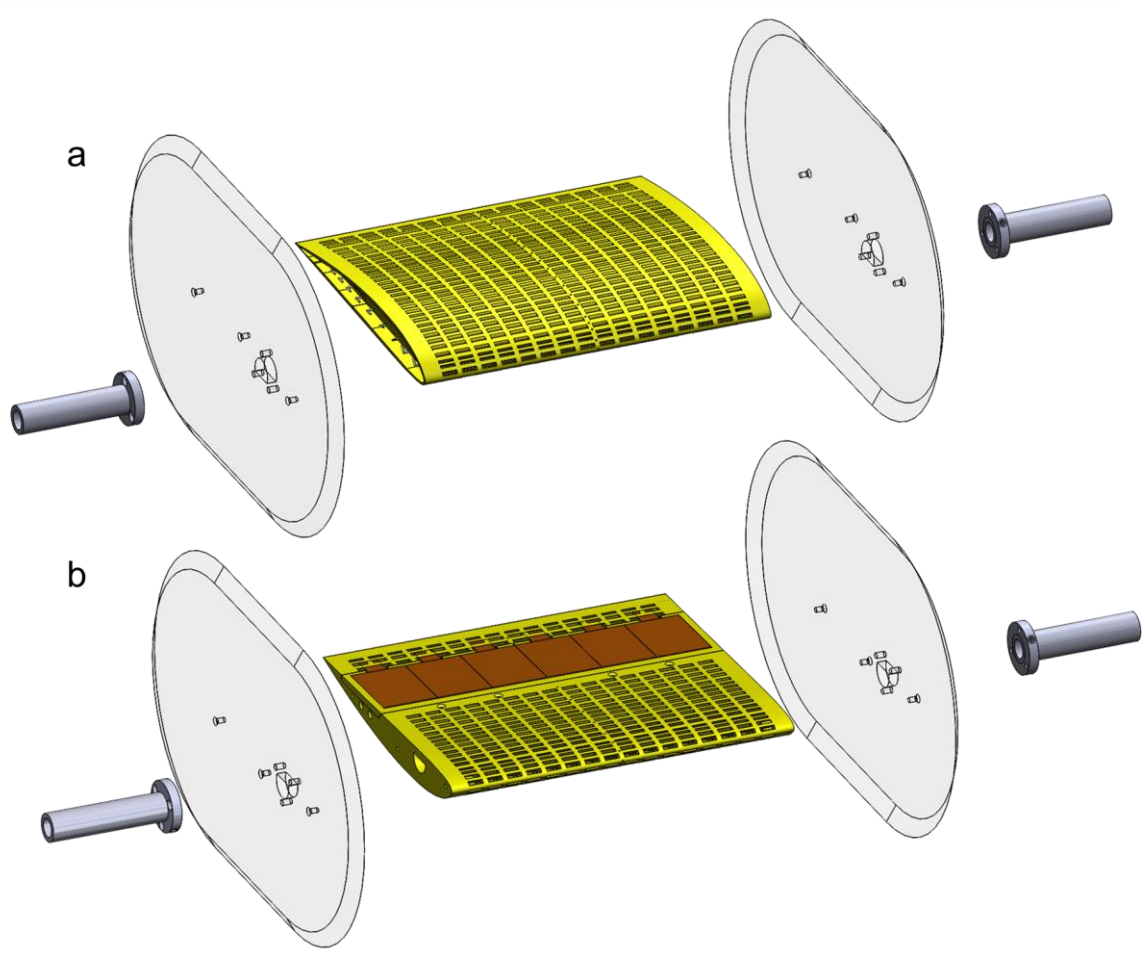

Figure 2.2. Perspective exploded view of the Clark-Y airfoil from above (a) and below (b) showing the bleed surface grid, the end fences, the mounting shafts, and the spanwise array of piezoelectric louvers (brown).

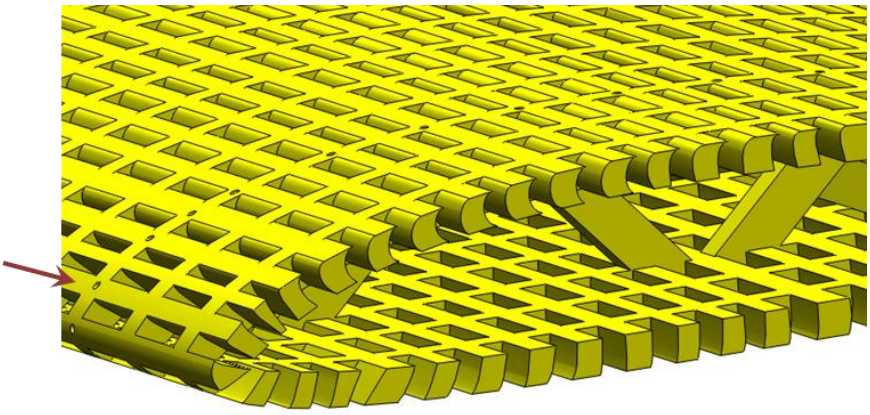

Figure 2.3. Perspective section view of the Clark-Y airfoil showing bleed slots on the suction and pressure surfaces near the leading edge. The chordwise structural support inside the airfoil and the pressure taps (marked with an arrow) on the mid-span are visible.

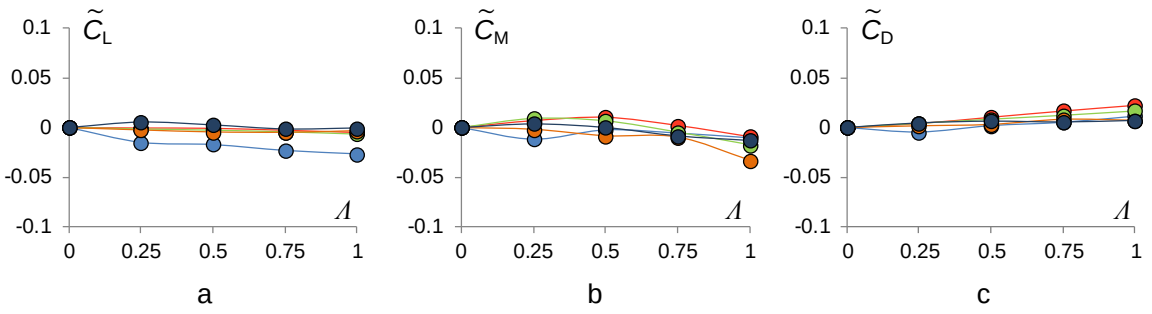

Figure 2.4. Effects of static louver actuation on aerodynamic forces in the absence of bleed. Fractional differences relative to the base airfoil of C_L (a), C_M (b), and C_D (c) for $\alpha = 4°$ (●), 8° (●), 12° (●), 16° (●), and 20° (●).

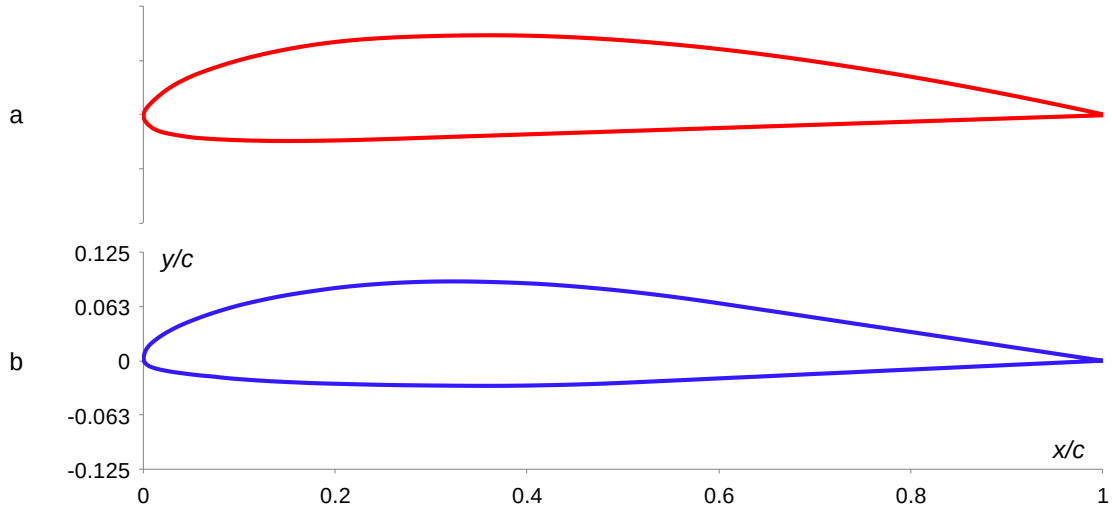

Figure 2.5. Profiles of the Clark-Y (a) and VR-7 (b) airfoils. Coordinates are listed in Appendix A.

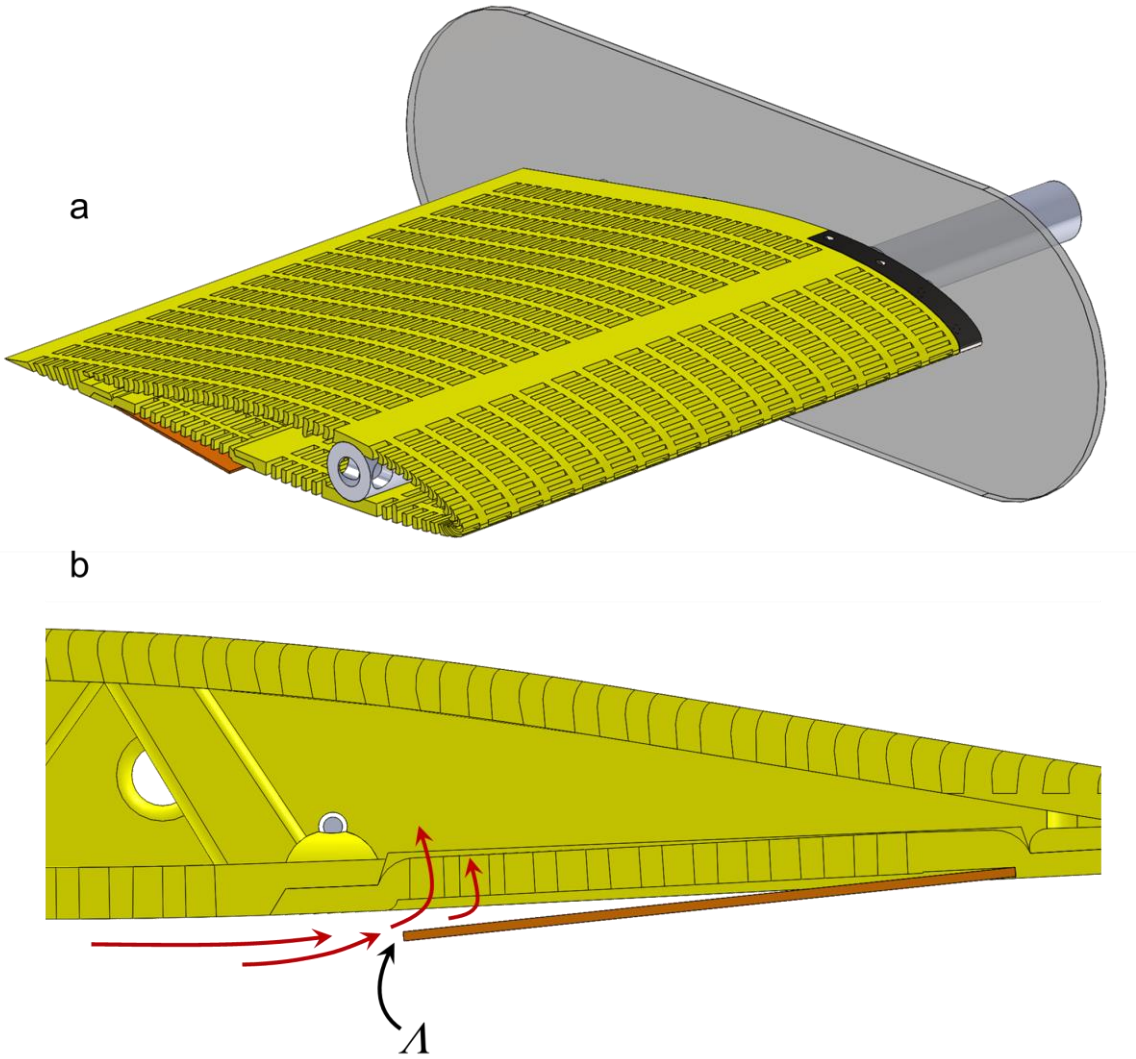

Figure 2.6. Section views of the VR-7 airfoil model: (a) bleed ports, pressure-side piezoelectric louvers (opening exaggerated), and perforated support shaft through *c*/4, and (b) magnified schematic view of the inlet bleed flow on the pressure-side.

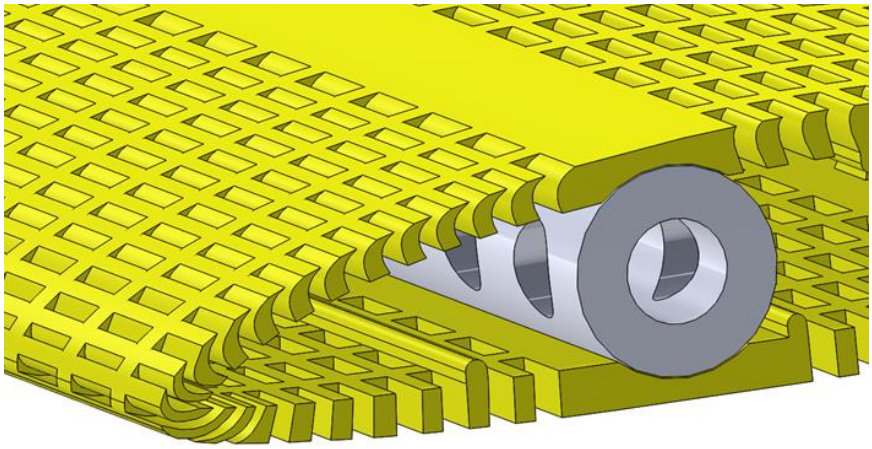

Figure 2.7. Perspective section view of the VR-7 airfoil showing the curvature of the leading edge bleed slots and the perforated support shaft.

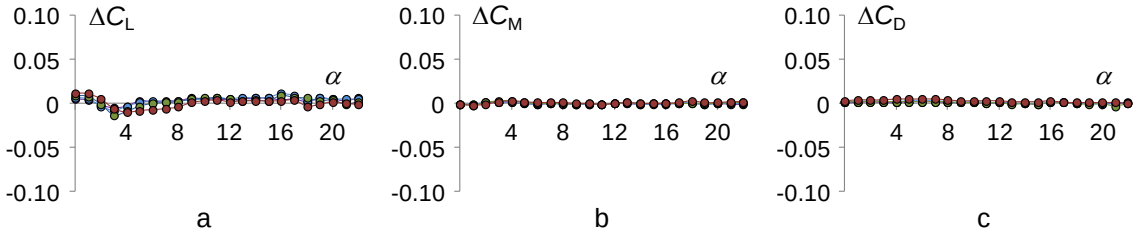

Figure 2.8. Variations in C_L (a), C_M (b), and C_D (c) with respect to baseline airfoil due to static louver actuation in the absence of bleed: Λ = 0.25 (●), 0.5 (●), 0.75 (●), and 1 (●).

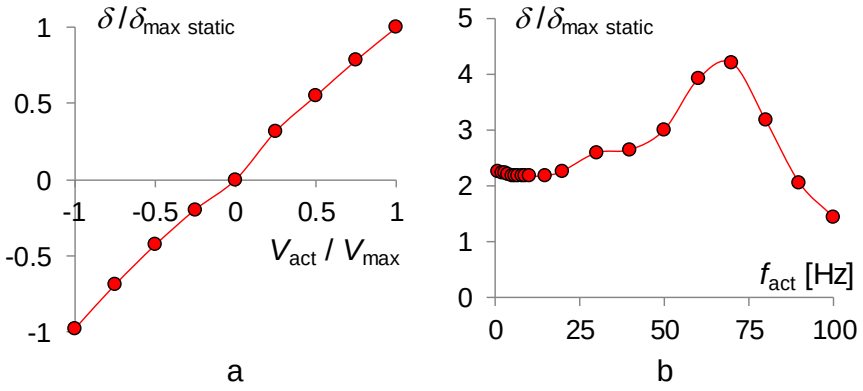

Figure 2.9. Variation of louver tip displacement with actuation voltage (a) and actuation frequency (b).

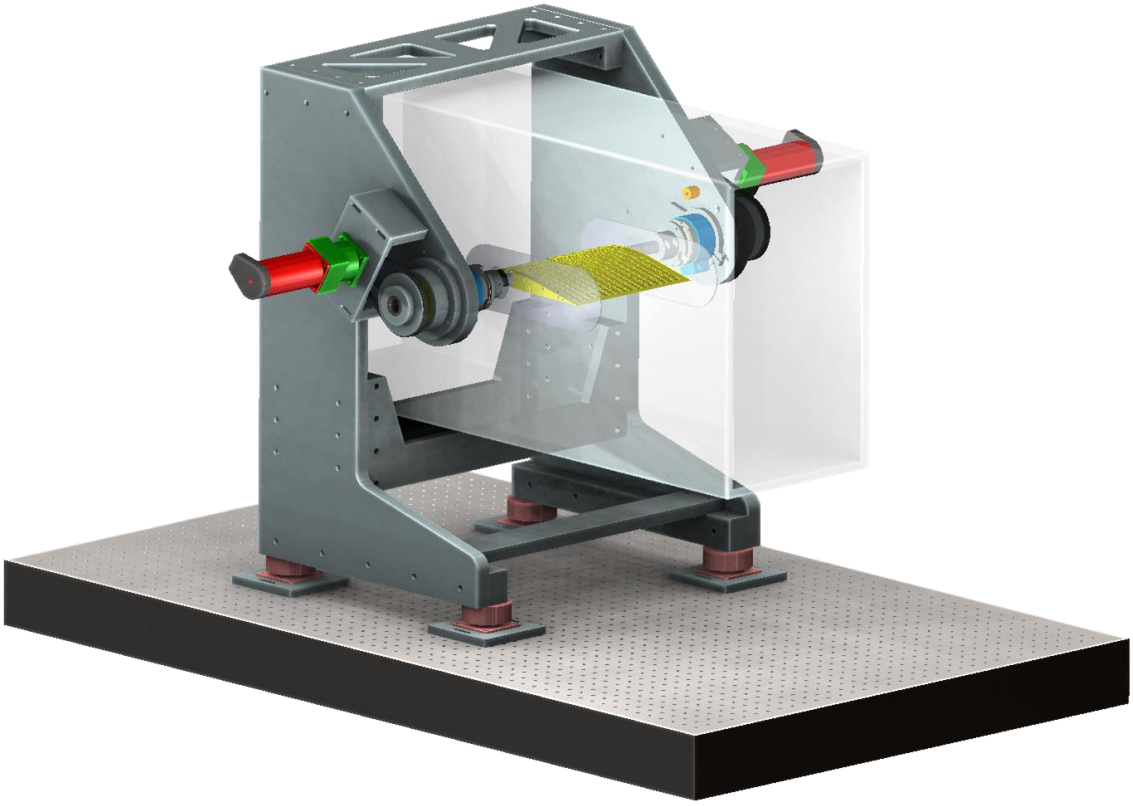

Figure 2.10. CAD rendition of the VR-7 airfoil (yellow), test section, and traverse. Load cells (blue) are mounted in-line with the *c*/4 axis and attached to the servomotors (red) and gearboxes (green) via pulleys. The traverse structure is mounted to an optical table using shock absorbers.

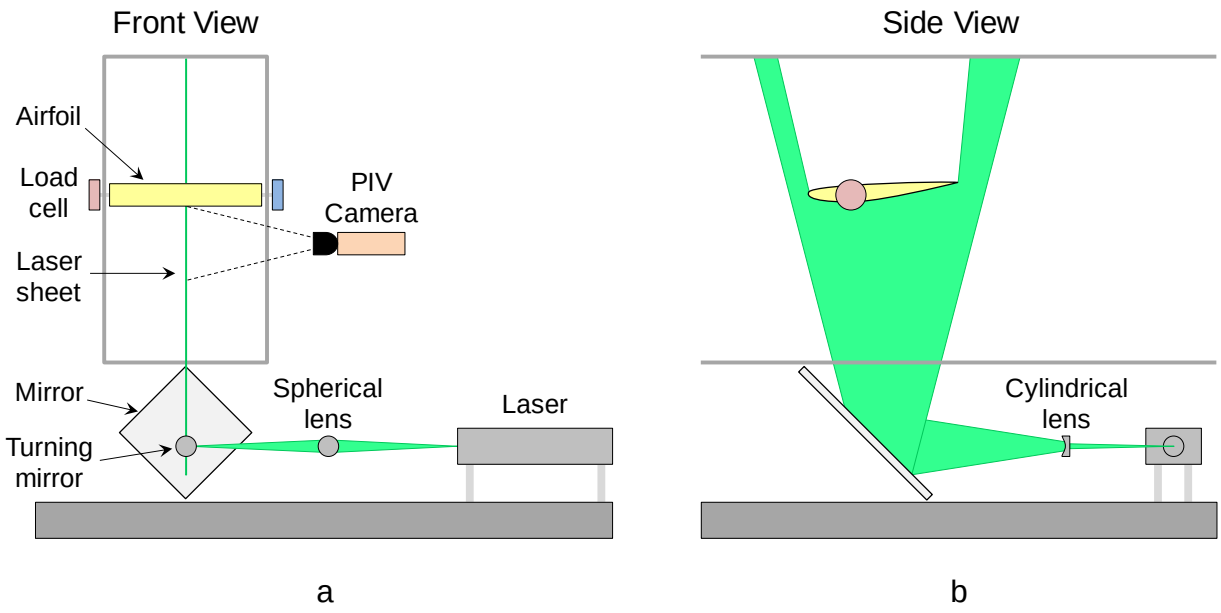

Figure 2.11. Streamwise front view (a) and side view (b) of a typical PIV setup in the present investigations. The airfoil is mounted upside down in the wind tunnel for measurements of the flow over the suction surface.

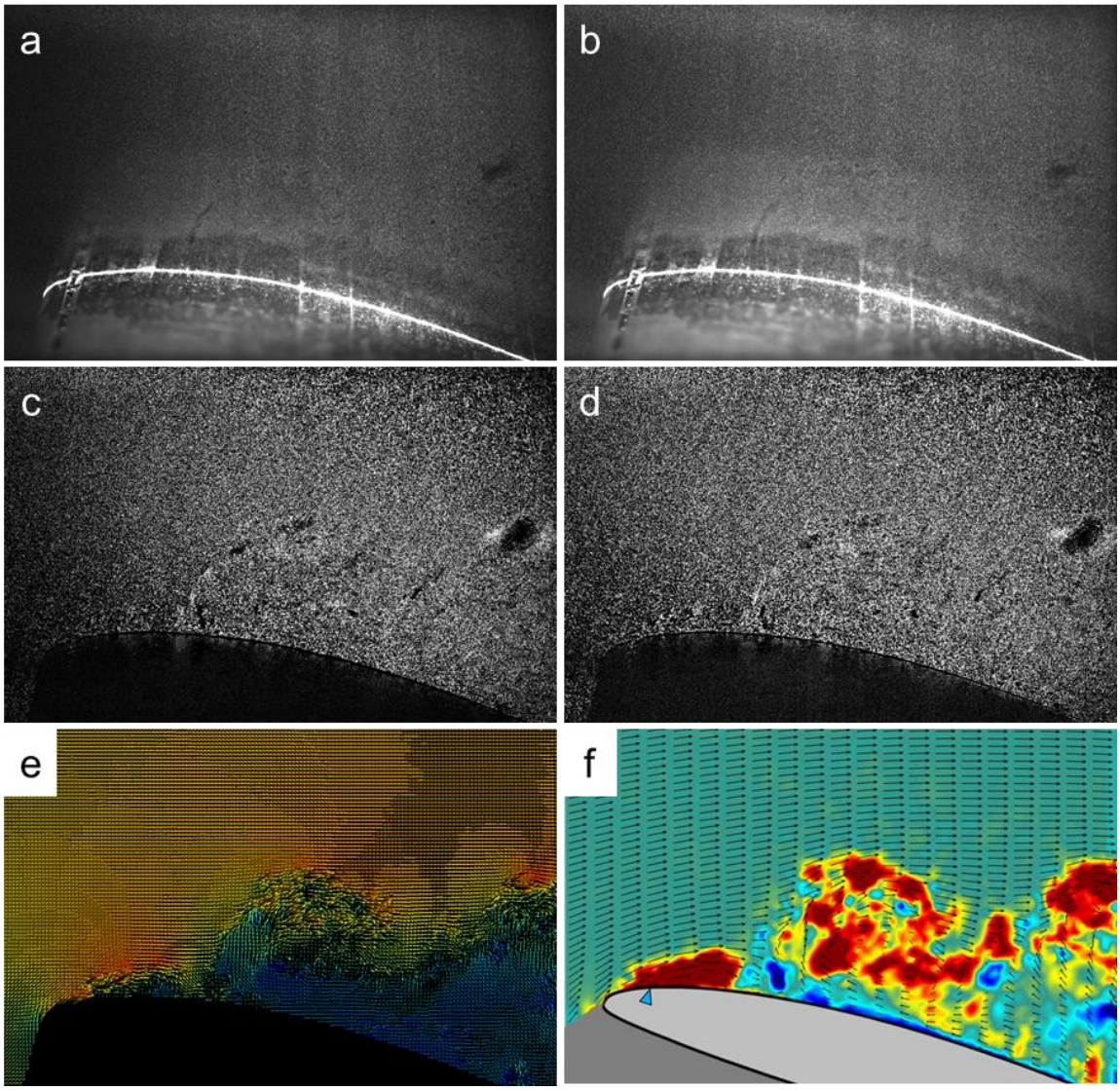

Figure 2.12. Sample PIV image-processing sequence showing instantaneous images of flow over the VR-7 airfoil ($\alpha = 16°$) with time-periodic bleed actuation: first and second frames (a, b) of a raw PIV image pair; results of image subtraction (c, d); vector field in DaVis (e); and distributions of velocity vectors and spanwise vorticity concentrations computed in MATLAB (f).

CHAPTER III

PRELIMINARY EVALUATION OF ACTIVE BLEED ON A COMMON FIXED-WING AIRFOIL MODEL

This chapter presents a preliminary investigation of the effects of active bleed on a general-purpose airfoil model (Clark-Y, cf. §2.2.1). The section begins by evaluating the range of control authority on the aerodynamic loads using quasi-steady bleed effected near the airfoil's leading edge. It is shown that quasi-steady and time-periodic bleed can be utilized to control separation and significantly affect the vorticity layer over the airfoil. The effects of the bleed on the static pressure distribution and airfoil's performance are also evaluated.

3.1 Quasi-Steady Bleed Actuation

As shown in §2.2.1, bleed actuation is applied through two spanwise arrays of ports on the suction side of the Clark-Y airfoil near its leading edge ($0.03 < x/c < 0.07$, $Re_c = 190{,}000$), where the flow through the inlet ports on the pressure side near the trailing edge is regulated by piezoelectrically-operated louvers (cf. Figures 2.3 and 2.4). The resulting modification of the aerodynamic loads for the base (smooth) airfoil and for several (static) openings of the louver actuators ($\Lambda = 0$, 0.25, 0.5, 0.75, and 1) are shown in Figures 3.1a-c. These data show that although the bleed affects the loads over the entire range $0° < \alpha < 22°$, for this streamwise location of the bleed ports, the actuation is most pronounced for $8° < \alpha < 20°$ (other bleed locations can significantly affect the aerodynamic loads at lower angles of attack). In fact, even the presence of open bleed

ports on the suction surface ($\Lambda = 0$) affects the loads due to local changes in suction and the interaction of the outer flow with the fluid within the airfoil's cavity that results in alteration of the boundary layer (as discussed further in connection with Figure 3.3). The presence of bleed leads to regulated reduction in lift relative to the base airfoil that typically increases in magnitude with the bleed flow (Figure 3.1a). The maximum reduction, $\Delta C_L = 0.71$ (46% relative to the base airfoil), is attained at $\alpha = 16°$. For a given bleed flow, the increase in angle of attack results in an apparent loss of suction that is similar to the effect of partial, premature stall due to the displacement of the surface boundary layer where the angle of attack at which this effect commences decreases with increasing bleed flow rate. Clearly, any lift magnitude within the domain of influence of the actuation can be realized over a range of angles of attack. As shown in Figure 3.1b, these changes in C_L are also accompanied by significant changes in C_M. This bleed configuration leads to a small nose-up pitching moment relative to the base airfoil for all bleed levels up to $\alpha = 8°$, and actuation at higher angles primarily leads to a stronger nose-down (negative) moment with a maximum magnitude of $\Delta C_M = 0.06$ at $\alpha = 14°$, or 85% of the base value. It is also noted that, over the range $10° < \alpha < 12°$, actuation can yield a nose-up (e.g. $\Delta C_M = 0.01$ at $\alpha = 10°$ with $\Lambda = 0.5$) or nose-down (e.g. $\Delta C_M = -0.04$ at $\alpha = 10°$ with $\Lambda = 1$) moment relative to the base airfoil, which allows a degree of maneuvering control based solely on bleed flow. The bleed is also accompanied by a small increase in C_D (maximum $\Delta C_D = 0.10$ relative to the base airfoil at $\alpha = 12°$).

The control authority of quasi-steady bleed is further elucidated by considering the variation of aerodynamic forces with the fractional louver opening. Figures 3.2a-c shows

the increments of C_L, C_M, and C_D with Λ relative to $\Lambda = 0$, respectively, for louver openings ranging from $0 < \Lambda < 1$ for $8^o < \alpha < 22^o$ where the dashed lines depict the extremum at each angle α. While the quasi-steady bleed produces a continuous reduction in lift up to nearly $\Delta C_L = -0.2$ at $\alpha = 8°$ (relative to $\Lambda = 0$), the primary actuation effectiveness is within a range of angles that approach and exceed the static stall angle ($\alpha = 18°$). In the range $12° < \alpha < 18°$, an increase or decrease in Λ can decrease or increase the lift, respectively, by up to nearly $\Delta C_L = 0.5$ (relative to $\Lambda = 0$). These data also indicate that the magnitude of the rate of change of C_L with Λ decreases as Λ is increased (e.g., at $\alpha = 18^o$, $dC_L/d\Lambda = -0.26$, -0.19, -0.17, and -0.15 for $\Lambda = 0.25$, 0.5, 0.75, and 1, respectively). Therefore, the (quasi-steady) $dC_L/d\alpha$ may be either increased or decreased simply by varying the bleed intensity. For example, during a quasi-steady maneuver from $\alpha = 12°$ to 16°, the actuation level Λ may be varied from 0.5 to 0.25 to produce an invariant lift decrement ($\Delta C_{L,\Lambda=0} = -0.21$ across this range). On the other hand, a sharp *relative* increase in lift may be achieved within the range $16° < \alpha < 20°$ by actuating at $\Lambda = 1$ ($\Delta C_L = +0.4$). Therefore, the level of C_L may be tailored in flight (as α is varied) simply by varying Λ. As α increases beyond 18°, actuation produces a monotonic and nearly linear decrease in lift although the magnitude of the variations decreases compared to pre-stall operation.

As with C_L, Figure 3.2b shows that varying the actuation at a given angle can also generate nearly-continuous nose-up or nose-down pitching moments, with a maximum variation in ΔC_M (relative to $\Lambda = 0$) of -0.05 at $\alpha = 14°$. The characteristic feature of the changes in C_M for this bleed configuration is that the change is confined to a relatively

narrow range of Λ that decreases with increasing angle of attack. There is virtually no change in C_M at $\alpha = 8°$ (less than $\Delta C_{M,max} = 0.01$) but the quasi-steady bleed ($0 < \Lambda < 1$) produces $\Delta C_L = -0.20$. By $\alpha = 10°$ the sharp change in C_M occurs around $\Lambda = 0.5$, but C_M is nearly invariant for $\Lambda < 0.5$, and $\Delta C_L = -0.39$ from $0 < \Lambda < 1$. For $\alpha = 18°$, the sharp change in C_M occurs around $\Lambda = 0.25$, and thereafter C_M is nearly invariant but $\Delta C_L = -0.40$. By $\alpha = 20°$ and higher angles, quasi-steady bleed yields positive (nose-up) variations relative to $\Lambda = 0$ for all values of Λ with this bleed configuration. Operating in these ranges of bleed actuation, where C_M is nearly invariant, allows for the independent control of lift without adversely affecting the pitching moment. Figure 3.2c also shows that increases in Λ result in small to moderate increases in C_D (up to 0.09) relative to $\Lambda = 0$ up to $\alpha = 18°$ followed by very slight reductions ($\Delta C_D = -0.02$) for $\alpha = 20°$ and 22°.

The data in Figures 3.1 and 3.2 indicate that variations in aerodynamic loading with Λ, especially in C_L, can be realized relative to some "operating point" that can be set within the range of louver openings. Then, the local sectional lift of the airfoil can be either increased or decreased relative to this operating point by modifying the spanwise variation of the bleed, without external control surfaces. In addition to aerodynamic maneuvering (for example, roll by differential spanwise lift), this approach can be used for direct lift control during landing and for stabilization of light, flexible airframes that are used for high-altitude UAVs.

The interaction between the bleed flow and cross flow over the suction surface of the airfoil that leads to the variations in aerodynamic forces shown in Figures 3.1 and 3.2 is investigated using particle image velocimetry (PIV) as shown in Figure 3.3 ($\alpha = 18°$),

where the field of view measures 0.175*c* x 0.075*c* in the cross stream directions (shown schematically in the inset at the top RHS). For each bleed setting, Figure 3.3 comprises color raster plots of spanwise vorticity concentrations superposed with cross stream distributions of velocity vectors (Figures 3.3a-e), color raster plots of distributions of the turbulent kinetic energy [TKE = $(\overline{u'u'} + \overline{v'v'})/2$, Figures 3.3f-j], and distributions of ("residual") velocity vectors relative to the velocity field of $\Lambda = 0$ from each of the velocity fields that are associated with the bleed flow (Figures 3.3k-n). These data are obtained for $\Lambda = 0$, 0.25, 0.5, 0.75, and 1 for which the momentum coefficients of the bleed jet are estimated: $C_\mu \cdot 10^4 = \frac{A_{outlet} \cdot V_{bleed}^2}{s \cdot c \cdot U_\infty^2} \cdot 10^4 =$ 0.63, 1.24, 1.87, 4.43, and 5.47, respectively (V_{bleed} is estimated from a control volume analysis of the jet velocity in the PIV images shown in Figure 3.3).

In the absence of bleed ($\Lambda = 0$, Figure 3.3a), the flow is nominally attached to the airfoil in the vicinity of the open bleed orifices on the suction surface (marked on the image). It is evident that small perturbations associated with the presence of the orifices lead to thickening of the boundary layer that is also evident in the distributions of the TKE in Figure 3.3f (and therefore leads to some reduction in lift relative to the base, smooth airfoil, cf. Figure 3.1). As the bleed commences ($\Lambda = 0.25$, Figure 3.3b), the flow separates from the surface at $x/c = 0.10$. At this bleed level, the separation domain within the field of view (as assessed from the presence of the reversed flow) is relatively shallow and the corresponding raster plot of TKE (Figure 3.3g) shows a central streamwise band of higher TKE that is bounded by lower intensity bands along the surface of the airfoil and near the outer flow. When $\Lambda = 0.5$ (Figure 3.3c), the separating shear layer is lifted away from the surface with a distinct domain of lower-level spanwise vorticity

concentrations near the surface of the airfoil. The domain of reversed flow begins immediately downstream of the second bleed port (x/c = 0.07). It is remarkable that even though the momentum coefficient of the bleed is small ($C_\mu \sim O[10^{-4}]$), it is sufficient to displace the oncoming flow and result in stronger separation as is evidenced by the extended streamwise domain of intense clockwise vorticity within the core of the separating shear layer. The core of the shear layer is also evident in the raster plot of TKE (Figure 3.3h) which shows a larger band of low levels near the surface. The separation continues to intensify as the bleed increases (Λ = 0.75 and 1) in (Figures 3.3d-e, and it appears that while the core of the shear layer intensifies, its cross stream extent diminishes. This narrowing is also evident in the corresponding TKE images (Figures 3.3i-j).

The bleed flow is clearly visible in Figures 3.3b-e. The onset of the separating shear layer is upstream of the first bleed port (x/c = 0.03), and the bleed layers appear to merge with the shear layer farther downstream as Λ and, consequently, C_μ are increased. It is interesting to note that the vorticity layer of the bleed flow is predominantly clockwise ostensibly as a result of the induced flow at the low-speed side of the separating shear layer. Finally, Figures 3.3k-n show cross stream distributions of the "residual" velocity vectors relative to the flow field of Λ = 0 (i.e., in the absence of bleed but with the outlet ports on the suction surface exposed to the cross flow). These distributions clearly show the increase in cross stream extent and intensity of the separated domain above the surface of the airfoil. The cross stream edge where the magnitude of the residual velocity is approximately 20% of the free stream speed increases in elevation with Λ to 0.045c (Λ = 0.25), 0.061c (Λ = 0.5), 0.065c (Λ = 0.75), and 0.072c (Λ = 1). Recall that these

changes correspond to decrements in C_L (cf. Figure 3.1a) although the magnitude of the rate of change of C_L with Λ decreases as Λ is increased. Since the bleed flow is driven by the pressure difference across the bleed inlet and outlet ports, it is remarkable that even though stall decreases the magnitude of the pressure difference between the bleed ports, the bleed intensifies with fractional opening, suggesting that the interaction with the separating shear layer (cf. Figure 3.3e) is stronger owing to the lower speed of the outer flow in the vicinity of the bleed ports.

The PIV data in Figure 3.3 are used to determine the speed of the bleed flow (Figure 3.4a) by establishing a control volume around the bleed outlets and computing the flow rate through each control surface. In this calculation, cross stream control surfaces extend along x/c = 0.01 and x/c = 0.14 and streamwise control surfaces along y/c = 0 (i.e., within the airfoil surface) and y/c = 0.08 in the images of Fig. 3.3a-e; as there are no data points within the airfoil, the imbalance in flow rate $Q = \bar{V}A = \int \vec{V} \cdot \hat{n}\, dA$ (where $\bar{V}$ is the average velocity through control surface area A) through the three control surfaces in the flow is equal to the flow rate through the bleed outlets. These data show that within the present measurement range, the bleed speed $\bar{V}$ and its nominal momentum coefficient C_μ (Figure 3.4b) vary approximately like Λ and Λ^2, respectively. Despite an increase in the degree of separation over the outlets with Λ (cf. Figures 3.3a-e) and, as discussed below in connection with Figure 3.6, an increase in static pressure on the suction surface near the outlets, the bleed velocity grows with Λ due to a reduction in the streamwise momentum of the cross flow above the outlets. Furthermore, the low momentum coefficient of the quasi-steady bleed flow rate clearly underscores the global control authority and the effects of its interaction with the cross flow.

The chordwise location of separation is assessed from static pressure distributions over the base airfoil and in the presence of quasi-steady bleed ($0 < \Lambda < 1$) for $8° < \alpha < 22°$ (Figure 3.5a). At $\alpha = 8°$, separation is not evident along the chord at any bleed level. As α is increased from 10° to 22°, trailing edge separation of the base airfoil monotonically moves upstream until it finally reaches the leading edge. In the presence of bleed, trailing edge separation commences at lower angles of attack when $\alpha > 8°$, and, for a given angle of attack, the separation migrates upstream with increasing Λ. However, it is noteworthy that for a given α, the effect of bleed magnitude on the upstream migration of separation saturates beyond some level Λ_o, although the aerodynamic forces continue to vary with the bleed input (cf. Figure 3.1). For example, for $\alpha = 10°$, an increase in Λ from 0 to 0.5 advances separation upstream to $x/c = 0.68$ ($\Delta C_L = 0.10$ between $\Lambda = 0$ and 0.5 as shown in Figure 3.2). However, as the bleed increases beyond $\Lambda_0 = 0.75$, separation does not move beyond $x/c < 0.75$ although ΔC_L continues to increase up to 0.44 at $\Lambda = 1$. Figure 3.5b illustrates the characteristic effect of bleed at $\alpha = 14°$ (pre-stall) using vorticity concentrations and velocity vectors in the cross stream plane above the bleed outlets. At this α, the flow over the base airfoil begins to separate at $x/c = 0.57$. In the presence of bleed ports ($\Lambda = 0$), the pressure data show that the flow begins to separate at $x/c = 0.51$, and the data in Figure 3.5b show that as the bleed is increased the boundary layer in the vicinity of the bleed outlets becomes thicker with increasing Λ until the adverse pressure gradient is sufficient to lift the vorticity layer from the suction surface immediately at the bleed ports. Conversely, at pre-stall angles, separation can be displaced aft (e.g., from the leading edge to $x/c = 0.51$

at $\alpha = 14°$) simply by reducing Λ. Figure 3.5a also indicates that as long as the flow is not dominated by strong unsteady effects, *prescribed* separation may be maintained as the angle of attack varies (e.g., separation can be maintained near $x/c = 0.40$ between $\alpha = 12°$ and 16° by reducing quasi-steady bleed from $\Lambda = 0.5$ to 0). By $\alpha = 22°$, leading edge separation occurs for the base airfoil. However, as discussed in connection with Figure 3.3, even at post stall angles, the angle at which the separated shear layer is deflected into the cross flow (and therefore the aerodynamic shape and loads) can be altered by varying the bleed level. As discussed in §IV, the control authority of bleed actuation can be significantly extended by exploiting the receptivity of the cross flow to a combination of quasi-steady and time-periodic bleed actuation.

3.2 Time-Dependent Bleed Actuation

The bleed actuation discussed in §III is quasi-steady. In this section, the response of the flow over the airfoil to time-periodic bleed actuation is assessed by driving the louver actuators time-harmonically with a peak-to-peak amplitude of $\Lambda = 1$. The actuators are operated within their bandwidth at $0.67 < St_{act} = f_{act}c/U_\infty < 1.2$ (where $50 < f_{act} < 90$ Hz) and the resulting pulsating bleed leads to significant post-stall increases in lift.

The effects of time-periodic bleed actuation on distributions of static pressure about the airfoil at $\alpha = 14°$, 16°, 18°, 20°, and 22° are compared with the effects of $\Lambda = 0$ and quasi-steady bleed at $\Lambda = 1$ and with the base (smooth) airfoil (Figure 3.6). As noted in §II, the 32 pressure ports are distributed along the surface of the airfoil using the structural grid that supports the bleed ports. The flow over the base airfoil (gray) separates near $x/c = 0.50$ at $\alpha = 14°$, and as α increases to 16°, the separation migrates upstream to $x/c = 0.39$ without an appreciable change in the suction pressure upstream of

separation or on the pressure side of the airfoil. At $\alpha = 18°$, separation also occurs near $x/c = 0.39$ though the suction upstream of separation increases significantly to $C_P \approx -4.5$ ostensibly as a result of acceleration around the leading edge as the stagnation point migrates towards the pressure surface (although this motion of the stagnation point cannot be resolved by the present pressure measurements). This suction peak is unchanged at $\alpha = 20°$ while the separation moves to $x/c = 0.25$, but it vanishes when the airfoil becomes completely stalled at $\alpha = 22°$. It is evident that the presence of the bleed ports ($\Lambda = 0$) leads to an upstream migration of separation (to $x/c = 0.33$ and 0.27 at $\alpha = 14°$ and 16°, respectively) and therefore to some loss in lift (cf. Figure 3.1a) although the suction peak is comparable to the peak of the base airfoil. However, at $\alpha = 18°$ the presence of the bleed ports results in upstream migration of separation ($x/c = 0.22$ compared to 0.39 for the base airfoil) and a lower suction peak, and the airfoil becomes completely stalled at $\alpha = 20°$ and 22°. These data indicate that improved integration of the bleed ports may reduce their impact on the aerodynamic performance at high angles of attack. When $\Lambda = 1$, the bleed leads to complete stall already at $\alpha = 14°$, indicating that within the range $0 < \Lambda < 1$ the global lift can be significantly reduced (cf. Figure 3.1a) and result in a C_L decrement of up to 0.57 (or 39% compared to baseline) at $\alpha = 18°$ (note that the bleed leads to a small reduction in the magnitude of the static pressure near the inlet to the ports, $x/c \approx 0.6$).

Time-periodic bleed actuation alters the pressure distribution significantly. Although the suction peak is not fully restored for $\alpha = 16°$ and 18°, the flow becomes nearly fully-attached along the entire top surface of the airfoil with significant increases in suction and some increase in pressure on the pressure side. When the base airfoil begins to stall at

$\alpha = 18°$ and 20°, the suction effected by periodic bleed actuation exceeds the suction on the base airfoil for $x/c > 0.16$ and 0.07, respectively (at $\alpha = 18°$, the lift increment relative to the base flow is $\Delta C_L = +0.23$, discussed below in Figure 3.7). Finally, when the base airfoil is fully stalled at $\alpha = 22°$, the suction induced by the actuation still persists and the flow appears to be attached through the trailing edge. It appears that the magnitude and distribution of the suction pressure in the vicinity of the leading edge is modified by the change in the apparent shape of the airfoil in the presence of bleed (as discussed in connection with Figure 3.9 below).

The effect of time-periodic bleed actuation on the lift over the airfoil for $0° < \alpha < 22°$ is illustrated in Figures 3.7a-c for three bleed configurations in which the number of bleed ports on the suction side is 1, 2, and 3 ($0.06 < x/c < 0.07$, $0.03 < x/c < 0.07$, and $0.01 < x/c < 0.07$, respectively). The range of lift variations with bleed is color highlighted such that quasi-steady bleed is marked in blue and time-periodic bleed is marked in orange. To begin with, the data in Figures 3.7a-c show that the effectiveness of the bleed can be divided into two regimes: time-stationary actuation as represented by quasi-steady bleed on relatively long time scales compared to the characteristic convective time scale of the flow (i.e., $T_{act} > T_{conv}$), and time-varying actuation for which the characteristic actuation time is commensurate with the characteristic convective time scale of the flow (i.e., $T_{act} \approx T_{conv}$). While the former is primarily effective below stall ($\alpha < 18°$) the latter is primarily effective at and above stall. The data in Figures 3.7a-c also show that range of affected lift increases with the streamwise extent of the bleed (or number of bleed ports) with more significant differences between one and two bleed ports (Figures 3.7a and b). When time-periodic bleed actuation is applied, the range of

the attainable lift is extended well beyond the levels of the base airfoil as marked in orange (with a small loss between 11° and 16°). It is interesting to note that the peak C_L (1.7 at $\alpha = 18°$) can be attained by a single actuation port (Figures 3.7a), but larger actuation area is more effective at higher angles of attack. Similarly, the effects of the streamwise position of the bleed port on the effectiveness range of the actuation are measured for a single spanwise row 0.0125*c* in streamwise width that is centered about *x/c* = 0.014, 0.035, and 0.062 as shown in Figures 3.8a-c, respectively. Even though each of the three rows is located upstream of separation when $\Lambda = 0$, the upstream port appears to provide the widest range of time-periodic bleed control while the domain of effectiveness of quasi-steady bleed increases with streamwise location indicating that the magnitude of the pressure difference across the bleed path and perhaps the adverse pressure gradient on the suction surface affect this effectiveness.

The data in Figures 3.7 and 3.8 demonstrate that *bleed actuation can yield continuous adjustment of the lift within a broad domain of angles of attack* ($8° < \alpha < 22°$). For example, for $\alpha = 18°$, $0.9 < C_L < 1.7$ ($-0.57 < \Delta C_L < +0.23$ relative to the baseline) without the use of external control surfaces. These variations in C_L can be used for maneuvering (e.g., roll control), direct adjustment of spanwise lift distributions, or structural stabilization.

The flow fields over the entire airfoil at $\alpha = 18°$ for $\Lambda = 0$ and in the presence of quasi-steady bleed at $\Lambda = 1$ and time-periodic bleed actuation at $St_{act} = 1.2$ using two spanwise rows of bleed ports are shown in Figures 3.9a-c, respectively, using composite color raster plots of time-averaged spanwise vorticity concentrations measured using PIV. The aerodynamic loads for this bleed configuration are shown in Figures 3.1a-c

($\alpha = 18°$ is marked using a dashed line), for which the upper and lower bounds of the blue domain correspond to $\Lambda = 0$ and $\Lambda = 1$, respectively. As shown in Figure 3.9a, when $\Lambda = 0$ ($C_L = 1.30$ in Figure 3.1a), the flow separates near $x/c = 0.25$, and the separated shear layer appears to be aligned with free stream. However, when the louvers are completely open ($\Lambda = 1$, $C_L = 0.90$ in Figure 3.1a), the interaction of the bleed flow with the separating shear layer leads to significant vectoring of its nominal centerline away from the airfoil at an angle of approximately 13° relative to the free stream, even though the bleed momentum coefficient is relatively low (estimated as $C_\mu = 5.47 \cdot 10^{-4}$; cf. Figure 3.4). Of course, ultimately, the shear layer becomes aligned with the free stream downstream of the trailing edge of the airfoil. As noted in connection with Figure 3.3e, the cross stream width of the vectored shear layer appears to decrease and the vorticity concentrations at the low-speed side are considerably weaker than for the shear layer that forms when $\Lambda = 0$ (Figure 3.9a). When the bleed actuation is time-periodic (Figure 3.9c, $C_L = 1.70$ in Figure 3.10a), the separating shear layer is deflected downward along the surface of the airfoil, resulting in a thick vorticity layer above the surface with virtually no evidence of recirculating flow. It appears that as a result of the actuation some of the shear layer vorticity is advected within the high-speed side of the shear layer (e.g., $x/c > 0.30$) ostensibly as a result of time-periodic formation of discrete vorticity concentrations that are phase-locked to the actuation. The interaction of the time-periodic bleed actuation with the outer flow leads to the formation of a domain of trapped vorticity downstream of the leading edge that is captured in the time-averaged field and enables the outer flow to overcome the adverse pressure gradient (and with it separation) and lead to increased lift. As shown in Figure 3.6, the flow attachment leads to stronger

suction along the top surface of the airfoil, particularly aft of $x/c = 0.25$, resulting in a nose-down pitching moment relative to the baseline and to quasi-steady bleed (Figure 3.10b). In fact, Figure 3.10b shows that for $8° < \alpha < 22°$, both quasi-steady and time-periodic bleed actuation are capable of generating a nose-down pitching moment relative to the baseline. The flow fields in Figures 3.9a-c exhibit similar levels of drag (Figure 3.10c), though it appears that form drag dominates when $\Lambda = 0$ and 1 and lift-induced drag is responsible for the level of C_D during time-periodic actuation resulting in $\Delta C_D = 0.05$ relative to the baseline airfoil. Figures 3.10a-c show that for this bleed configuration, time-periodic actuation primarily extends the lift effectiveness beyond that of the baseline and of quasi-steady bleed (cf. Figure 3.1) without adversely affecting C_M or C_D.

The evolution of the separating shear layer is assessed from cross stream distributions of the (normalized) streamwise velocity at $x/c = 0.25$, 0.5, 0.75, and 1 (Figures 3.11a-d, respectively, where $\tilde{y}$ denotes the cross stream distance from the airfoil surface at each chordwise location). At $x/c = 0.25$, the flow for $\Lambda = 0$ is still attached, but becomes separated at $x/c = 0.5$ with reversed flow within $0 < \tilde{y}/c < 0.06$ that extends to $\tilde{y}/c = 0.14$ and 0.19 by $x/c = 0.75$ and 1, respectively. However, in the presence of quasi-steady bleed at $\Lambda = 1$, the flow is already separated by $x/c = 0.25$ and the separated domain spreads rapidly in the cross stream direction as is evidenced from the cross stream distributions at $x/c = 0.5$, 0.75, and 1 with reversed flow to $\tilde{y}/c < 0.13$, 0.22, and 0.28, respectively with a significant decrease in lift relative to $\Lambda = 0$ ($\Delta C_L = -0.40$). In the presence of time-periodic bleed, the flow exhibits a fundamentally different structure. The cross stream velocity profiles indicate the presence of a narrow, cross-stream domain

of recirculating flow near the surface which is only evident at $x/c = 0.5$ ($\tilde{y}/c < 0.02$), vanishes by $x/c = 0.75$ (in the presence of the time-periodic actuation the flow is attached through the trailing edge), and is associated with the apparent change in the (time-averaged) shape of the surface by the trapped vorticity allowing flow to overcome the inherent adverse pressure gradient and resulting in increased lift.

Although the time-averaged vorticity fields in Figures 3.9a-c include no temporal information about vorticity production and advection near the surface due to bleed, these dynamics can be surmised from distributions of the TKE (Figure 3.12). As shown in Figure 3.12a, in the absence of bleed (but with open ports on the suction surface, $\Lambda = 0$) the data shows evidence of velocity fluctuations within the boundary layer upstream of separation that are ostensibly intensified by the open (but inactive) bleed ports. The fluctuations are relatively weak within the recirculating flow domain $0.40 < x/c < 1$, though the separated shear layer is clearly marked by concentrations of TKE that begin to fill the cross stream extent of the near wake downstream of the trailing edge of the airfoil. Perhaps the most prominent feature in the presence of quasi-steady bleed at $\Lambda = 1$ (Figure 3.12b) is the band of intense fluctuations that propagate away from the leading edge and bound a domain of relatively low levels of fluctuations near the suction surface that extends over the majority of the chord. The advection of vorticity concentrations within the deflected separating shear layer (Figure 3.9b) is clearly marked by elevated levels of TKE within the layer.

In the presence of time-periodic actuation (Figure 3.12c), a relatively thin, intense band of TKE develops over the leading edge of the suction surface and especially near the bleed outlets. Further along the chord ($x/c > 0.25$), this band begins to align with the

direction of the free stream but becomes most concentrated within a thick cross stream domain (e.g., $\Delta y/c \approx 0.10$ at $x/c = 0.50$) that is deflected towards the airfoil surface. Unlike the separated flows in Figures 3.12a and b, the TKE fills the entire cross stream extent of the near wake. The concentrated levels of TKE in the layer above the suction surface in Figure 3.12c indicate that although the increase in lift relative to the base flow and $\Lambda = 0$ might be interpreted as "reattachment" of the stalled flow, this increase is not the result of a formally pre-stall boundary layer. It appears that the actuation increases the entrainment by the separated shear layer and therefore leads to a Coandă-like deflection towards the surface of the airfoil such that the layer vortices (cf. Figure 3.9c) are advected along the surface through the trailing edge. This observation is supported by instantaneous PIV images (not shown) that confirm that the interaction of the time-periodic bleed with the surface layer leads to the nearly frequency-locked, time-dependent advection of discrete, large-scale vortical structures within the deflected shear layer. In §4, the evolution of these structures, the time scales governing their interaction with the cross flow, and their impact on aerodynamic loading are explored in more detail on a static VR-7 airfoil model.

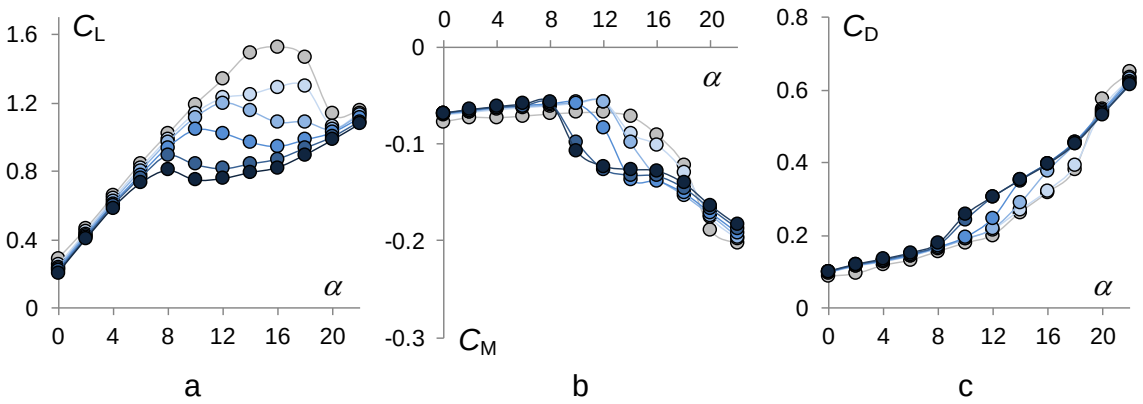

Figure 3.1. Variation of C_L (a), C_M (b), and C_D (c) with angle of attack for the base airfoil (●) and for several quasi-steady louver openings: $\Lambda = 0$ (●), 0.25 (●), 0.5 (●), 0.75 (●), and 1 (●).

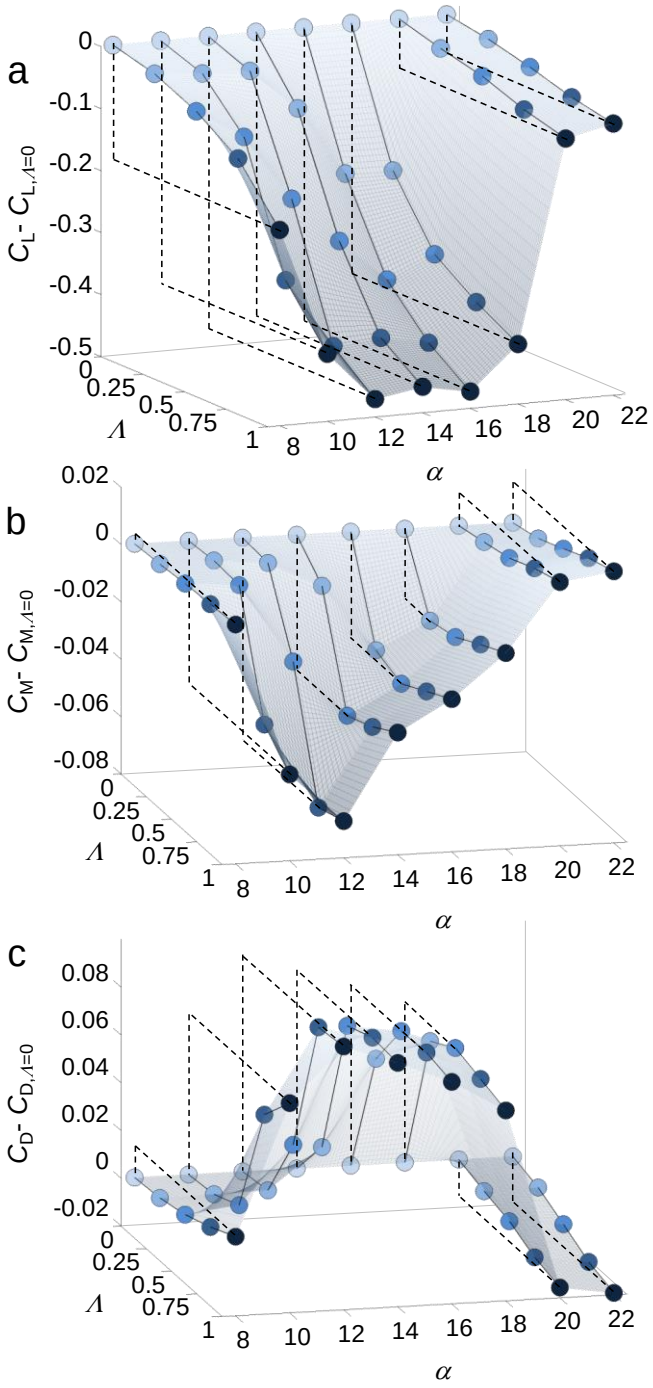

Figure 3.2. Variation of C_L (a), C_M (b), and C_D (c) with quasi-steady louver opening Λ relative to $\Lambda = 0$ for $8° < \alpha < 22°$. Black dashed lines indicate the magnitude of the extremum at each angle, and symbol colors correspond to the levels of Λ as shown in Figure 3.1.

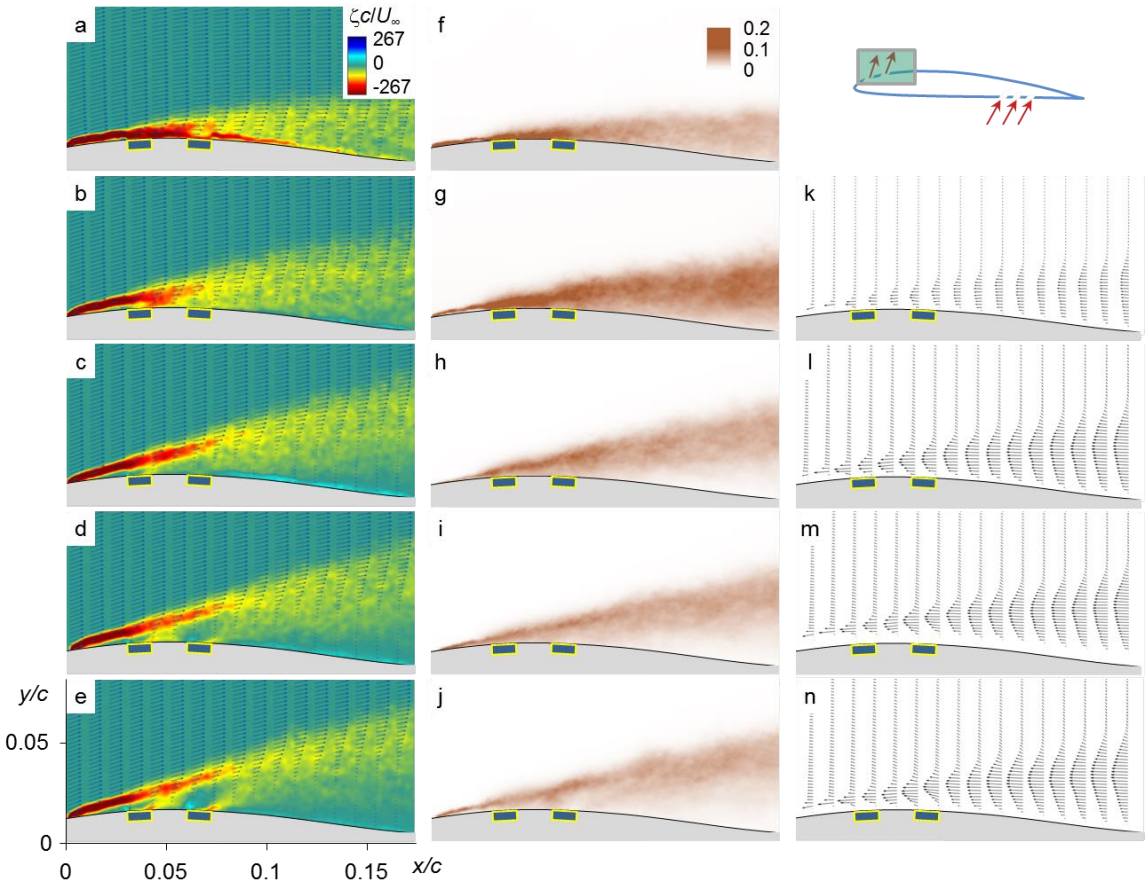

Figure 3.3. The interaction between the bleed and the cross flow over the suction surface at α = 18° measured using PIV within the field of view shown schematically in the inset at the top right. The images in each column from top to bottom correspond to: Λ = 0, 0.25, 0.50, 0.75, and 1. Columns: (a-e) color raster plots of spanwise vorticity concentrations and cross stream distributions of velocity vectors; (f-j) color raster plots of distributions of TKE; and (k-n) cross stream distributions of residual velocity vectors.

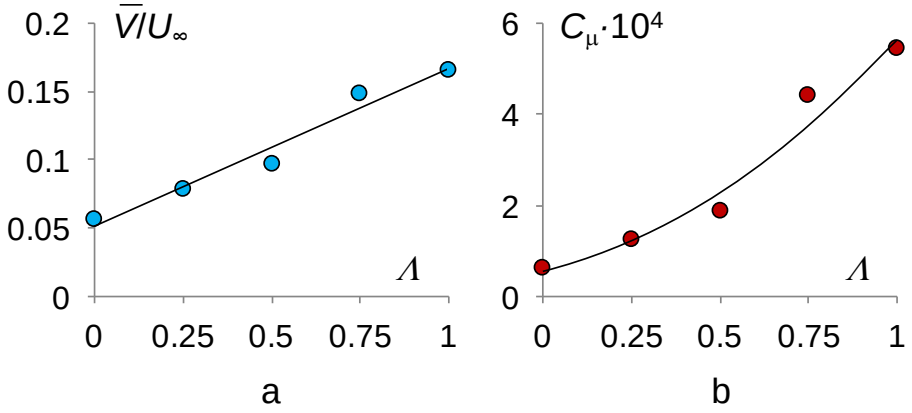

Figure 3.4. Variation of the average bleed speed (a) and momentum coefficient $C_\mu \cdot 10^4$ (b) at the bleed outlet with fractional louver opening Λ at $\alpha = 18°$.

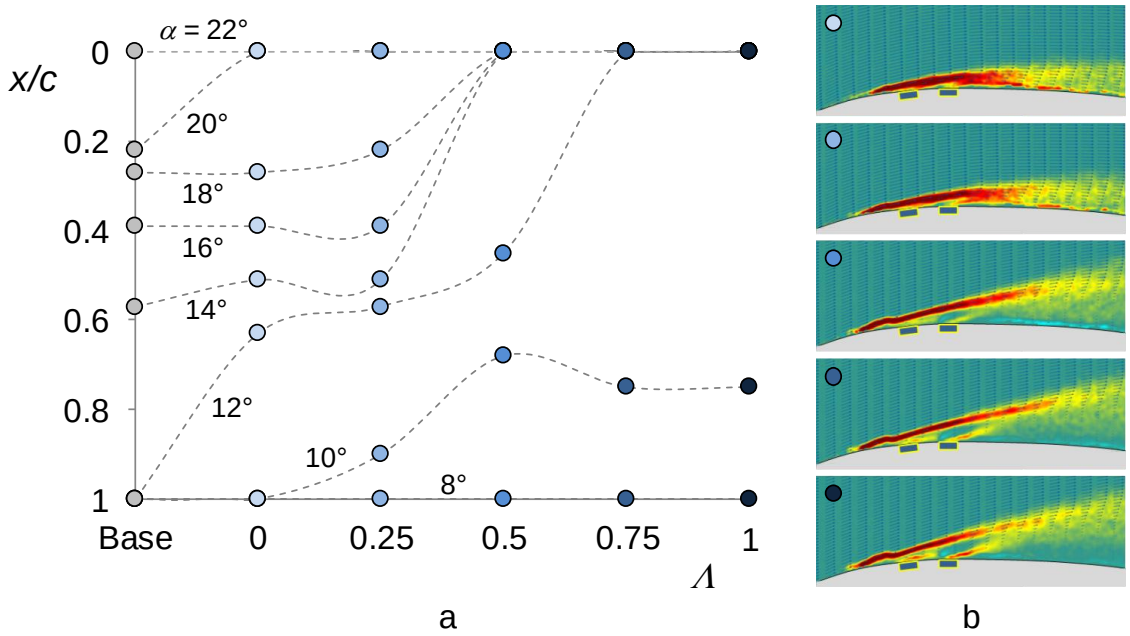

Figure 3.5. Variation in chordwise location of separation assessed from static pressure measurements for $8° < \alpha < 22°$ for the base airfoil and with quasi-steady bleed actuation (a), and distributions of spanwise vorticity and velocity vectors above the bleed outlets at $\alpha = 14°$ for $0 < \Lambda < 1$ (b). Symbol colors correspond to the levels of Λ as shown in Figure 3.1.

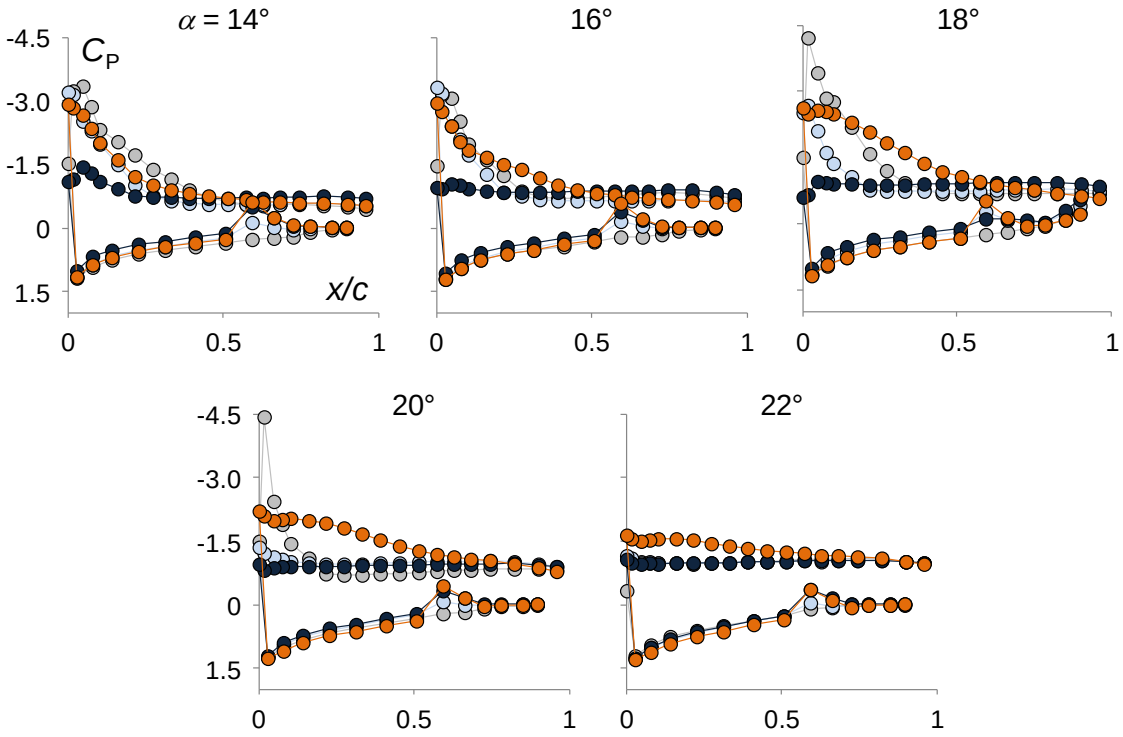

Figure 3.6. Pressure distributions over the airfoil at $\alpha = 14°$, 16°, 18°, 20°, and 22°: base (smooth) airfoil (●), and for $\Lambda = 0$ (●), $\Lambda = 1$ (●), and time-periodic actuation (●) using two bleed ports ($0.03 < x/c < 0.07$). The opening of the louvers is accompanied by a local reduction in pressure near $x/c = 0.6$.

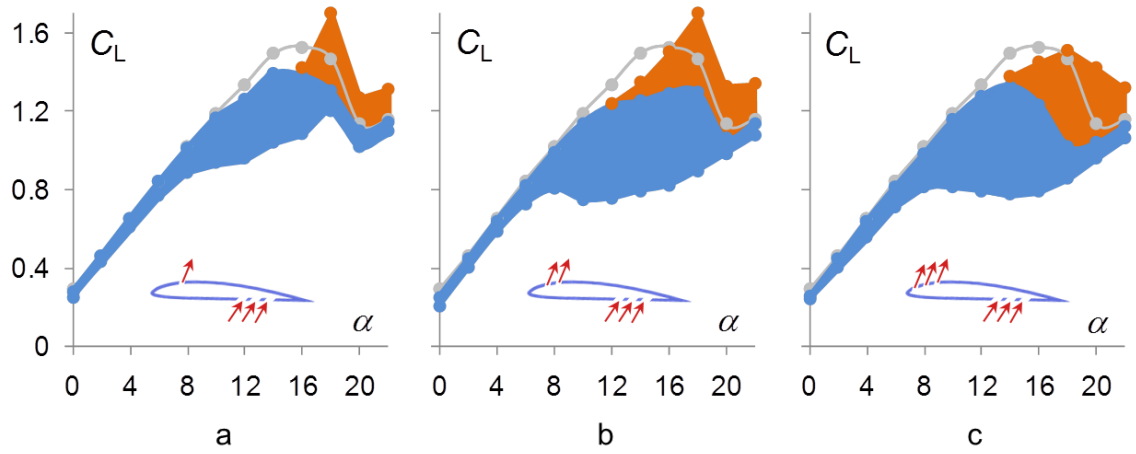

Figure 3.7. Effective ranges of bleed actuation as measured by variations of lift with α (quasi-steady and time-periodic bleed are marked in blue and orange, respectively) for three bleed configurations in which the number of bleed ports varies on the suction surface is: a) one, $0.06 < x/c < 0.07$, b) two, $0.03 < x/c < 0.07$, and c) three, $0.01 < x/c < 0.07$. The ranges of lift variations with quasi-steady and time-periodic bleed are marked in blue and orange, respectively.

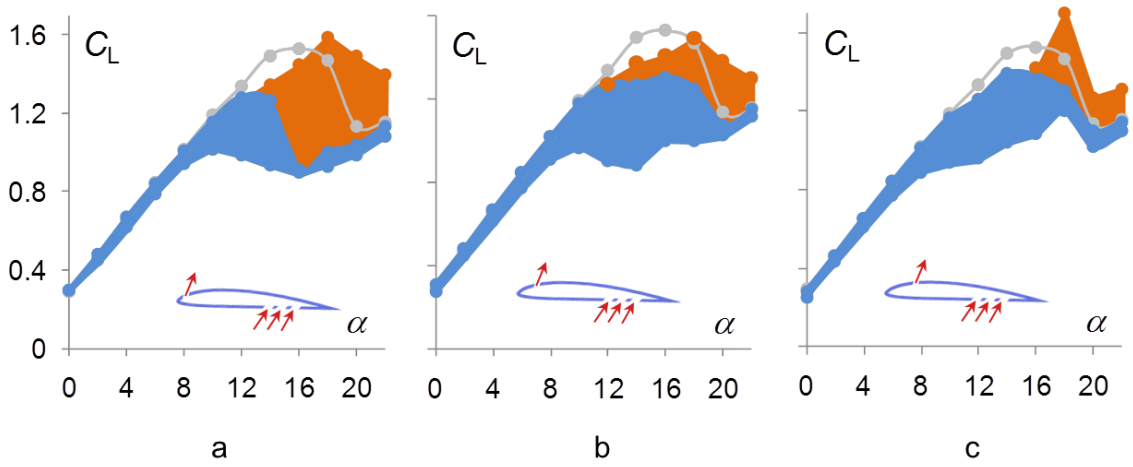

Figure 3.8. As in Figure 3.7 for three streamwise positions of a single bleed outlet port on the suction surface at x/c = 0.014 (a), 0.035 (b), and 0.062 (c).

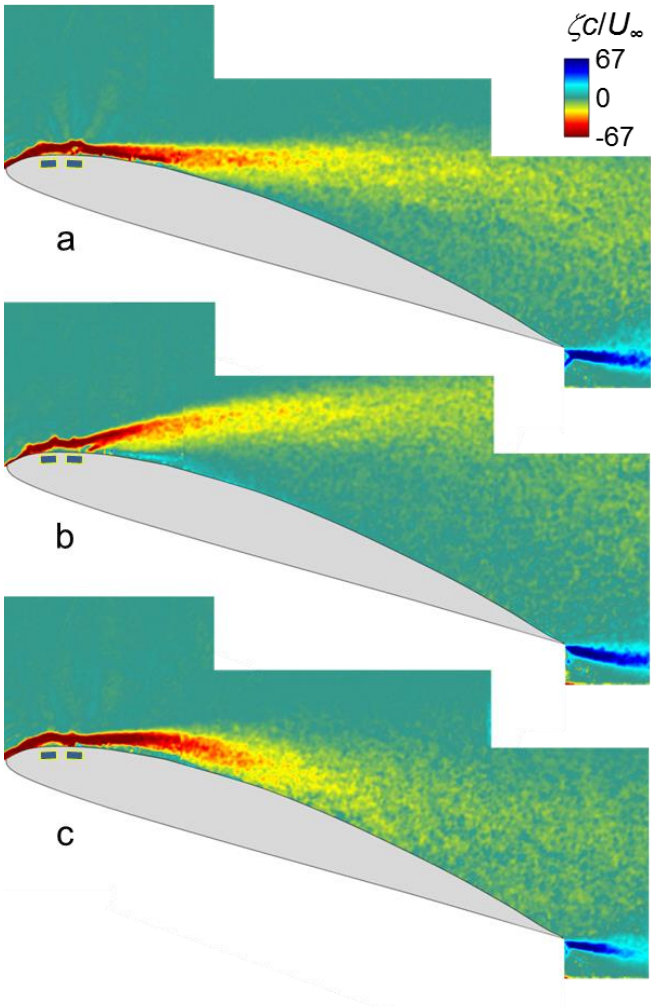

Figure 3.9. Color raster plots of spanwise vorticity concentrations over the airfoil at $\alpha = 18°$ for $\Lambda = 0$ (a), 1 (b) and time-periodic bleed actuation at $St_{act} = 1.2$ (c). Corresponding levels of C_L, C_M, and C_D are shown in Figure 3.10a-c, respectively.

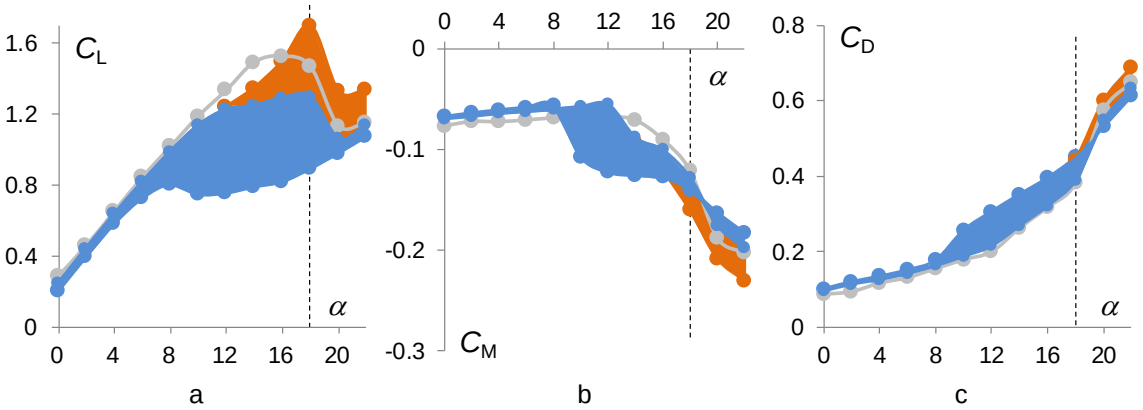

Figure 3.10. Effective ranges of bleed actuation (as in Figure 3.7) measured by variations of C_L (a), C_M (b), and C_D (c) with α. The bleed configuration is as in Figure 3.9 (outlets from $0.03 < x/c < 0.07$), and $\alpha = 18°$ is marked with a dashed line.

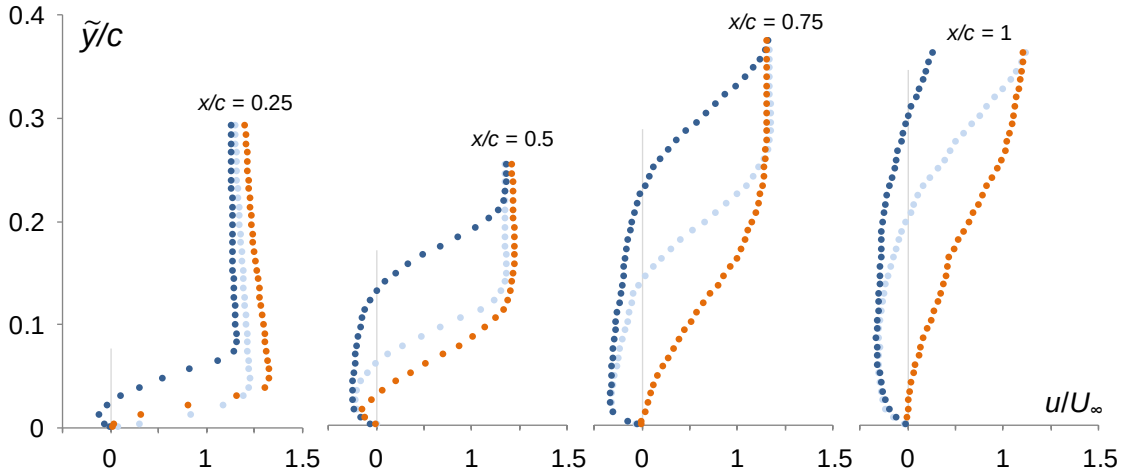

Figure 3.11. Cross stream distributions of the streamwise velocity (corresponding to the flow fields of Figure 3.9) measured relative to the airfoil's suction surface (denoted by $\tilde{y} = 0$) at the chordwise stations $x/c = 0.25$, 0.5, 0.75, and 1: $\Lambda = 0$ (●), 1 (●), and time-periodic bleed actuation at $St_{act} = 1.2$ (●).

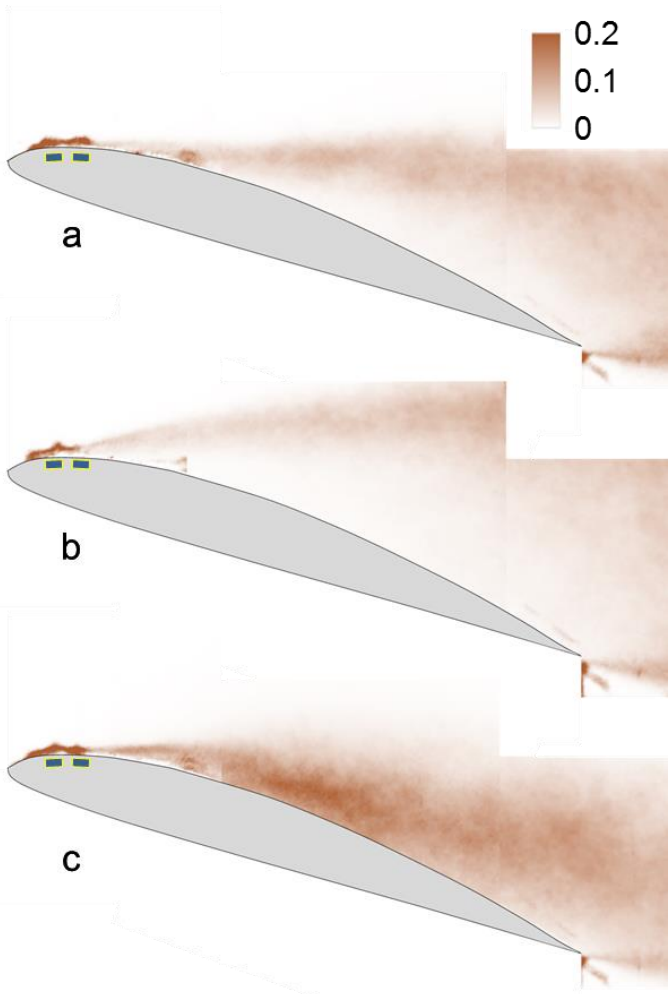

Figure 3.12. Color raster plots of distributions of TKE at $\alpha = 18°$: a) $\Lambda = 0$, b) $\Lambda = 1$, and c) time-periodic bleed.

CHAPTER IV

MODIFICATION OF VORTICITY CONCENTRATIONS ON A STATIC AIRFOIL USING BLEED ACTUATION

Building on the preliminary findings of §3, the time-resolved interactions between the bleed and cross flows are investigated to elucidate the mechanisms by which bleed alters the aerodynamic loading on a static airfoil model (VR-7, cf. §2.2.2). The chapter begins by assessing the alteration of the aerodynamic loads using a number of quasi-steady and time-periodic bleed configurations over a wide range of angles of attack. Time-averaged distributions of velocity and spanwise vorticity concentrations in the cross stream plane show that bleed leads to bifurcation and deflection of the vorticity layer over the airfoil. This is also investigated using proper orthogonal decomposition (POD). The time scales of the interaction with the cross flow are investigated using step actuation and are extended to time-periodic actuation that triggers the periodic formation and advection of large-scale vortices.

4.1 Modification of Aerodynamic Loads by Bleed Actuation

The effects of bleed actuation on the global aerodynamic loads are investigated using quasi-steady and time-periodic louver-controlled bleed through several configurations of bleed ports over a broad range of angles of attack ($0° < \alpha < 22°$). Figures 4.1a-c show a composite of the aerodynamic loads (C_L, C_M, and C_D, respectively) that can be realized over the entire range of the present actuation parameters (including, for reference, the base flow and the thin airfoil theory lift offset by 0.25 to account for airfoil camber). The

actuation includes closed louvers with open outlets ($\Lambda = 0$), quasi-steady bleed at $\Lambda = 1$, and time-periodic bleed (with non-zero mean), using multiple rows of bleed ports. These data demonstrate that bleed actuation can yield nearly-continuous variations of the aerodynamic forces and moments within a range which (at least for C_L) is bounded from below by bleed when all ports are fully open on both the suction and pressure surfaces and from above by the performance of the base airfoil for $\alpha < 13°$ and by the response of the flow to time-periodic bleed actuation for $13° < \alpha < 22°$ which appears to overcome the effects of stall in the base flow.

The response of the flow over the airfoil to bleed actuation can be roughly divided into two domains of angles of attack, namely, below and above the range within which the flow over the base airfoil begins to separate just upstream of the trailing edge. Below stall, quasi-steady bleed actuation leads to a significant reduction in lift (decrements of up to 88% can be realized, e.g. at $\alpha = 0°$) that, depending on the bleed configuration, are accompanied by substantial increases (e.g., up to 125% at $\alpha = 4°$) or decreases (up to 27% at $\alpha = 8°$) in drag relative to the base airfoil. At post stall angles of attack time-periodic bleed actuation results in a range of significantly higher lift than on the base airfoil (lift increment of up to 61% relative to the base flow is realized at $\alpha = 19°$), and, depending on the bleed configuration, the drag can be substantially reduced (by up to 35% at $\alpha = 19°$). As demonstrated in §3.1, the changes in C_L and C_D are associated with control of the separation domain over the suction surface of the airfoil. Although time-periodic bleed actuation is very effective in increasing lift at post stall angles of attack, it should be noted that some configurations of quasi-steady bleed can also lead to significant increases in lift (up to 32% at $\alpha = 19°$).

Bleed actuation also has some profound effects on the distributions of the pitching moment below and above stall. For $\alpha < 16°$, there are some nose-up variations for a few bleed configurations (C_M is bounded from above by a configuration which allows bleed through $x/c > 0.72c$, for which $\Delta C_{M,max} = +C_{M,0}$ (at $\alpha = 11°$), and significant nose-down moment for most bleed configurations (e.g., $\Delta C_M = -2.65C_{M,0}$ at $\alpha = 16°$). While the post-stall C_M of the base airfoil undergoes a sharp nose-down increase, bleed actuation induces a nose-up moment so that C_M can be nearly invariant over a broad range of α. Though post-stall, while the pitching moment relative to the base airfoil is mostly nose-up, some actuation configurations can yield a nose-down moment (e.g., at $\alpha = 18°$, $-0.17 < C_M < -0.05$). The joint distribution of C_L and C_M (Figure 4.2) exhibits left and right clusters of data in upper and lower bands that roughly correspond to time-periodic and quasi-steady actuation, respectively. In the right cluster, which includes the baseline and all bleed configurations when the flow is attached at low to moderate angles of attack, the distribution is nearly bounded by $C_M \approx -0.03$ (with the exception of the configuration allowing bleed through $x/c > 0.72c$) while C_L varies over a range of about 1.2 indicating an opportunity for changing the sectional lift independently of the pitching moment. The left cluster includes the post-stall baseline but also several time-periodic and quasi-steady bleed configurations which are not stalled for which $C_L \gtrsim 1.3$. It is remarkable that time periodic actuation enables significant variation of C_M for nearly invariant, post-stall-enhanced $C_L \approx 1.5$.

In what follows, we restrict attention to several specific bleed configurations. The aerodynamic effects of distributed bleed at low angles of attack are explored using four representative bleed configurations that are shown schematically in Figure 4.3: in

configuration *C1*, bleed is effected through nine spanwise rows of ports on the suction surface within the extent $0.29 < x/c < 0.47$ for which the ratio of the total bleed area to the airfoil's planform area is $A_b/A_p = 0.08$ (there are no bleed ports on the pressure side); configuration *C2* utilizes the ports of *C1* and adds three spanwise rows of bleed ports on the pressure surface within the extent $0.37 < x/c < 0.43$ ($A_b/A_p = 0.10$); configuration *C3* adds three additional rows of ports to *C2* on the pressure side upstream of the rows of *C2* so that the open ports are within $0.31 < x/c < 0.43$ ($A_b/A_p = 0.13$); finally, in configuration *C4*, all available bleed ports on the airfoil are open, corresponding to $A_b/A_p = 0.50$.

Figures 4.3a-c show variations with α of C_L, C_M, and C_D, respectively, for the base airfoil ($C_L = 2\pi\alpha$ is shown for reference with an offset of 0.25), and for *C1*, *2*, *3*, and *4*. These data show that the lift distribution is bounded from above by lift of the base airfoil (which agrees well with lift of a thin airfoil up to $\alpha < 8°$). The lift is bounded from below by the performance of the fully-open airfoil (*C4*), which exhibits a maximum lift reduction of $\Delta C_L = C_L - C_{L,0} = 0.97$ relative to the base flow at $\alpha = 10°$. The data in Figure 4.3 indicate that increasing bleed diminishes $dC_L/d\alpha$ (from 0.10/° to 0.03/°, for the base airfoil and *C4*, respectively). While the presence of bleed ports on the suction surface with closed louvers (*C1*) results in a slight decrease in lift (e.g., $\Delta C_L = 0.08$ at $\alpha = 10°$), there is a considerable reduction in lift with configurations *C2* and *C3* ($\Delta C_L = 0.46$ and 0.58, respectively at $\alpha = 10°$) indicating that the diminution in lift results primarily from the bleed flow rather than the presence of the ports. Though the base and fully-open configurations form the upper and lower bounds of C_L and C_D, Figure 4.3b shows that they result in nearly identical C_M through $\alpha = 6°$ and that C_M of *C1* is similar to the base through $\alpha = 10°$, indicating that the presence of the bleed ports just

downstream of mid chord has little impact on C_M. However, quasi-steady bleed results in nose-down C_M well outside of this range, where the lower bound is formed by *C3* with a maximum $\Delta C_M = -0.44C_{M,0}$ at $\alpha = 5°$. These quasi-steady bleed configurations are accompanied by variations in drag that range from an increase of up to $\Delta C_D = 1.25C_{D,0}$ ($\alpha = 4°$) for the fully open airfoil, which may be thought of as a bluff body, to a decrease of up to $\Delta C_D = -0.27C_{D,0}$ ($\alpha = 8°$) with maximum variations in $\Delta(L/D)$ of -12.79 and 5.62 relative to the base airfoil.

Some of the effects of both quasi-steady and time-periodic bleed actuation at intermediate and high ranges of angles of attack are explored using bleed through a single spanwise row of ports on the suction surface ($0.03 < x/c < 0.04$) where the bleed inlet on the pressure side ($0.51 < x/c < 0.72$) is regulated by the louvers. Figures 4.4a-c show the variations of C_L, C_M, and C_D, respectively, with angle of attack for the base (sealed) airfoil, quasi-steady bleed at $\Lambda = 1$, and in the presence of time-periodic bleed by operating the louvers at $St_{act} = f_{act}c/U_\infty = 1.1$ between $\Lambda = 0$ and 1. These data show that while time-periodic bleed has little effect below $\alpha < 8°$, quasi-steady bleed leads to a significant diminution in C_L for $8° < \alpha < 22°$, with a maximum decrease $\Delta C_L = -0.33C_{L,0}$ (relative to the base airfoil) at $\alpha = 15°$. Perhaps the most striking feature in Figure 4.4a is that time-periodic bleed actuation leads to a significant increase in lift near the stall angle ($\Delta C_L = 0.15C_{L,0}$ at $\alpha = 16°$), and maintains higher levels of lift than in the base flow for $\alpha > 16°$ (the maximum lift increment among the configurations shown in Figure 4.1a is $\Delta C_{L,max} = 0.61C_{L,0}$ at $\alpha = 19°$ when bleed is effected between $0 < x/c < 0.01$). Although this effect of the actuation may be thought of as "attachment," the discussion in §4.2 shows that the separated vorticity layer is merely deflected towards the airfoil's

surface. Furthermore, quasi-steady actuation can also lead to significant increases in lift for $14° < \alpha < 22°$, indicating that the actuation can be self-regulating in response to the dynamics of the flow over the suction surface. As shown in Figures 4.1a and 4.2, time-periodic bleed actuation may be operated with different levels of offset and oscillation amplitudes over the entire range of fractional louver opening, thereby enabling continuous variations of C_L between the peak attained with maximum time-periodic amplitude and the minimum levels corresponding to quasi-steady actuation.

This time-periodic and quasi-steady bleed actuation also has significant effects on the pitching moment. The actuation induces slight nose-up moment about $c/4$ relative to the base airfoil at low to moderate angles of attack ($0° < \alpha < 11°$), and as flow begins to separate near the trailing edge ($\alpha \approx 10°$), the bleed results in a nose-down moment of increasing magnitude. Near the static stall angle ($\alpha \approx 17°$), time-periodic and quasi-steady bleed lead to $\Delta C_M = -1.08 C_{M,0}$ and $-2.15 C_{M,0}$, respectively. At the same time, the drag due to bleed exceeds the level of the base flow for pre-stall α and reaches the levels of the (stalled) base airfoil for $\alpha > 14°$, though the rate of increase of the drag with α owing to time-periodic bleed is higher than with quasi-steady bleed through stall as a result of the lift-induced drag.

The receptivity of the flow over the airfoil to time-periodic bleed actuation (using the bleed configuration of Figure 4.4) within the range $0.13 < St_{act} < 1.6$ (10 through 120 Hz) is investigated by measuring the aerodynamic loads as the flow over the static base airfoil progresses from pre- to post-stall at $\alpha = 14$, 16, and 18° (Figure 4.5, the corresponding levels of the base airfoil are marked for reference using solid lines). As shown in Figure 4.5a, at $\alpha = 14°$ the actuation leads to a reduction in C_L relative to the base airfoil that

diminishes slowly with increasing actuation frequency while the corresponding changes in C_M and C_D are minimal. At $\alpha = 16°$, the lift increases monotonically (almost linearly) for $0.1 < St_{act} < 0.5$ and then becomes nearly invariant for $St_{act} > 0.5$. For $0.1 < St_{act} < 0.4$, C_L is below the level of the base airfoil, but increases above it (up to 10% higher) thereafter. The corresponding C_M has a small nose-down increase as St_{act} increases, a local minimum near $St_{act} = 0.28$, and then the nose-up moment begins to increase nearly linearly for increasing St_{act} while the drag has a local maximum at $St_{act} = 0.28$ and then diminishes linearly with St_{act}. The variation of the aerodynamic loads with St_{act} at $\alpha = 18°$ is similar to 16°, except that the asymptotic level of C_L for $St_{act} > 0.5$ relative to the base airfoil is much higher (up to 47%), and the extrema of C_M and C_D occur at higher actuation frequencies ($St_{act} = 0.47$ and 0.60, respectively). Their rates of change with St_{act} for $St_{act} > 0.60$ are very similar, and C_D ultimately drops below the drag of the base airfoil for $St_{act} > 1.33$.

The variations of the aerodynamic loads on the base airfoil with bleed actuation indicate that the aerodynamic forces can be varied relative to an "operating point" that is set within the range of louver actuation. Spanwise variation of the bleed can be used for increasing or decreasing the local sectional lift or pitching moment relative to this operating point *without external control surfaces*. In addition to aerodynamic maneuvering (for example, roll by differential spanwise lift), this approach can be used for direct lift control (DLC) during landing and for the stabilization of light, flexible airframes that are used for high-altitude UAVs.

4.2 Modification of the Surface Vorticity Layer by Quasi-Steady Bleed Actuation

The global effects of quasi-steady and time-periodic bleed actuation on the flow over the airfoil and in its near-wake are assessed from PIV measurements at pre- and post-stall angles of attack. As discussed in connection with Figure 4.1a, below stall, the bleed leads to significant regulation of lift diminution that is accompanied by either nose-up or nose-down increases in pitching moment. The effect of bleed actuation on the global flow over the airfoil is demonstrated at $\alpha = 16°$ (pre-stall) using one row of spanwise ports on the suction surface ($0.03 < x/c < 0.04$) where the inlet bleed flow through the pressure surface ($0.51 < x/c < 0.72$) is regulated by the louver actuators. Figures 4.6a-c show time-averaged color raster plots of spanwise vorticity concentrations and cross stream distributions of velocity vectors for the base airfoil and in the presence of quasi-steady ($\Lambda = 1$) and time-periodic ($St_{act} = 1.1$) bleed, respectively. The time-averaged base flow separates at $x/c \approx 0.45$ and forms a shear layer above a recirculating flow domain that extends through the trailing edge as is evidenced by the opposite sense (counterclockwise, CCW) vorticity layer near the surface. As shown in Figure 4.4a, the base lift saturates and begins to taper off for $\alpha > 11°$ ($C_{L,max} = 1.35$, and $C_L = 1.30$ at $\alpha = 16°$) as the (time-averaged) separation migrates upstream from the trailing edge before the airfoil becomes completely stalled at the leading edge for $\alpha > 17°$ (which is also accompanied by sharp increases in nose-down C_M and in C_D). As shown in Figure 4.6b, the interaction of the quasi-steady bleed with the flow over the surface causes the separation to migrate further upstream to at $x/c \approx 0.2$. The separating shear layer is vectored away from the airfoil at an angle of approximately 10° relative to the direction of the free stream while the CCW vorticity layer over the surface intensifies, indicating a

stronger recirculation that extends $\Delta y/c$ = 0.25 above the trailing edge (compared to $\Delta y/c$ = 0.15 for the base airfoil) while the lift is reduced to 0.90 (C_D increases from 0.15 to 0.34). When the bleed actuation has a time-periodic component (about a nonzero mean) at St_{act} = 1.1 (Figure 4.6c), the time-averaged vorticity concentrations indicate that the separated shear layer is strongly deflected towards the surface, and compared to the base flow, it is significantly thicker and more curved within $x/c < 0.5$. Unlike the base flow, cross stream distributions of the time-averaged velocity show no evidence of reversed flow near the trailing edge. These changes in the flow field over the airfoil are accompanied by a significant increase in lift compared to the base flow (from C_L = 1.30 to 1.52). These data indicate that bleed actuation can effectively manipulate the vorticity layer over the surface and enable continuous variation between the flow states and aerodynamic loads in Figures 4.6b and c.

It is important to note that the time-averaged vorticity layer does not fully reflect the dynamics of the flow over the surface. This is apparent from cross stream distributions of the RMS fluctuations of the spanwise vorticity concentrations for each of the configurations (Figures 4.7a-c). The RMS fluctuations indicate strong dynamical interactions of vorticity concentrations above the surface as the time-averaged vorticity layer becomes thicker and ultimately detaches from the surface. The instantaneous flow field is discussed further in connection with Figure 4.14 below.

The details of the displacement of the surface vorticity layer by bleed actuation are investigated at low angles of attack before the base flow begins to separate at the trailing edge. Bleed is effected between the pressure and suction surfaces using three configurations in which the pressure side is sealed (*C1*) and has three (*C2*) and six (*C3*)

spanwise rows of ports (cf. Figure 4.3). Figures 4.8a-l show time-averaged raster plots of spanwise vorticity concentrations over the surface of the airfoil at $\alpha = 3°$, 5°, and 7° for the base flow and for each of the three bleed configurations. These data show that the base flow is fully attached at all three angles (Figures 4.8a, e, and i). In the absence of net bleed (*C1*, Figures 4.8b, f, and j), the surface vorticity layer thickens as the flow moves over the open ports on the suction surface, its cross stream width increases somewhat with angle of attack, and a secondary cross stream maximum of the spanwise vorticity appears (roughly) in the center of the vorticity layer (e.g., $0.35 < x/c < 0.65$ in Figure 4.8j). However, no reversed flow is detected as shown in the cross stream distributions of the streamwise velocity at the trailing edge (Figure 4.9). The cross stream spreading is accompanied by a small reduction in lift compared to the base flow (up to $\Delta C_L = -0.05 C_{L,0}$ at $\alpha = 7°$, cf. Figure 4.3) ostensibly as a result of streamwise pressure equalization between the upstream and downstream ports which imposes a slight adverse streamwise pressure gradient.

When (three) bleed rows are open on the pressure side (*C2*, Figures 4.8c, g, and k), the clockwise (CW) surface vorticity layer begins to gradually *deflect* away from the surface, and this deflection increases with α. The deflection is clearly visible by the appearance of a local cross stream maximum of the spanwise vorticity away from the surface. As shown in Figure 4.8g, the CW vorticity has a local cross stream maximum at the surface over most of the bleed array ($0.29 < x/c < 0.47$), but a clear secondary off-surface peak appears above it at $x/c > 0.40$. This peak continues to intensify downstream of the port array as the CW maximum over the surface diminishes and a layer of CW spanwise vorticity of lower magnitude appears just above the surface. It is remarkable

that this deflection progresses with increasing α without the appearance of reversed flow all the way through the trailing edge until $\alpha = 7°$ (Figure 4.9). As noted in in §3, a fundamental characteristic of quasi steady bleed is that in the absence of deliberate regulation, the intensity of the bleed can increase somewhat with the pressure difference across the bleed ports as a result of the increase in α. The present PIV data indicate that the magnitude of the bleed flow increases along the streamwise extent of the bleed ports, and the bleed speed at the downstream edge of the array is estimated to be $0.1U_\infty$, corresponding to $C_\mu = 2.5 \cdot 10^{-4}$. Considering the relatively low momentum associated with the bleed, it appears that its primary function is to displace the low-speed (but higher momentum) fluid near the surface of the airfoil by forming a (relatively thin) wall layer along the surface. As indicated in Figure 4.8k, the flow is extremely susceptible to the actuation, which leads to bifurcation of the CW vorticity layer within the domain $0.30 < x/c < 0.45$, ostensibly as a result of induced local changes in the streamwise pressure gradient (cf. §3.2), and to its ultimate deflection downstream for $x/c > 0.45$. The deflected vorticity layer spreads rapidly in the cross-stream direction, and its width at the trailing edge at $\alpha = 7°$ more than triples (to $0.2c$) compared to the base flow. When $\alpha = 7°$, the vorticity layer appears to be detached from the surface as is evident by the appearance of a thin layer of CCW vorticity on the surface that is driven by a narrow cross stream domain of reversed flow visible in the velocity distribution near the trailing edge (Figure 4.9). As the inlet area on the pressure surface is increased (*C3*, Figures 4.8d, h, l), the bifurcation of the surface CW vorticity layer moves upstream. The vorticity layer becomes partially detached at $\alpha = 7°$, and a layer of CCW vorticity forms over the surface. These changes in the flow are accompanied by a substantial reduction

in lift and increase in the nose-down pitching moment ($\Delta C_L/C_{L,0}$ = -0.51, -0.52, and -0.51, and $\Delta C_M/C_{M,0}$ = -0.44, -0.44, and -0.41, at α = 3°, 5°, and 7°, respectively).

The susceptibility of the flow over the airfoil to bleed actuation may be the result of a local instability owing to the actuation. Figures 4.10a-b show cross-stream distributions of the streamwise velocity and spanwise vorticity, respectively, at x/c = 0.47 in Figures 4.8e and g. These distributions show that vorticity extrema *off the surface* at $\tilde{y}/c$ = 0.01 and 0.02 correspond to distortion of the time-averaged cross-stream distribution of the streamwise velocity and the appearance of inflection points in $u(\tilde{y})$. Although the stability of the time-averaged flow was not explored as part of the present investigations, these inflection points may be indicative of an inviscid shear layer instability (e.g., Ho and Huerre, 1984). This finding suggests that the bleed-induced bifurcation and subsequent off-surface deflection of the vorticity layer is the result of amplification of this inviscid instability, similar to the growth of such instabilities in wall jets and free shear layers (e.g., Huerre and Monkewitz, 1985, Amitay and Cohen, 1997). It is also conjectured that the response of the base flow to time-dependent bleed actuation that is accompanied by quasi-steady bleed and leads to the time-averaged deflection of the detached vorticity layer towards the surface (cf. Figure 9c) may be related to the same stability mechanism. The bifurcation of the vorticity layer in the presence of time-periodic actuation is discussed in more detail in §4.4.

4.3. Time-Dependent Bleed Actuation

The effects of bleed on the flow are demonstrated by comparing color raster plots of instantaneous concentrations of spanwise vorticity for the base airfoil when flow is fully attached (Figure 4.11a) to flow over configuration *C3* at α = 3° (Figure 4.11d). While

the vorticity layer of the base flow is concentrated directly above the surface, quasi-steady bleed leads to the formation of a train of discrete vortices having a nominal passage period $\tau = 0.21T_{conv}$ or $St = 4.76$ (the passage frequency of the vortices is 357 Hz). These dynamics are not captured by the time-averaged flow field (Figure 4.8d), which exhibits the formation of a secondary cross stream maximum of the spanwise vorticity above the surface. The evolution of these nominally spanwise vortices indicates that the bleed destabilizes the attached boundary layer, and the formation frequency is probably associated with concomitant modulation dynamics of the quasi-steady bleed which are clearly affected by changes in the local pressure above the bleed ports. The actuation has similar effects at $\alpha = 5°$ and 7° (Figures 4.11e and f), which also show that the cross stream scale of the discrete vortices increases with angle of attack ostensibly due to the increase in flux of CW vorticity and in the strength of the actuation. As the scale of these vortices increases, their passage frequency decreases slightly to $St = 4$ at $\alpha = 7°$. These data show that the apparent time-averaged "deflection" of the vorticity layer from the surface is in fact a manifestation of the increase in the cross stream scale of the discrete vortices, but the vorticity layer is in fact bounded from below by the surface.

The effect of the quasi-steady actuation on the dynamics of the vorticity concentrations on the suction side of the airfoil is indicative of the receptivity of the flow to time-dependent actuation. These effects are first investigated using a step change in bleed by louver activation between $\Lambda = 0$ and 1 at $\alpha = 16°$ as demonstrated by measurements of the aerodynamic loads (Figure 4.12) and of the instantaneous flow field over the airfoil (using time-resolved PIV, Figure 4.13, where the timing of the PIV

frames is marked in Figure 4.12). Bleed is actuated using the louvered ports of the pressure surface and one row of ports on the suction surface at $0.03 < x/c < 0.04$. Prior to the onset of actuation, the flow is nominally attached through mid-chord (Figure 4.13a for which $C_L = 1.16$ and $C_M = -0.05$). Bleed actuation commences in Figure 4.13b ($t/T_{conv} = 8$) and interacts with the vorticity layer to form a large-scale concentration of CW vorticity (Figure 4.13e, $t/T_{conv} = 13$). As shown in Figure 4.12, the process of the formation of this vortex (e.g., Figure 4.13d, $t/T_{conv} = 11$) leads to an increase in C_L to 1.30 and apparently to an increase in suction pressure aft of $c/4$ that is manifested by an increase in the nose-down pitching moment ($C_M = -0.09$). The subsequent formation and advection of this large-scale vortex (Figure 4.13e) enhances the accumulation of CW vorticity over the airfoil and increases C_L to a maximum of 1.47 and the nose-down moment to $C_M = -0.25$ (Figure 4.12e). Because C_M is measured relative to $c/4$, it peaks when the vorticity concentration advects over the trailing edge, i.e. slightly after the occurrence of the peak in lift, which depends primarily on the pressure distribution near the leading edge. The bleed continues ($\Lambda = 1$) in Figures 4.13e-h and leads to further increase in the cross stream scale of the CW vortex as it is advected towards the trailing edge. The bleed is terminated at $t/T_{conv} = 25$ (Figure 4.13h), and C_L decreases to 0.76 before the vorticity layer collapses onto the surface and the flow becomes attached through $x/c = 0.5$ (Figure 4.13j, $t/T_{conv} = 29$), and C_L and C_M relax to their original levels.

These data indicate that the transient increase in lift can be exploited by repeated, i.e. time-periodic, actuation for a sustained change in the aerodynamic loads (as demonstrated in connection with Figure 4.6c). In fact, the interaction between continuous time-periodic bleed flow and the cross-stream leads to the periodic formation

of large-scale vortices that contribute to the accumulation of CW vorticity over the airfoil and thereby a net increase in lift during the actuation cycle, and consequently, in the time-averaged lift. The mechanism by which this process occurs is illustrated in Figures 4.14a-p that show raster plots of instantaneous concentrations of the spanwise vorticity during two actuation cycles. Even though the data in Figure 4.11 suggests that the flow is receptive at characteristic frequencies St = 4-5, the actuation frequency is selected to be St_{act} = 1.1 because of the limited frequency range of the present piezoelectric louvers. Figures 4.14i-iii show for reference a sequence ($\Delta t/T_{conv}$ = 0.11 apart) of instantaneous PIV images of the flow over the (sealed) base airfoil. At the onset of the cycle of the time-periodic bleed (Figure 4.14a, t/T_{act} = 0), the vorticity layer is detached from the surface near x/c = 0.12, and a concentration of CW vorticity downstream induces a layer of CCW vorticity at the surface beneath it. The disruption of the detached vorticity layer by the bleed results in a rollup of another concentration of CW vorticity upstream of the vortex in Figure 4.14a (Figures 4.14b-d, t/T_{act} = 0.12 to 0.37) that forms a braid-like domain with the downstream vortex (Figure 4.14d). This vortex continues to grow while it is advected downstream ($u_{celerity}/U_{\infty} \approx 0.35$) and becomes disconnected from the surface vorticity layer upstream as it entrains CCW vorticity from underneath (Figures 4.14e-h t/T_{act} = 0.50 to 0.87), while the CW surface vorticity layer upstream remains *fully attached*. The CW vortex increases in scale (its diameter is about 0.3c by x/c = 0.5) while the surface CW vorticity layer continues to migrate downstream and remain attached due to induced motions by the CCW vorticity concentration in the upstream segment of the isolated vortex (e.g., Figures 4.14e-g). It is remarkable that these unsteady motions can overcome the nominally-adverse local pressure gradient on the suction surface of the

airfoil. Furthermore, the data in Figure 4.14 indicate that the increase in lift as a result of the time-periodic actuation is associated in part with the time-periodic formation and slow advection of the large-scale isolated CW vortex (that is reminiscent of a dynamic stall vortex, although the airfoil is stationary). The periodic shedding of this vortex is accompanied by a momentary decrease in lift, although the time-averaged lift is clearly higher than that of the baseline flow (cf. Figure 4.4a).

As noted above, the actuation frequency is selected to be within the receptivity range of the base flow (based on measurements of the global lift forces). However, the present PIV measurements indicate that the characteristic time constant that is associated with the attachment of the surface vorticity layer following the formation and advection of the CW vortex that is engendered by the actuation is actually *longer* than the actuation period. The onset of the next bleed cycle coincides with Figure 4.14i ($t/T_{act} = 1$). Although the bleed flow disrupts the surface vorticity layer near the leading edge, there is little visible effect in Figures 4.14j-l (t/T_{act} = 1.12 to 1.37) since the vorticity layer is dominated by the large-scale vortex that is still visible at the downstream end of the measurement domain. Perhaps the most prominent feature in Figures 4.14o and p (t/T_{act} = 1.74 and 1.87, respectively) is the onset of detachment of the surface vorticity layer before it interacts again with the bleed at the beginning of the next actuation cycle at $t/T_{act} = 2$ (corresponding to Figure 4.14a). *These data indicate that the actuation period is approximately half the characteristic period of the transitory attachment of the surface vorticity layer following the formation and advection of the large scale CW vortex.* In fact, when the time-periodic bleed actuation is applied at $St_{act} = 0.53$, the time-averaged lift is $C_L = 1.46$ compared with 1.52 at $St_{act} = 1.1$ (cf. Figure 4.5a).

4.4. Manipulation of Vorticity Flux using Time-Dependent Bleed Actuation

Changes in the transport of vorticity concentrations due to the interaction of time-periodic bleed with the cross flow over the airfoil are elucidated by comparing corresponding distributions of spanwise vorticity and vorticity flux. Figure 4.15a (based on the data in Figure 4.14) shows that transient advection of the large CW vortex and the subsequent deflection (or attachment) of the upstream vorticity layer near the leading-edge are manifested in the time-averaged flow by deflection of a thick band of CW vorticity ($\Delta y/c \approx 0.2$ by $x/c = 0.5$) towards the surface (cf. Figure 4.6c). Figure 4.15a also shows a thin layer of "trapped" of CCW vorticity along the suction surface ($\Delta y/c \approx 0.01$). The *instantaneous* distribution of spanwise vorticity concentrations in Figure 4.15b (also Figure 4.14c) reveals that the formation and evolution of the CW vortex centered at $x/c = 0.25$ following the onset of the bleed during the actuation cycle induces a layer of CCW vorticity along the surface that accompanies the detachment of the CW vortex from the surface. The time-averaged distribution of the flux of spanwise vorticity (Figure 4.15c) demonstrates countercurrent adjoining upper and lower domains of downstream and upstream advection of CW vorticity concentrations, respectively, that are bounded from below by a thin domain of upstream advection of CCW vorticity concentrations over the surface. The instantaneous raster plots of vorticity and vorticity flux (Figures 4.15b and d) exhibit countercurrent vorticity flux within a domain of upstream flux of CW vorticity that is bounded from above by streamwise flux of CW vorticity and from below by upstream flux of CCW vorticity (circled in Figures 4.15b and d, note that flow within the blue dashed contour in Figure 4.15d marks a domain in which $u(x, y) < 0$).

Some aspects of the dynamic effects of time-periodic bleed on the spatial and temporal characteristics of advection of vorticity concentrations over the suction surface and, in particular, the bifurcation of the vorticity layer that was discussed in connection with Figure 4.8 are analyzed using proper orthogonal decomposition (POD) of the vorticity flux. The present analysis follows the formulations of Sirovich (1987) and Adrian and Westerweel (2011). The field of streamwise flux of spanwise vorticity concentrations $\Psi(x, y, t) = u(x, y, t)\cdot\zeta(x, y, t)$ measured in N successive PIV snapshots is represented as

$$\Psi(x, y, t_k) = \sum_{i=1}^{N} c_i(t_k)\phi_i(x, y) \tag{4.1}$$

where $\phi_i(x, y)$ are the orthogonal basis functions or spatial modes, and $c_i(t_k)$ are the temporal coefficients. The fluctuating components of the field are concatenated into a single matrix and its autocovariance matrix, and eigenvalues λ_i are computed. This method yields N temporal coefficients that each scale the contribution of the modes, where the modes are arranged by the eigenvalue in descending order of energy content. The Ψ field of any snapshot may be partially reconstructed using an arbitrary number of modes.

The decomposition is applied to the PIV measurements at $\alpha = 16°$ with the bleed configuration of Figure 4.14 using a set of 2,736 instantaneous images sampled at a rate of 2 kHz (resulting in a record that is $103T_{conv}$ or $114T_{act}$ long). The reconstruction of a characteristic snapshot of $\Psi(x, y, t)$ is shown in Figure 4.16 (this field is derived from that data of Figure 4.14e). A snapshot of the vorticity flux in the presence of bleed (Figure 4.16a) is reconstructed using the three most energetic modes that capture 25% of the total energy (Figure 4.16b), 17 modes capturing 50% of the energy (Figure 4.16c), 77

modes capturing 75% of the energy (Figure 4.16d), and the entire set of 2,736 modes that capture 100% of the energy (Figure 4.16e). Figure 4.16a shows the large scale CW vortex that forms time-periodically at half the frequency of the bleed actuation and is centered at $x/c = 0.35$. The three highest-energy modes (Figure 4.16b) capture large-scale features of the vorticity flux that are not obscured by small-scale motions. These modes reveal the bifurcation of the vorticity layer downstream of the actuation ports (marked by a triangle) that leads to the rollup of the large-scale CW vortex and to the accumulation of vorticity as it is advected over the surface. This bifurcation is associated with the time-averaged deflection of the vorticity layer away from the surface as shown in Figure 4.15a. The emergence of smaller-scale features with additional spatial modes (Figure 4.16c) reveals more details within the core of the bifurcated vortex as well as opposite sense flux (contributed either by streamwise advection of CCW vorticity or upstream advection of CW vorticity). More features of the large-scale vortex emerge with the addition of higher order (energetic) modes (Figures 4.16c-d). The details of these flux concentrations are only fully resolved with the complete set of modes (Figure 4.16e). It might be argued that the dynamics of the large-scale features of the flow can be captured by 15 or so modes.

The four most energetic POD modes of the spanwise vorticity flux over the suction surface in the base flow (20% of the energy) and in the presence of time-periodic bleed (29%) are compared in Figures 4.17a-d and 4.17e-h ($St_{act} = 1.1$), respectively, using color raster plots. The first mode of the base flow (Figure 4.17a, 7.2% of the energy) captures a small (0.03c in diameter) domain of intense flux of CW vorticity near the leading edge that is associated with vorticity production within the attached boundary layer. In the

presence of bleed, the structure of the first mode (Figure 4.17e, 12.8% of the energy) is profoundly different than in the base flow and is affected by the receptivity of the flow to bleed actuation due to the proximity of the bleed outlet to the domain of concentrated flux energy identified in the first base mode (Figure 4.17a). The bifurcated vorticity layer is associated with adjacent layers of positive and negative fluxes that lift the surface layer into the cross flow. It is conjectured that these opposite sense fluxes are associated with the CW vorticity layer that forms the large scale vortex and the CCW vorticity that is lifted off the surface by the induced reversed flow and ultimately imposes the attachment of the vorticity layer upstream of the large CW vortex (cf. Figure 4.14e). The second mode of the base flow (Figure 4.17b, 6.3% of the energy) exhibits two layers of opposite sense fluxes that intensify in the streamwise direction, spread in the cross direction, and appear to lift off the surface at $x/c \approx 0.4$ (cf. Figure 4.6a). Similar to the discussion of the first mode in the presence of bleed, the separation of the base flow is accompanied by upstream flux of CW vorticity. The second bleed mode (Figure 4.17f, 7.8% of the energy) shows more details of the positive flux near the surface of the airfoil. It is interesting to note that the negative flux associated with the CW vorticity layer appears to migrate nearly to the leading edge, suggesting the bifurcation of the vorticity layer by the bleed is associated with counter current instability above the bleed port. Modes three and four of the base flow (Figure 4.17c and d, 3.6% and 2.9% of the energy, respectively) exhibit both cross-stream and streamwise segmentation in opposite sense vorticity flux within $0.18 < x/c < 0.32$ and $\Delta y/c = 0.05$ above the surface. These higher-order bifurcations of the vorticity layers are associated with the formation of small-scale vorticity concentrations and motions that are visible in Figures 4.14i-iii. Such higher-

order bifurcations are also visible in modes three and four in the presence of bleed (Figures 4.17g and h, 4.3% and 4.1%, respectively) but are spread to higher elevations above the surface.

It is instructive to consider the spectral content of the time histories of the temporal coefficients of the spatial modes. Figure 4.18 shows power spectra of each of the first four temporal coefficients in the absence and presence of bleed actuation. While the spectral content of the first coefficient $c_{1\text{-base}}$ of the base flow appears to be nearly featureless and the power is nearly uniformly distributed over all spectral components, $c_{1\text{-act}}$ is significantly higher in magnitude (up to nearly 1,000-fold) and exhibits several prominent spectral peaks at $St = 0.13$, at the actuation frequency $St_{act} = 1.1$, and at its first subharmonic. The spectral content of $c_{2\text{-base}}$ exhibits a broad spectral peak at $St = 0.1$ along with weaker peaks in its second and third harmonics that appear to be associated with the two counter layers of vorticity flux in the separating base flow that are captured by the second spatial POD mode discussed above (cf. Figure 4.17b). It is interesting to note that while the spectral content of $c_{2\text{-base}}$ is higher than $c_{1\text{-base}}$ for $St < 0.4$, it diminishes significantly for $St > 2$ such that the total spectral power of each coefficient is 24.25 and 26.13, respectively. The low frequency spectral peaks are not as pronounced in $c_{2\text{-act}}$ which appears to be dominated by peaks at the actuation frequency and its first subharmonic ($St_{act} = 0.56$) as a result of the bifurcation of the vorticity layer above the bleed port (cf. Figure 4.17f). The spectral content of $c_{3\text{-base}}$ and $c_{4\text{-base}}$ are similar to $c_{1\text{-base}}$ while the corresponding spectra of $c_{3\text{-act}}$ and $c_{4\text{-act}}$ have spectral peaks at the actuation frequency and its higher harmonics indicating the role of the actuation in the formation of the counter layers of vorticity flux (cf. Figures 4.17g and h). Of particular note is the evolution of the spectral band between the actuation

frequency and its subharmonic between $c_{3\text{-act}}$ and $c_{4\text{-act}}$ that appears to be associated with the evolution of the multiple counter layers of vorticity flux that are effected by the actuation in Figures 4.17g and h. These layers are indicative of the attachment of the vorticity layer upstream of the time-periodic large CW vortices and contribute to the effectiveness of the bleed across a wide range of actuation frequencies (cf. Figure 4.5).

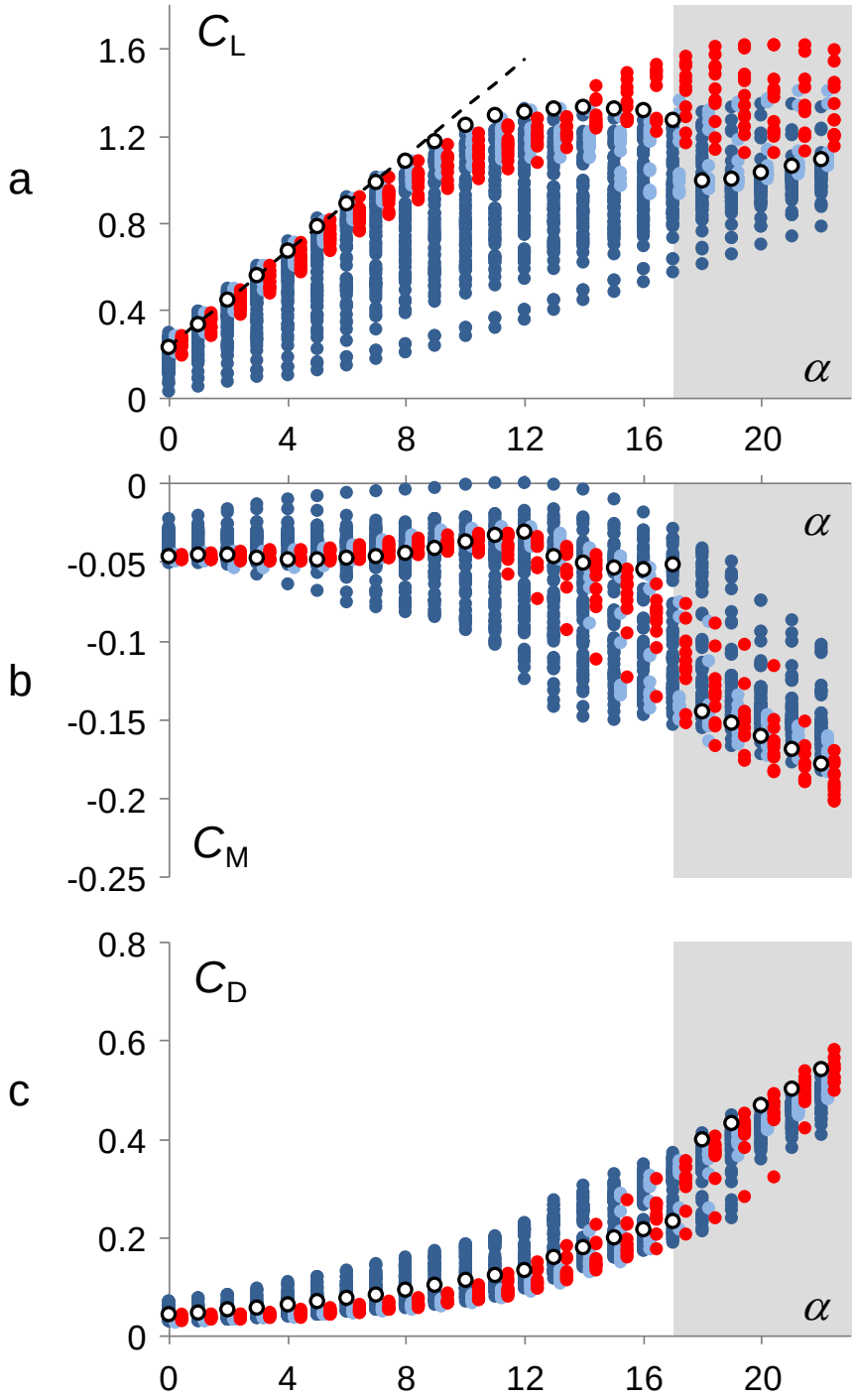

Figure 4.1. Variation of C_L (a), C_M (b), and C_D (c) with angle of attack for the base airfoil (○), $\Lambda = 0$ (●), quasi-steady bleed at $\Lambda = 1$ (●), and time-periodic bleed (●). For clarity, the clusters of data points $\Lambda = 0$ (●) and time-periodic bleed (●) are slightly offset to the right at each angle of attack. Thin airfoil theory lift $C_L = 2\pi\alpha$ (offset by 0.25 to account for camber) is shown for reference in (a) using a dashed line. The range of post-stall α is shaded in gray.

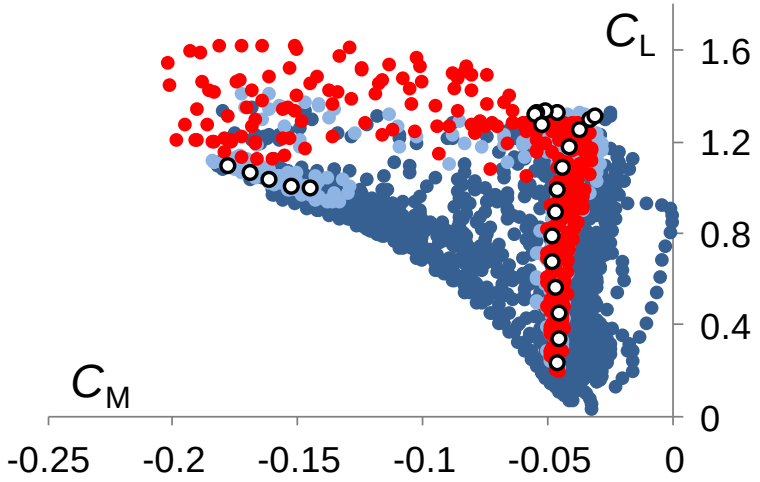

Figure 4.2. Joint distribution of C_L and C_M. Symbols as in Figure 4.1.

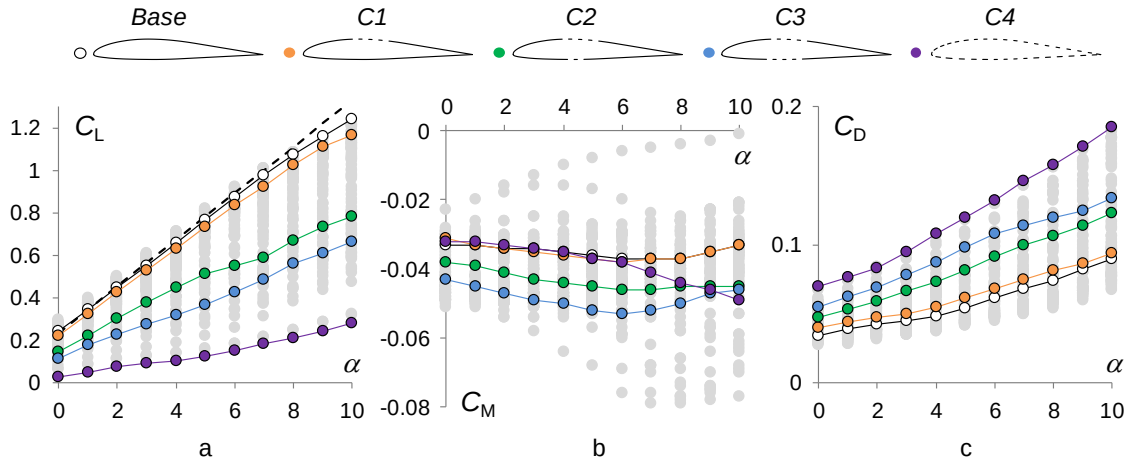

Figure 4.3. Variations of C_L (a), C_M (b), and C_D (c) with α for the base airfoil (○) and for quasi-steady bleed configurations *C1* (●), *C2* (●), *C3* (●), and *C4* (●). Data for other configurations (Figure 4.1) are shown in gray, and $C_L = 2\pi\alpha$ (with an offset of 0.25) is shown for reference using a dashed line.

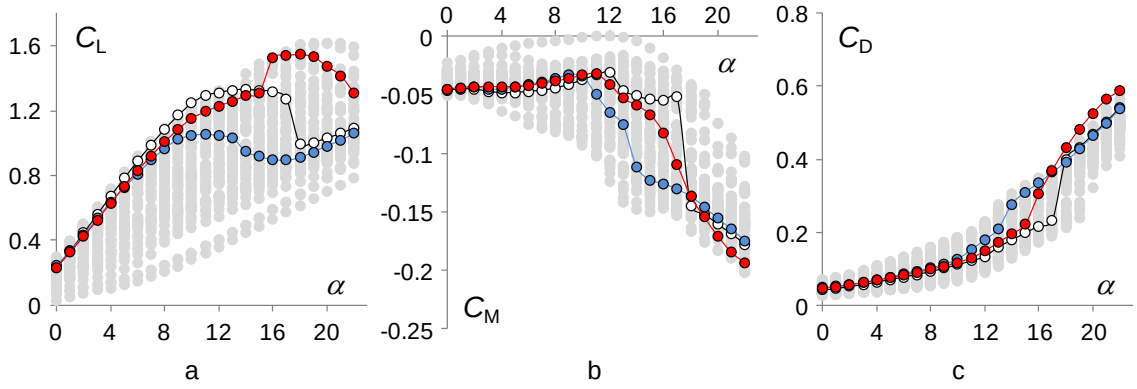

Figure 4.4. Variation of C_L (a), C_M (b), and C_D (c) with α for the base airfoil (○), quasi-steady bleed at $\Lambda = 1$ (●), and time-periodic bleed (●, $St_{act} = 1.1$) with the bleed ports at $0.03 < x/c < 0.04$. Data from Figure 4.1 are shown in gray for reference.

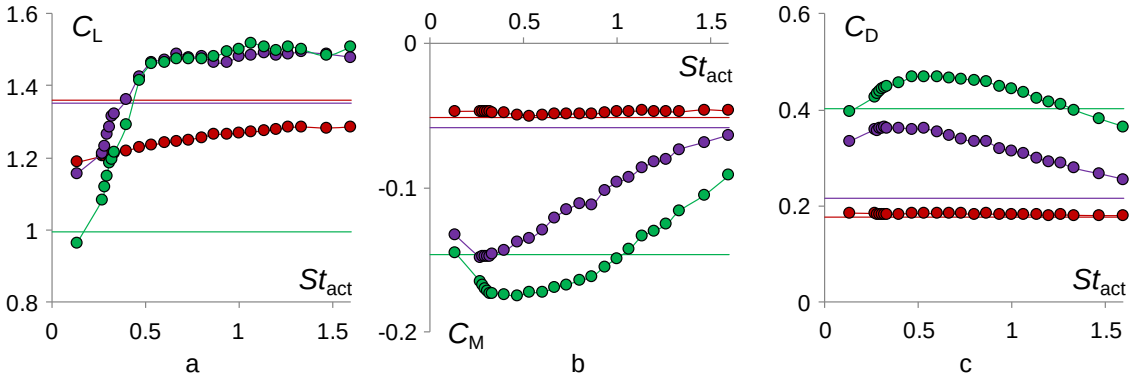

Figure 4.5. Variation of C_L (a), C_M (b), and C_D (c) with louver actuation frequency at $\alpha = 14°$ (●), 16° (●), and 18° (●). Base flow levels are shown using solid lines.

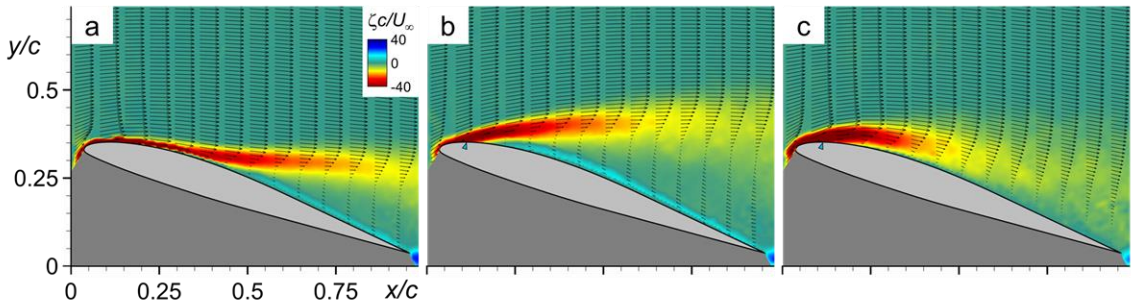

Figure 4.6. Time-averaged distributions of spanwise vorticity concentrations (color raster plots) and velocity vectors at $\alpha = 16°$ in flow over the base airfoil (a) and in the presence of bleed actuation: $\Lambda = 1$ (b), and time-periodic at $St_{act} = 1.1$ (c). The bleed outlet on the suction surface is indicated with a blue triangle.

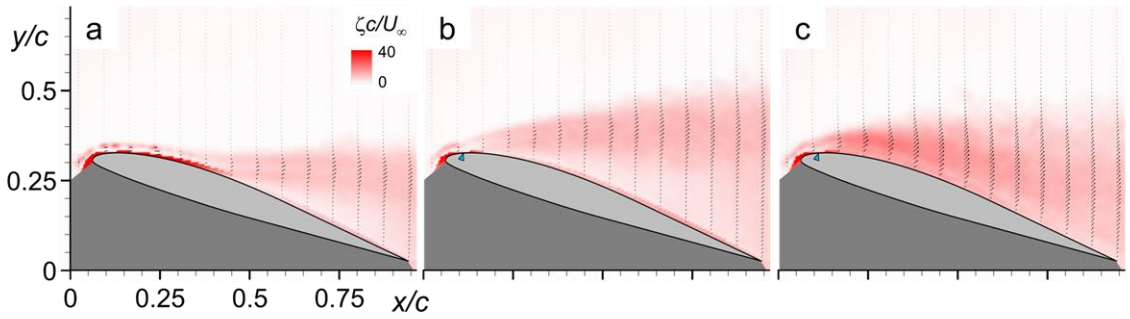

Figure 4.7. As in Figure 4.6, RMS vorticity fluctuations.

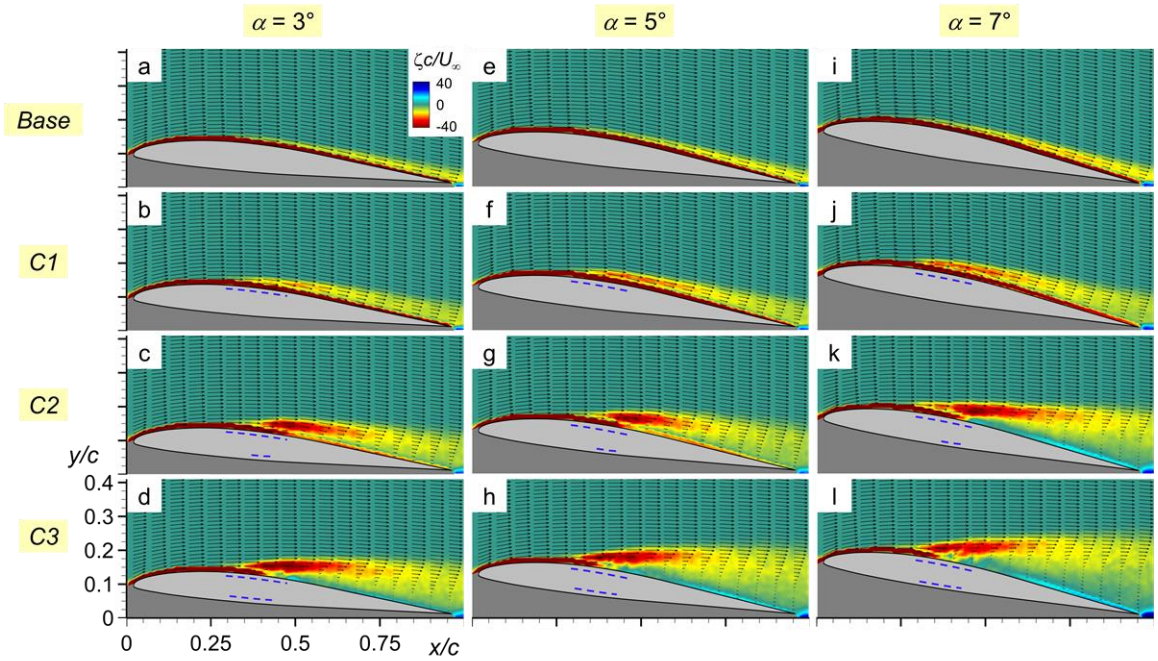

Figure 4.8. Color raster plots of spanwise vorticity concentrations and cross stream distributions of velocity vectors of the time-averaged flow at α = 3°, 5°, and 7° for the base airfoil (a, e, i) and with bleed configurations *C1* (b, f, j), *C2* (c, g, k), and *C3* (d, h, l), respectively. The locations of open ports are shown schematically using dashed lines.

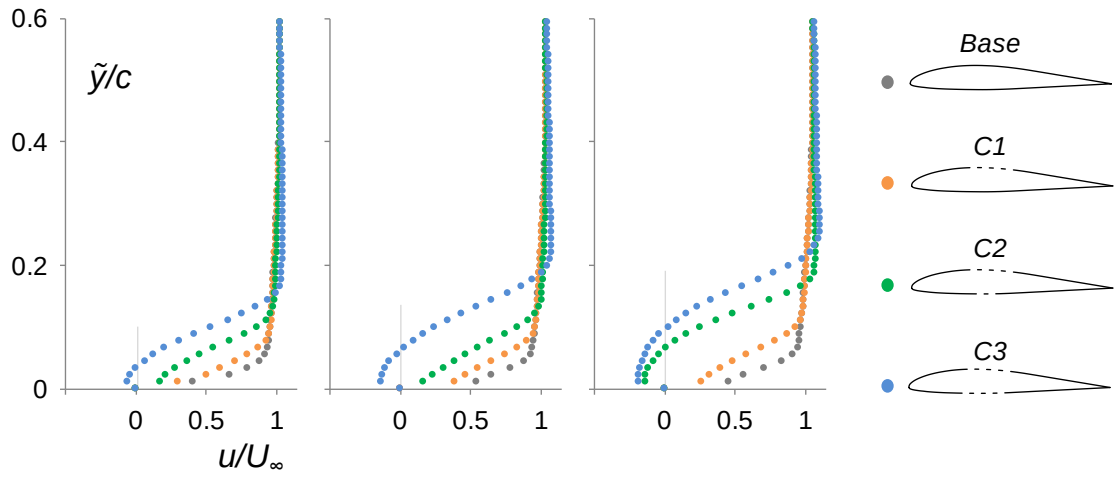

Figure 4.9. Cross stream distributions of the streamwise velocity on the suction surface at the trailing edge of the airfoil (corresponding to Figure 4.8) at α = 3°, 5°, and 7°: base airfoil (●) and bleed configurations *C1* (●), *C2* (●), and *C3* (●). The cross stream coordinate $\tilde{y}/c$ is measured relative to the trailing edge at each angle.

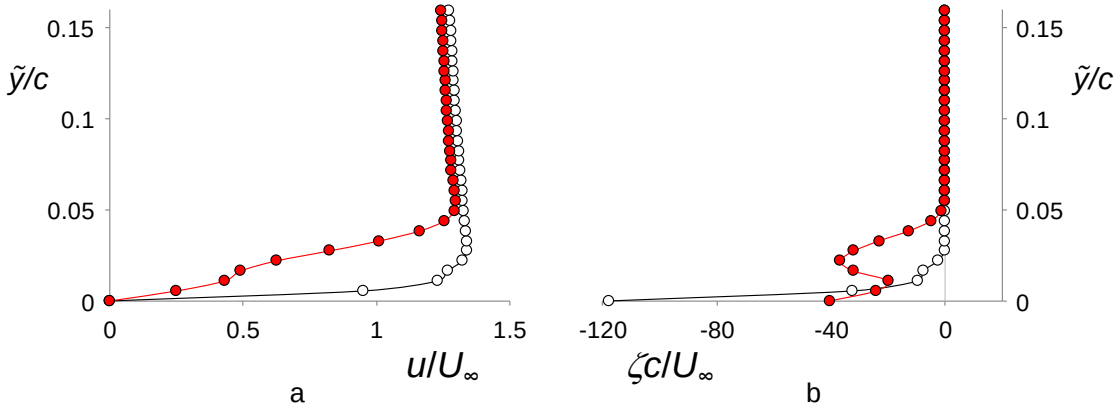

Figure 4.10. Distributions of streamwise velocity (a) and spanwise vorticity (b) for the base flow (—) and in the presence of bleed (configuration *C2*, —) measured at $\alpha = 5°$, $x/c = 0.47$ (cf. Figures 4.8e, g). The cross stream coordinate $\tilde{y}/c$ is measured relative to the airfoil surface.

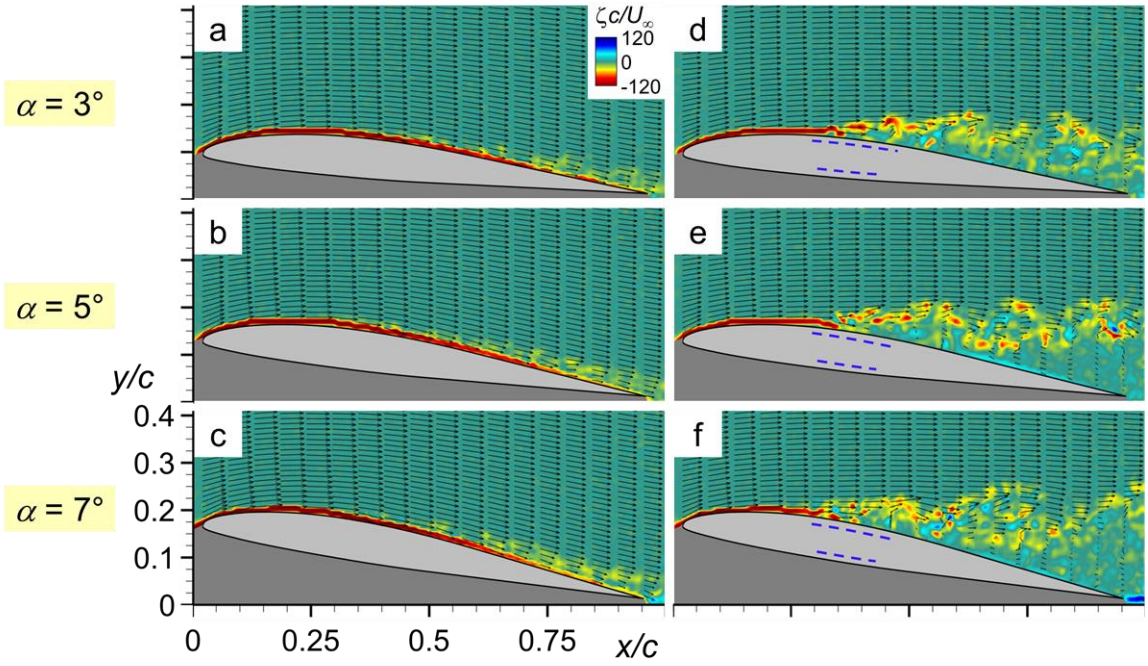

Figure 4.11. Instantaneous distributions of spanwise vorticity concentrations and velocity vectors in the cross stream plane at α = 3°, 5°, and 7° for the base airfoil (a-c) and using configuration *C3* (d-f).

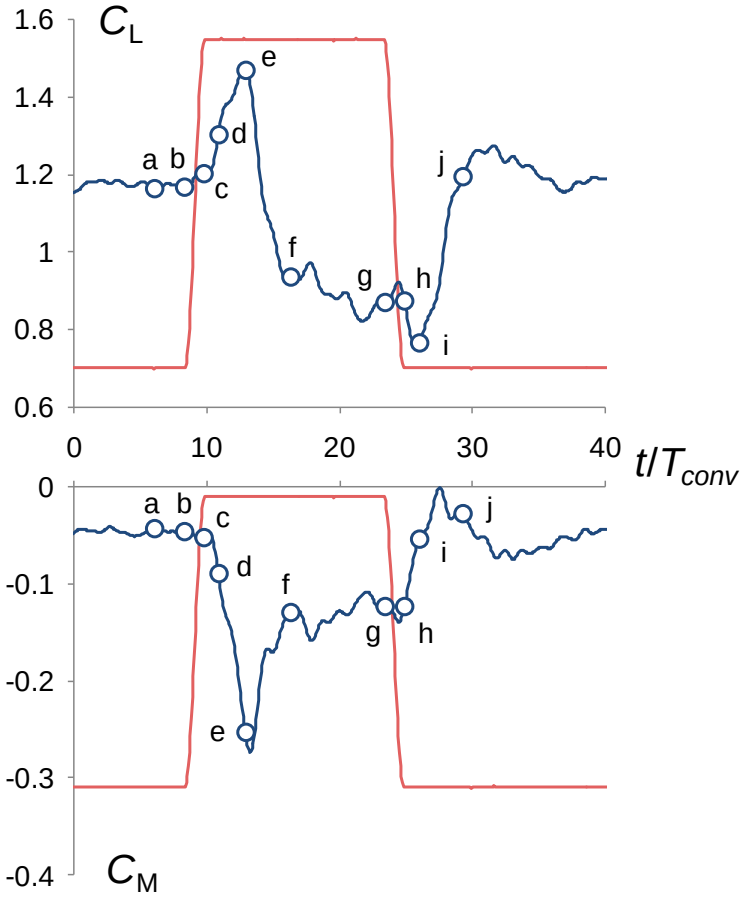

Figure 4.12. Variations in lift and pitching moment (—) at α = 16° in response to a step change in bleed actuation between $\Lambda = 0$ and 1. The actuation waveform is shown schematically (—), and the indicated time steps correspond to Figure 4.13.

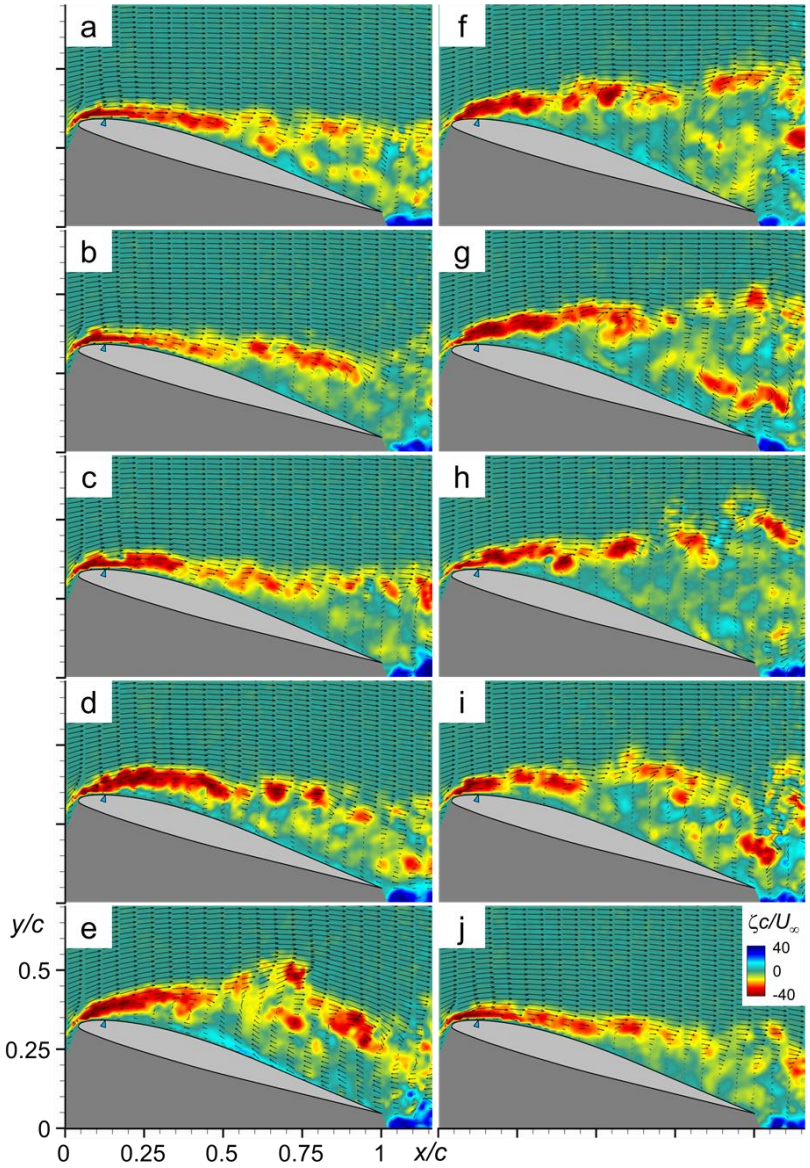

Figure 4.13. Instantaneous spanwise vorticity concentrations (color raster plots) and velocity vectors in flow over the airfoil at $\alpha = 16°$ during the onset and termination of step bleed actuation. Timing of the frames is indicated on the actuation waveform in Figure 4.12: $t/T_{conv} = 6$ (a), 8 (b), 10 (c), 11 (d), 13 (e), 16 (f), 23 (g), 25 (h), 26 (i), and 29 (j).

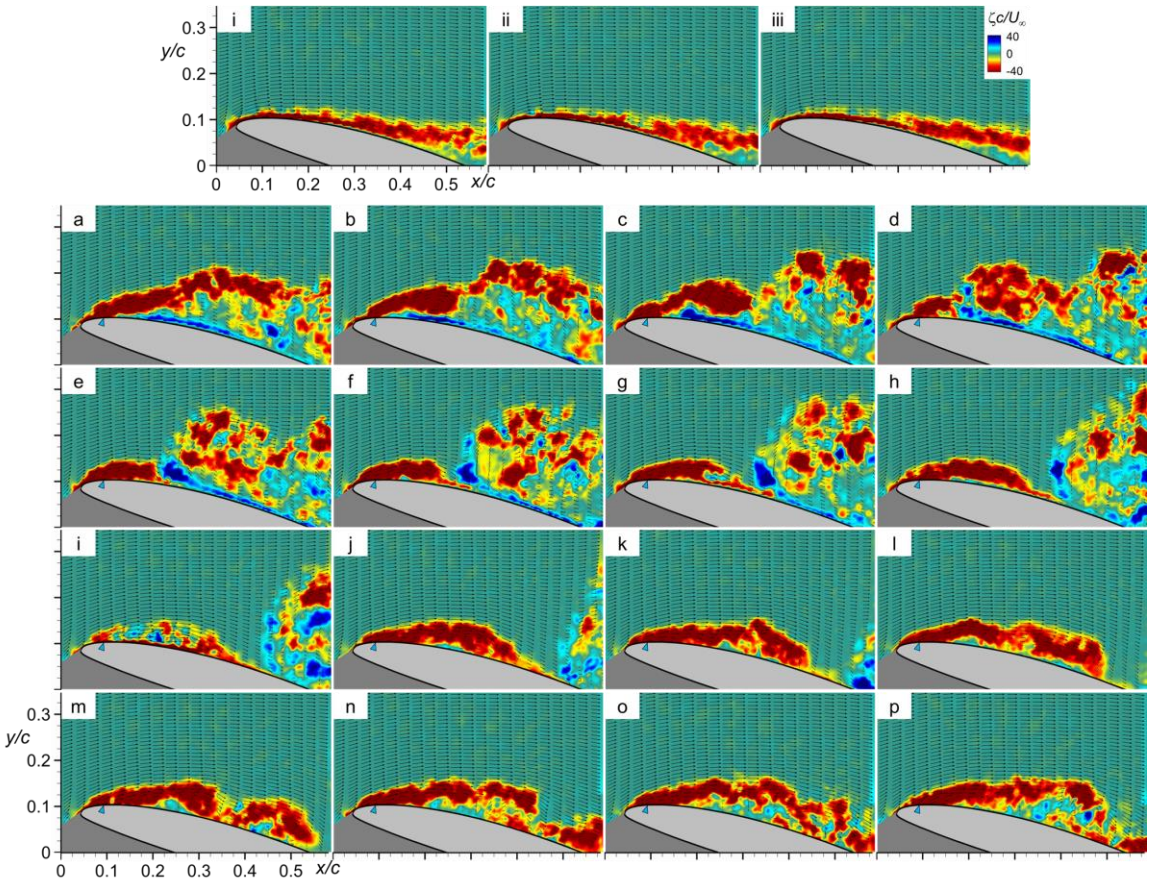

Figure 4.14. Color raster plots of instantaneous spanwise vorticity concentrations and cross stream distributions of velocity vectors over the airfoil at $\alpha = 16°$. Successive frames of the base flow ($\Delta t = 0.11T_{conv}$ apart) are shown in i, ii, and iii and following the onset of bleed during two cycles of the time-periodic actuation cycle ($St_{act} = 1.1$): $t/T_{act} = 0$ (a), 0.12 (b), 0.25 (c), 0.37 (d), 0.50 (e), 0.62 (f), 0.75 (g), 0.87 (h), 1 (i), 1.12 (j), 1.24 (k), 1.37 (l), 1.49 (m), 1.62 (n), 1.74 (o), and 1.87 (p). The onset of bleed occurs in (a) and (i).

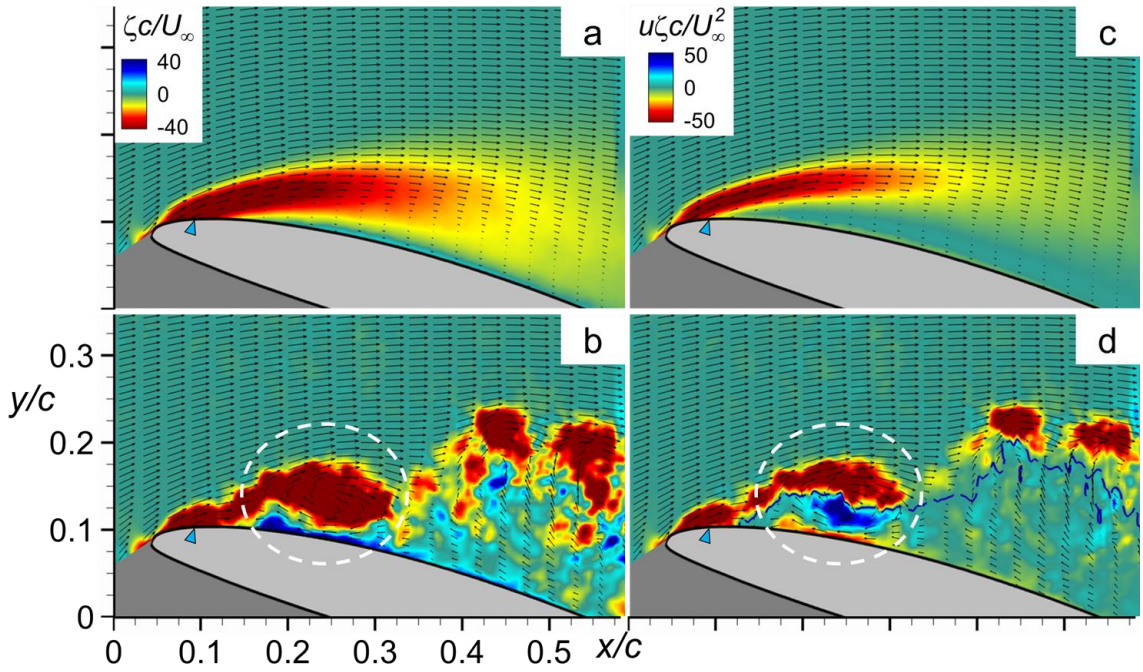

Figure 4.15. Color raster plots (superposed with velocity vectors) of: time-averaged (a) and instantaneous (b, $t/T_{act} = 0.25$) spanwise vorticity concentrations, along with time-averaged (c) and instantaneous (d, $t/T_{act} = 0.25$) spanwise vorticity flux over the airfoil at $\alpha = 16°$ and in the presence of time-periodic bleed. The streamwise velocity $u < 0$ within the domain bounded by the blue dashed contour and the airfoil in (d). The CW vortex formed by the interaction of the bleed and outer flow is marked by the dashed white lines in (b) and (d).

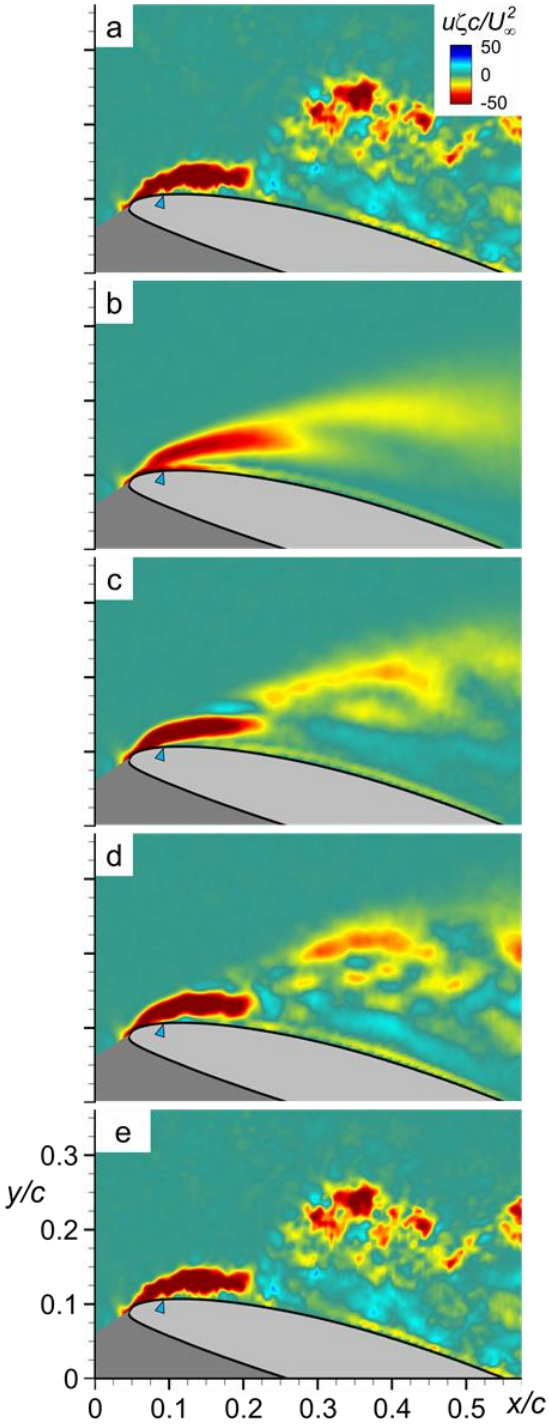

Figure 4.16. Reconstructions of an instantaneous distribution of spanwise vorticity flux in the presence of bleed (a) using POD modes: b) 3 modes (25% of total energy); c) 17 modes (50%); d) 77 modes (75%); and e) 2,736 modes (100%).

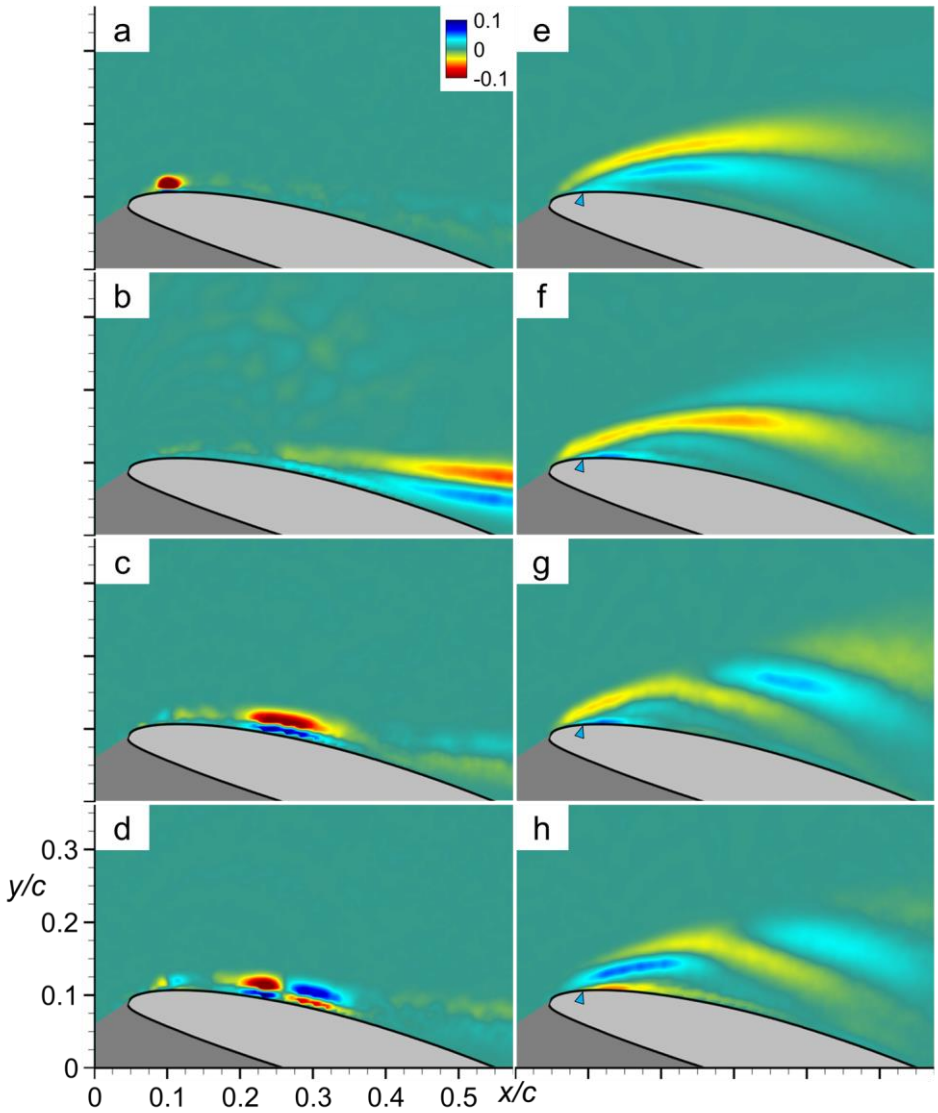

Figure 4.17. Color raster plots of the first four (most energetic) spatial POD modes of the streamwise flux of spanwise vorticity over the suction surface for the base airfoil (a-d) and in the presence of bleed (e-h, St_{act} = 1.1).

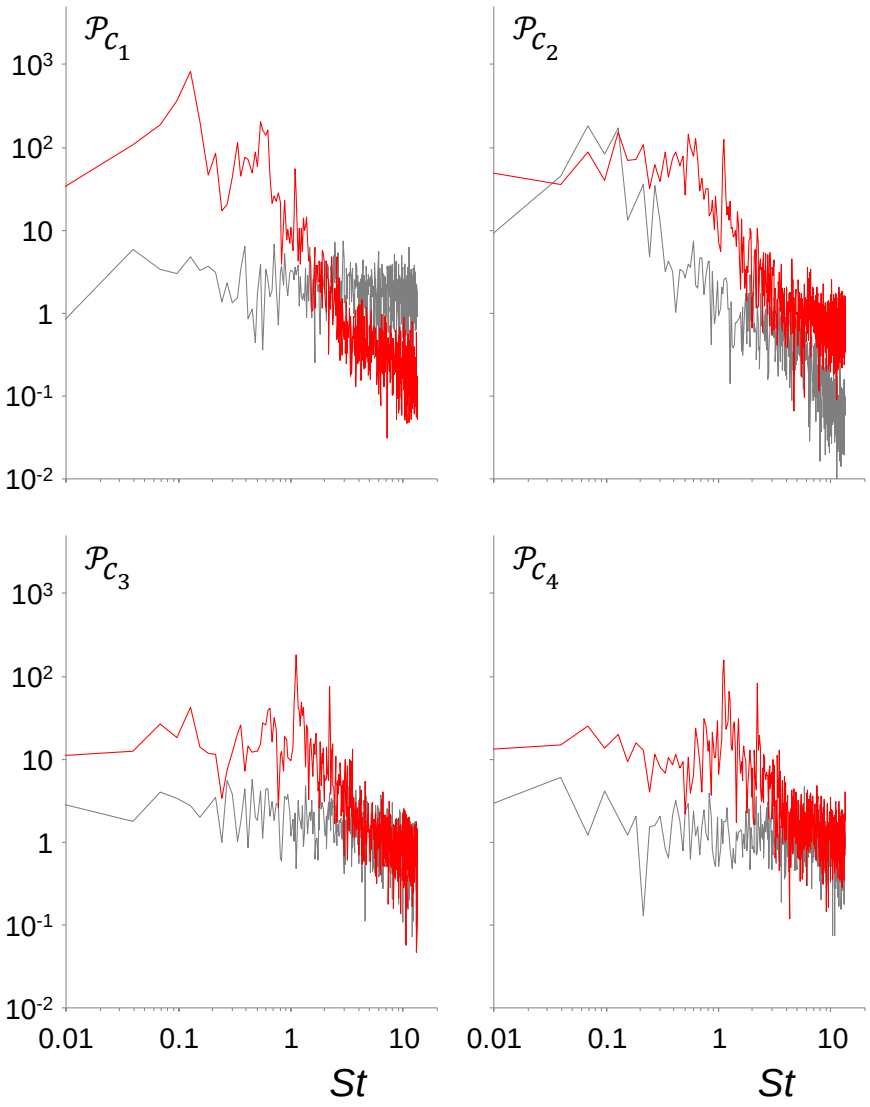

Figure 4.18. Normalized power spectra of the time coefficients of the POD modes for the base flow (—) and in the presence of bleed (—).

CHAPTER V

IMPROVED PITCH STABILITY AND LIFT HYSTERESIS BY BLEED ACTUATION ON A PITCHING AIRFOIL

This chapter extends the application of bleed-effected control to a dynamic platform, namely an airfoil oscillating in pitch about its quarterchord. The first section compares the theoretical unsteady lift and pitching moment to experimental results for validation and characterizes dynamic stall on the base airfoil. The second section examines the effects of bleed on the dynamic stall process and on the regulation of vorticity concentrations during quasi-unsteady pitch, and proper orthogonal decomposition is used to understand how bleed modulates the spatial and temporal distributions of vorticity flux in the wake that lead to changes in the global aerodynamic loads. The final section demonstrates that bleed has a profound effect on the evolution of the flow during the pitch cycle over a wide range of reduced frequencies. By altering the timing and strength of the dynamic stall vortex during upstroke motion and characteristics of flow reattachment during downstroke, bleed significantly improves lift hysteresis and pitch stability while maintaining cycle-average forces and moments.

5.1 Aerodynamic Characterization of the Base Airfoil during Pitch Oscillations

The effects of oscillations on the global aerodynamic loads of the base VR-7 airfoil when it is undergoing simple harmonic pitching are first investigated at low angles of attack ($-4° < \alpha < 4°$) and compared with the analysis of Theodorsen (1935) for thin airfoils in simple harmonic motion (no translation) in a uniform, inviscid, incompressible flow (e.g.,

Bisplinghoff Ashley, and Halfman, 1996, and Leishman, 2006):

$$L = \pi\rho U_\infty^2 \frac{c^2}{4}\left[\frac{1}{U_\infty}\dot{\alpha} - \frac{c}{2U_\infty^2}a\ddot{\alpha}\right] + 2\pi\rho U_\infty^2 \frac{c}{2}\left[\alpha + \frac{c\dot{\alpha}}{2V}\left(\frac{1}{2} - a\right)\right]C(k) \tag{5.1}$$

$$M = -\pi\rho\frac{c^3}{8}\left[\left(\frac{1}{2} - a\right)U_\infty\dot{\alpha} + \frac{c}{2}\left(\frac{1}{8} + a^2\right)\ddot{\alpha}\right]$$

$$+2\pi\rho U_\infty \frac{c^2}{4}\left(\frac{1}{2} + a\right)\left[U_\infty\alpha + \frac{c}{2}\left(\frac{1}{2} - a\right)\dot{\alpha}\right]C(k) \tag{5.2}$$

where ω is the angular frequency, U_∞ is the free stream velocity, c is the chord, α and $\dot{\alpha}$ are the pitch angle and angular velocity, and a measures the location of the pitch axis relative to the midchord. $C(k)$ is Theodorsen's function ($k = \omega c/2U_\infty$), defined in terms of in terms of Hankel functions or Bessel functions of the first and second kind:

$$C(k) = F(k) + iG(k) = \frac{H_1^{(2)}(k)}{H_1^{(2)}(k) + iH_0^{(2)}(k)}$$

$$= \frac{J_1(J_1+Y_0)+Y_1(Y_1-J_0)}{(J_1+Y_0)^2+(J_0-Y_1)^2} - i\left[\frac{Y_1Y_0+J_1J_0}{(J_1+Y_0)^2+(J_0-Y_1)^2}\right] \tag{5.3}$$

where J and Y and Bessel functions of the first and second kind, respectively. Theodorsen's function (also known as the lift deficiency factor) represents a ratio of unsteady circulatory lift to quasi-steady circulatory lift. The term *circulatory* signifies that the forces arise from the creation of circulation about the airfoil and therefore implies dependence on the free stream speed. In contrast, *non-circulatory* terms depend on flow acceleration or apparent mass and are important at high reduced oscillation rates. The first bracketed terms in Equations (5.1) and (5.2) are non-circulatory and the second bracketed terms are circulatory. Theordorsen's function for non-static airfoils (Figures 5.1a and b show the real and imaginary parts; the magnitude is smaller than one) scales the circulatory terms of the lift and pitching moment and introduces a phase lag between the motion and the aerodynamic response. In the limit $k \to \infty$, the lift is reduced

to half of the steady-state value, and the phase lag vanishes. In the present investigation, $\alpha = \alpha_A \sin(\omega t)$. Setting $a = -\frac{1}{2}$ in Equations (5.1) and (5.2) to denote pitching about the quarterchord and casting the forces in coefficient form results in:

$$C_L = -\pi k^2 \alpha_A \left[\left(\frac{1}{2} - \frac{2F}{k^2}\right)\cos(\omega t) + \left(\frac{1}{k} + \frac{2F}{k} - \frac{2G}{k} + \frac{2G}{k^2}\right)\sin(\omega t)\right] -$$

$$i\pi k^2 \alpha_A \left[\left(\frac{-1}{k} - \frac{2F}{k} + \frac{2G}{k} - \frac{2G}{k^2}\right)\cos(\omega t) + \left(\frac{1}{2} - \frac{2F}{k^2}\right)\sin(\omega t)\right] \quad (5.4)$$

$$C_M = \pi k^2 \alpha_A \left[\frac{3}{8}\cos(\omega t) + \frac{1}{k}\sin(\omega t)\right]$$

$$+ i\pi k^2 \alpha_A \left[\frac{-1}{k}\cos(\omega t) + \frac{3}{8}\sin(\omega t)\right] \quad (5.5)$$

where F and G are the real and imaginary parts of Theodorsen's function, respectively (cf. Equation 5.3).

The measured variations C_L and C_M ($-4° < \alpha < 4°$) and Theodorsen's theory (Equations 5.4 and 5.5, offset by the cycle-averaged measurements) are shown in Figure 5.2 over a range of reduced frequencies $0.04 < k < 0.34$. These data show good agreement for k up to 0.17, beyond which the theory begins to underpredict the range of measured values with increasing k ostensibly due to the finite thickness and camber of the airfoil and perhaps viscous effects. Although Theodorsen's theory predicts lower lift during the upstroke than during the downstroke (due to the phase lag arising from the circulatory terms), Figures 5.2a-b show that the measured lift values on the upstroke and downstroke are nearly identical for $-1° < \alpha < 4°$ and exhibit some hysteresis for $-5° < \alpha < -1°$. This asymmetry suggests that camber effects may cause the deviation from theory (note that this trend is reversed by $k = 0.17$, as shown in Figure 5.2c). Furthermore, the increasing clockwise rotation of the nominal principal axis of the closed traces between Figures 5.2a to d is owed to the increasing effect of hysteresis which

reduces the amplitude of the circulatory components (namely, F) of the lift in Theodorsen's theory. The pitching moment data in Figures 5.2e-h also show good agreement with the theoretical predictions. Figures 5.2d-h capture both the direction of the induced moment during the cycle and the increase of moment hysteresis with k as a result of acceleration effects. Note that the small-amplitude oscillations in the measured C_M (e.g., near $\alpha = 2°$ on the upstroke in Figure 5.2f) are in part due to the stiff trajectory tracking of the PID controller that seeks to minimize angular position error (cf. §2.4.1.3). The agreement between theoretical predictions and the measurements provides confidence that the capabilities of the pitching facility and force measurement system are sufficient to resolve the variations in C_L and C_M that occur during dynamic stall.

The dynamic loads that arise when the airfoil oscillates in pitch (even at low or quasi-steady rates) result in deviations from the loading at static angles. The aerodynamic performance of the base airfoil is investigated at very low pitch rates to identify the onset of significant deviations from the static loads to delineate the quasi-steady and unsteady pitching regimes. Figures 5.3a-c show phase-averaged measurements of $C_L(\alpha)$, $C_M(\alpha)$, and $C_D(\alpha)$, respectively, for pitching within the range $0° < \alpha < 20°$ at pitch rates of $0.01 < k < 0.13$ along with the static measurements. Figure 5.3a shows that during the upstroke (denoted with solid lines), the dynamic and static lift are close through $\alpha \approx 10°$, beyond which the lift of the static airfoil plateaus while the pitching airfoil experiences a continued increase in lift due to time lag effects and transient boundary layer improvement effects which maintain the suction (e.g., Ericsson and Reding, 1988). The magnitude of the lift overshoot grows with the rate of pitch as shown in Figure 5.3a where the onset of dynamic stall for $k = 0.01$, 0.02, 0.04, 0.08, and 0.13, marked by a

steep ascent in lift, occurs at $\alpha = 18.2°$ ($C_L = 1.33$), 18.3° ($C_L = 1.40$), 18.6° ($C_L = 1.50$), 18.8° ($C_L = 1.81$), and 19.5° ($C_L = 2.00$), respectively. A precipitous drop in lift (accompanied by a massive zone of separated flow beginning at the leading edge) follows the dynamic stall peak, and the angle at which lift is restored on the downstroke (i.e., when the flow reattaches to the airfoil surface) falls with increasing pitch rate. The data in Figure 5.3a, in particular the magnitude of lift overshoot and depth of hysteresis, indicate that $k \sim 0.1$ is a reasonable limit for the quasi-steady pitching regime. Figures 5.3b and c show that dynamic stall is accompanied by a sharp nose-down pitching moment and increase in drag (up to 190% and 160% of the maximum static values, respectively). The peak levels of C_M and C_D, as with C_L, migrate to higher α with increasing k; however, due to the growth of the dynamic stall vortex and its advection to the trailing edge (where C_M is most sensitive), the peak magnitude in nose-down C_M lags the peak of C_L. Significant moment hysteresis during downstroke is evident in Figure 5.3b, particularly for $k = 0.08$ and 0.13, where transient nose-up changes in C_M near $\alpha = 12°$ and 10°, respectively, cause the maximum excursions of C_M during the cycle to reach $\Delta C_M = 0.36$ and 0.38.

5.2 Modification of Vorticity Flux during the Pitch Cycle by Bleed Actuation

The investigations in §4 demonstrated that the interaction of time-dependent bleed flow with the outer flow leads to temporal and spatial modulation of vorticity concentrations within the surface vorticity layer. In the present section, these effects are exploited to alter the transport of vorticity layer on the suction surface of the airfoil with specific emphasis on the timing of the formation of the dynamic stall vortex during the upstroke segment of the pitch cycle. The characteristics of flow separation and attachment during

the upstroke and downstroke segments of the pitch cycle have a profound effect on lift hysteresis and pitch stability (e.g., McCroskey, 1982) and can be strongly affected and improved by bleed actuation. In this section, we restrict attention to a detailed discussion of the effects of bleed actuation on pitch dynamics at a characteristic quasi-unsteady pitch frequency ($k = 0.17$). The effects of bleed on pitch stability and lift hysteresis over a several reduced pitch frequencies are discussed in more detail in §5.3.

Distributions of instantaneous frames (from 2,000 fps PIV) of velocity vectors and spanwise vorticity concentrations in the cross stream (x-y) over the airfoil during pitch at $\alpha(t) = 18° + 4°\sin(2U_\infty kt/c)$ in the absence and presence of bleed actuation are shown in Figures 5.4a-f and g-l, respectively. The bleed actuation is applied time-periodically (at $St_{act} = 1.1$) through a single spanwise row of equally-spaced outlet ports between $0.03 < x/c < 0.04$ on the suction surface at a rate of approximately 20 bleed pulses per pitch cycle. In the absence of actuation, at $\alpha = 18.1°$ (Figure 5.4a) the flow is nominally attached through $x/c = 0.55$, and the separating vorticity layer exhibits streamwise segmentation ($0.55 < x/c < 1.0$) over a reversed flow domain (having a characteristic cross stream width of $\Delta y/c = 0.12$) and the roll up of a CW vortex over the trailing edge. The interaction of the bleed ($x/c = 0.15$) with the outer flow at the same pitch angle (Figure 5.4g) leads to an arc-like displacement of the surface vorticity layer with a local segmentation where the base flow separates ($x/c = 0.55$) that is followed by a rollup of a CW vortex (centered at $x/c \approx 0.9$). At $\alpha = 20.1°$ (Figure 5.4b), the base flow exhibits two CW vorticity concentrations (centered at $x/c \approx 0.35$ and 0.65) where the latter (cross stream scale about $0.3c$ and celerity $0.6U_\infty$) evolves from rollup of the segmented vorticity layer in Figure 5.4a. The formation of these vorticity concentrations is

commensurate with accumulation of vorticity over the airfoil and an increase in lift as demonstrated in Figure 5.5a (following), leading to dynamic stall (e.g., McCroskey, 1981). In the presence of bleed (Figure 5.4h), the vorticity concentrations in Figure 5.4g merge and form a single larger-scale CW vortex that is centered at ($x/c \approx 0.82$) and has a somewhat larger cross stream scale (about $0.4c$) and celerity ($0.7U_\infty$) than the CW vortex in the unforced flow. The formation of these CW vortices is accompanied by concentrations of CCW vorticity near the surface that migrate towards the leading edge. Following shedding of the dynamic stall vortex ($\alpha = 22.0°$, Figure 5.4c), the base flow separates at the leading edge, forming a large recirculation domain that extends to the trailing edge of the airfoil and is accompanied by significant widening of the near wake. The receptivity of the separating shear layer to bleed actuation (Figure 5.4i) leads to modulation of its segmentation resulting in the formation of two distinct CW vorticity concentrations the over the airfoil. When the downstroke begins, the base flow remains stalled, although the cross stream extent of the recirculating domain is somewhat diminished (Figure 5.4d). Bleed actuation leads to the rollup of another CW vortex near the leading edge (Figure 5.4j), partial attachment upstream, and clear separation from the larger CW vorticity concentration downstream that continues to be advected towards the trailing edge. As the downstroke proceeds, the attachment induced by the bleed continues to progress towards the trailing edge ($x/c = 0.40$ in Figure 5.4k, and $x/c = 0.70$ in Figure 5.4l) while at the corresponding pitch angles in the base flow the airfoil remains stalled (Figures 5.4e and f), although the cross stream extent of the separated flow diminishes with the changes in the direction of the outer flow. These data indicate that while the effects of the bleed during the upstroke are more subtle, they contribute to

changes in the *timing* of the formation and advection of the vorticity concentrations that are associated with the dynamic stall (and therefore in the aerodynamic loads), while during the downstroke the induced changes in the vorticity flux downstream of the leading edge lead to significantly earlier attachment compared to the base flow.

The variations in the aerodynamic loads $C_L(\alpha)$, $C_M(\alpha)$, and $C_D(\alpha)$ are measured phase-locked to the pitch cycle for the base flow and in the presence of time-periodic bleed ($St_{act} = 1.1$) and are shown in Figures 5.5a-c, respectively (RMS variations are shown for C_L using shaded bands). The angles corresponding to the Figures 5.4a-l are marked on the $C_M(\alpha)$ trace in the presence of bleed. In the absence of actuation, C_L increases and C_M decreases nearly monotonically with α during the upstroke until the onset of the dynamic stall begins near $\alpha = 20°$ (Figures 5.5a-b). This results in a rapid increase in C_L (up to 2.12 at $\alpha = 21.0°$) that is accompanied by an abrupt (nose-up) increase in C_M through $\alpha = 20.2°$ due in part to the traveling low-pressure zone associated with the dynamic stall vortex (McAlister, Carr, and McCroskey, 1978) and followed by a steep decrease in C_M that continues almost through the peak angle of the pitching cycle, $\alpha_{max} = 22°$. As the airfoil becomes fully stalled at α_{max}, C_L decreases rapidly ($\Delta C_L = -0.84$ between $\alpha = 21.5°$ during the upstroke and 21.5° during the downstroke) and then continues to decrease to $C_{L,min} = 0.63$ near $\alpha = 14.7°$, until finally the flow begins to reattach and lift is restored. The onset of the downstroke and shedding of the dynamic stall vorticity concentrations (cf. Figure 5.4c) produces a rapid recovery of C_M, which increases throughout the downstroke segment of the pitch cycle to slightly nose-up (CW) $C_M = 0.03$ at $\alpha = 14.1°$. It is instructive to consider the pitch cycle's pitch stability as measured by the aerodynamic damping coefficient $E_\alpha = -\frac{\int C_M d\alpha}{\pi \bar{\alpha}^2} = 0.05$

($E_\alpha > 0$ indicates suppressive or stable damping, cf. §1.2.1). Even though cycle is slightly stable, the pitch cycle includes an *unstable* CW loop segment ($19.5° < \alpha < 20.6°$) during which the nose-up pitching moment increases with α. The variation of the cycle drag (Figure 5.5c) shows a rapid increase of the lift-induced drag during dynamic stall ($20.0° < \alpha < 21.8°$) followed by a rapid decrease. The drag during the downstroke is higher than the upstroke because of the persistent delay in attachment (cf. Figures 5.4e-f).

As shown in Figures 5.5a and b, the effects of time-periodic bleed ($St_{act} = 1.1$) at this quasi-unsteady pitch frequency are significant. Although there is a reduction in C_L during the upstroke compared to the base flow ($\Delta C_L \approx -0.25$), the rapid increase in C_L during dynamic stall is significantly muted, and the magnitude and rate of the decrease in C_L following the shedding of the dynamic stall vorticity concentrations are significantly lower as well. As noted in connection with Figures 5.4g-l, it appears that these changes in C_L relative to the base flow are associated with the bleed-induced changes in the timing of the formation, advection, and shedding of the CW vorticity concentrations. Furthermore, the earlier flow attachment during the downstroke (cf. Figures 5.4k-l) leads to higher, nearly invariant C_L for $14° < \alpha < 20°$. Therefore, the actuation results in a significant reduction in cycle hysteresis. Despite a reduction in lift during the upstroke, the cycle-averaged lift in the presence of bleed ($\langle C_L \rangle = 1.26$) is only slightly lower (4%) than the lift of the base flow ($\langle C_L \rangle = 1.31$). The corresponding bleed-induced changes in C_M manifested by rapid variations associated with the shedding of the dynamic stall vorticity concentrations (cf. Figure 5.4i) are damped, and the increase in the nose-down rate during the upstroke is smaller than for the base flow. The maximum nose-down moment ($C_M = -0.30$) is lower in magnitude than in the base flow ($C_M = -0.35$) and occurs

earlier during the pitch cycle ($\alpha = 21.0°$ compared to 21.7° for the base flow). Furthermore, the sense of $C_M(\alpha)$ is CCW throughout the *entire* pitch cycle indicating that the cycle is stable (positively damped), and, in fact, E_α = 0.72 which is significantly higher than in the base flow. In the presence of bleed, the drag is somewhat higher than in the base flow during the upstroke, but is lower near the α_{max} ($C_{D,max}$ = 0.68 at $\alpha = 21°$ compared to 0.80 for the base flow). The attached flow in the presence of bleed during the downstroke leads to lower C_D and the cycle-averaged drag is only 3% higher than in the base flow.

The interaction between the time-periodic bleed flow issuing from the suction-side outlet and the local cross flow that leads to variations in vorticity flux near the surface is examined using magnified phase-locked PIV measurements at 20 equally-spaced time increments during the pitch cycle (Figure 5.6). These measurements allow a comparison of the phase-averaged mass flow rate coefficient, $C_Q(t) = \frac{s_{jet} \cdot \int \vec{V}_{jet} \cdot \vec{n}\, dl}{s \cdot c \cdot U_\infty}$ (s_{jet} is the span of the bleed ports) to $C_L(t)$ and $C_M(t)$. Figure 5.6a shows a phase-averaged color raster plot (t/T_{cyc} = 0.45) of the spanwise vorticity in the cross stream *x-y* plane within a domain measuring 0.1*c* x 0.09*c* over the bleed outlet (the leading edge is located at *x/c* = -0.02 in the figure coordinate frame). The black dashed line extending across the bleed outlet ($0.012 < x/c < 0.022$) represents the control surface through which the mass flow rate is estimated by interpolating the measured velocity. In Figure 5.6a, the bleed flow forms a small rectangular jet at the outlet that is characterized by opposite sense shear layers at its upstream and downstream edges (CCW on the left). The jet is skewed in the streamwise direction and leads to the dominant CW vorticity layer that is formed over the leading edge away from the suction surface while the downstream CW domain of vorticity from

the bleed jet merges with the shear layer and contributes to its downstream spreading.

While the control authority demonstrated using time-periodic bleed actuation during pitch cycle is attained with levels of C_Q that do not exceed $O(10^{-4})$, the magnitude of the bleed during pitch is affected by the variations in the pressure distribution over the airfoil. Figure 5.6b shows that although the phase-averaged $C_L(t)$ peaks during the upstroke, the bleed flow rate issuing from the outlet has a minimum as a result of the interaction with the higher-momentum (locally attached) cross flow along the surface. As the lift decreases after the dynamic stall vortex is shed (near $t/T_{cyc} = 0.1$) and the downstroke ($0.25 < t/T_{cyc} < 0.75$) commences, the flow rate of the bleed flow increases. The oscillations in C_Q (about 33 Hz) during $0.75 < t/T_{cyc} < 0.80$ may be related to the periodic segmentation (cf. Figure 5.4k) of the vortex layer downstream of the leading edge and may be the result of the role of the dynamic evolution of the flow over the suction surface in time-periodic regulation of the magnitude of the bleed flow (cf. §4.3). In contrast to Figure 5.6b, Figure 5.6c shows that the bleed flow rate tracks the phase of the pitching moment remarkably well. During the upstroke, low levels of bleed flow are associated with the nose-down moment. The bleed flow rate increases with C_M through $t/T_{cyc} = 0.5$ (opposite to the rotation of the airfoil), and contributes to stable pitch (positive damping) before undergoing the oscillations through $t/T_{cyc} = 0.9$.

As discussed in connection with Figure 5.4, the continuous variations in aerodynamic loads on the base airfoil are manifested by the formation, advection, and shedding of spanwise vorticity concentrations, and therefore by changes in the vorticity flux into the wake, both of which are significantly affected by bleed actuation. Of particular interest are the transitory accumulation and shedding of vorticity concentrations during dynamic

stall. These effects are evaluated using phase-locked PIV measurements over the domain $0 < x/c < 0.57$ and $0 < y/c < 0.92$ in the near wake (beginning $x/c = 0.05$ downstream of the trailing edge). Figure 5.7 shows distributions of velocity vectors and spanwise vorticity concentrations in the absence (Figures 5.7a-e) and presence (Figures 5.7f-j) of bleed at $t/T_{cyc} = 0$, 0.10, 0.20, 0.70, and 0.75 (corresponding respectively to $\alpha = 18.0°$, 20.4°, and 21.8° during upstroke, and $\alpha = 14.2°$ and 14.0° during downstroke). Also shown are the corresponding distributions of the streamwise flux of spanwise vorticity into the wake in the absence (Figures 5.7k-o) and presence (Figures 5.7p-t) of bleed. The trailing edge of the airfoil is moving within $0.11 < y/c < 0.23$ (marked on the ordinate; $y/c = 0.17$ at $\alpha = 18.0°$).

The attached flow over the base airfoil during the upstroke (Figure 5.7a, $\alpha = 18.0°$) results in shedding of concentrated layers of CW and CCW vorticity from the suction and pressure surfaces, respectively, that become diffused by $x/c = 0.20$. The presence of bleed (Figure 5.7f) leads to a significant (nearly three-fold) increase in cross stream spreading of the wake at $x/c = 0$, which is associated with the lift diminution of $\Delta C_L \approx -0.25$ as discussed in connection with the formation of large-scale vortices in the instantaneous images in Figures 5.4a and g. Both in the absence and presence of bleed (Figures 5.7k and p, respectively), outer layers of streamwise flux of CW and CCW vorticity enclose inner layers of flux of alternating sense, namely, upstream flux of CW vorticity and of CCW, that appear to scale with the overall width of the near wake. These upstream, opposite sense flux layers above and below on each side of the wake's centerline contribute to respective increase and decrease in the time rate of change of the circulation about the airfoil.

At the onset of moment stall (cf. Figure 5.5b), the shedding of a CW vortex from the base airfoil (Figure 5.7b) leads to a momentary counterclockwise rotation of the inner layers of wake flux (Figure 5.7l) that marks the onset of a precipitous decrease in C_M. However, in the presence of bleed (Figure 5.7g) the wake exhibits gradual cross stream spreading with corresponding growth in the streamwise and cross stream extents of the inner and outer layers of flux (Figure 5.7q) that appear to mitigate the rate of change of C_M (cf. Figure 5.5b). Dynamic stall of the base airfoil is accompanied by an abrupt transition to fully separated flow in Figure 5.7c, rapid cross stream spreading, and an increase in strength of the inner layer of upstream flux of CW vorticity (Figure 5.7m). In contrast, segmentation of the CW vorticity layer over the airfoil in the presence of bleed (cf. Figure 5.4i) alleviates this abrupt transition in the base flow and results a predominately counterclockwise traversal of the C_M trace during the cycle (i.e., improved stability). The bleed-induced changes are manifested by earlier occurrence of the moment stall ($\alpha = 18.8°$ compared to 20.0° in the absence of bleed, cf. Figure 5.5b), a reduction in $dC_M/d\alpha$ (to -0.08/° compared to -0.19/° for the base airfoil), and a reduction in $C_{M,min}$ (to -0.30 compared to -0.35 for the base airfoil). Also, in the presence of bleed, the layer of CCW vorticity remains coherent significantly farther downstream indicating that the interaction of the bleed with the cross flow suppresses fluctuations in flux of CCW vorticity and therefore in the aerodynamic loads which may be indicative of the reduction in lift hysteresis and the improved pitch stability. Lift is restored as reattachment progresses through the trailing edge, the remnants of CW vorticity concentrations associated with stall are advected downstream of the base airfoil (Figure 5.7d), and the CCW vorticity layer that is accompanied by an intense band of streamwise

flux ($\Delta x/c > 0.5$) becomes vectored downward (-7.5° relative to the free stream, Figure 5.7n). As with the onset of dynamic stall, the reattachment process in the presence of bleed is marked by the gradual collapse of the CW vorticity domain (Figure 5.7i), and the upstream flux of CW vorticity begins to retract upstream (Figure 5.7s). Finally, the cross stream widths of the wake with and without bleed contract at the bottom of the downstroke segment (Figures 5.7e and o), and though the corresponding magnitudes of C_L are momentarily similar at 1.1 (cf. Figure 5.5a), the base airfoil regains lift at a significantly faster rate ($dC_L/d\alpha \approx 0.96/°$) than in the presence of bleed ($dC_L/d\alpha \approx 0.09/°$).

The effects of the bleed on the spatial and temporal characteristics of the vortical structures during the pitch cycle (and therefore on the aerodynamic loads) are also investigated using proper orthogonal decomposition (POD) of the time-resolved streamwise flux of spanwise vorticity concentrations $\Psi(x, y, t) = u(x, y, t) \cdot \zeta(x, y, t)$ in the near wake of the pitching airfoil. The POD analysis follows the method described in detail in §4.4. The pitch oscillation cycle is analyzed using 2,500 instantaneous images (captured at 2 kHz) from five consecutive pitching cycles. The effectiveness of POD in capturing the contributions of dominant structures of vorticity flux is illustrated in Figure 5.8 by reconstructing a characteristic *instantaneous* snapshot of $\Psi(x, y, t)$ within a domain $0.25 < x/c < 0.80$, $0 < y/c < 1.40$, beginning $0.25c$ downstream from the trailing edge. These data are captured at $\alpha = 21.8°$ ($t/T_{cyc} = 0.20$) during upstroke (the position of the trailing edge is marked for reference) just as the dynamic stall vortex is beginning to advect over the trailing edge of the base airfoil as is evident by the streamwise flux of concentrations of CW vorticity in $y > 0.5c$ at the left side of the image (Figures 5.8a-e). The corresponding image in the presence of time-periodic bleed ($St_{act} = 1.1$) is shown in

Figures 5.8f-j. The snapshot of vorticity flux in the wake is reconstructed in incremental steps of the total energy in the base flow and in the presence of bleed: 25% (using 6 and 8 modes Figures 5.8b and g), 50% (31 and 33 modes in Figures 5.8c and h), 75% (104 and 106 modes in Figures 5.8d and i), and finally 100% (2,500 modes in Figures 5.8e and j). While 25% of the energy in the flux of the base flow (Figure 5.8b) captures the streamwise flux associated with the shedding of CCW vorticity from the airfoil's pressure side, the concentrations of streamwise flux of CW vorticity in the original snapshot are only weakly evident throughout the pitching cycle, indicating that the dynamic stall vortex is dominated by the presence of small-scale motions. In contrast, in the presence of bleed, 25% of the energy reveals a strong band (about 0.4*c* wide) of streamwise flux of CW vorticity. This indicates that the presence of the bleed regulates the shedding of CW vorticity throughout the pitch cycle. With the addition of lower-energy modes (Figures 5.8c-d for the base airfoil and Figures 5.8h-i with bleed), more details of the streamwise flux of CW vorticity are revealed. Although the finest details of the structures do not appear until the energy from nearly all of the modes is accounted for (Figures 5.8e and j in the absence and presence of bleed, respectively), a close representation of the vorticity flux during dynamic stall can be achieved using the first 20 highest-energy modes.

Figure 5.9 shows color raster plots of the three most energetic POD modes of the flux during the entire pitch cycle in the near wake of the base pitching airfoil (Figures 5.9a, c, and e, 17.6% of the energy) and in the presence of bleed (Figures 5.9b, d, and f, 14.9% of the energy). The first mode of the base flow (Figure 5.9a, 9.6% of the energy) exhibits streamwise fluxes of opposite sense that are associated with the CW vorticity of the separating shear layer (centered about $y/c = 0.95$) and the CCW vorticity layers over the

suction and pressure surfaces (centered about $y/c = 0.50$). Bleed actuation alters the first flux mode significantly (Figure 5.9b, 7.3% of the energy). The magnitude of the streamwise flux of CW vorticity is diminished, and two inner flux layers of opposite sense appear between the top and bottom streamwise flux layers (cf. Figure 5.7p). The inner layers represent upstream flux of CW (top) and CCW (bottom) vorticity as part of a continuous regulation of vorticity concentrations in the near wake (as shown in Figure 5.7r, this regulation intensifies when the flow is separated). The second POD modes appear to capture primarily the flux of opposite-sense vorticity of the attached flow (cf. Figures 5.7o and t). While the second mode of the base flow (Figure 5.9c, 5.0% of the energy) is nearly streamwise-continuous, the bleed leads to spatial segmentation of the fluxes of CCW and CW vorticity (Figure 5.9d, 3.9% of the energy), that are probably related to the segmentation of the vorticity layer discussed in connection with Figure 5.4l, indicating temporal modulation of vorticity flux during the pitch cycle that affects the global circulation about the airfoil. The third mode of the base flow (Figure 5.9e, 3.1% of the energy) and in the presence of bleed (Figure 5.9f, 3.6% of the energy) exhibit higher order segmentation of streamwise fluxes of alternating sense (of CW and CCW vorticity concentrations) that are indicative of regulation of the global flux and therefore of the circulation during the pitch cycle. It is noted that the first three POD modes of the velocity distributions (not shown) contain large fractions of the total energy (65% and 51% of the total energy in the absence and presence of bleed, respectively) and primarily indicate the extent of separation in the wake, while the first three modes of vorticity (19% and 17% of the total energy, respectively) and vorticity flux (nearly 18% and 15%, respectively) are similar and show more details of bleed's effects in the near-wake.

It is instructive to consider the time coefficients of the vorticity flux POD modes during the pitch cycles that are shown in terms of the pitch angle in Figures 5.10a-f. The time coefficient of the first mode of the base flow (c_1, Figure 5.10a) indicates, surprisingly, that the first mode is nearly temporally-invariant during the upstroke (even though the lift is increasing). The time coefficient exhibits sharp transitions at α_{max} and α_{min} and some fluctuations, and there is a slow decrease during the downstroke that is probably associated with the attachment of the flow and the decrease in angle of attack. However, in the presence of bleed, c_1 (Figure 5.10b) exhibits a nearly linear increase punctuated by oscillations that are associated with the segmentation of the vorticity layer. The fact that these fluctuations are *not* at the actuation frequency indicates that the time scale of the segmentation is also affected by the coupled dynamics of the pitch motion of the airfoil. The decrease during the downstroke has a similar pattern, and there is some hysteresis. The time coefficient of the *second* mode of the base flow (c_2, Figure 5.10c) is somewhat reminiscent of c_1 in the presence of bleed, although the traces that correspond to the upstroke and downstroke motions intersect at $\alpha = 18°$ (which is just following the commencement of separation near the trailing edge). The time coefficient c_2 with bleed (Figure 5.10d) is remarkably similar to c_3 for the base flow (Figure 5.10e) and to c_3 with bleed (Figure 5.10f) and indicate alternating regulation of the vorticity flux and therefore of the circulation.

These findings indicate that the bleed predominantly modulates the spatial and temporal distributions of vorticity flux over the airfoil and into the near wake to effect changes in the global circulation and therefore in the aerodynamic forces and moments. As will be discussed in §5.3, these variations in the flow field can be harnessed to

mitigate the adverse effects of the dynamic stall vortex and significantly improve the pitch stability over a range of pitch rates.

5.3 Effects of Bleed Actuation on Pitch Stability

As discussed in §5.2, the effects of bleed actuation on flow over the airfoil during the pitch cycle leads to reduction in lift hysteresis with minimal or no reduction in the cycle-averaged lift and to improved pitch stability (or damping). Figures 5.11a-c show the variations in phase-averaged aerodynamic loads $C_L(\alpha)$, $C_M(\alpha)$, and $C_D(\alpha)$ for the base flow and in the presence of time-periodic bleed ($St_{act} = 1.1$) during the pitching cycle at (nominally quasi-steady) $k = 0.08$, $k = 0.17$ (also shown in Figure 5.5), and $k = 0.25$.

The base flow exhibits lift hysteresis even at quasi-steady pitch oscillation, and it increases with reduced frequency. At $k = 0.08$ (Figure 5.11a), the buildup of the dynamic stall vortex apparently results in nearly invariant lift ($14.5° < \alpha < 19.5°$) that is followed by an abrupt increase ($C_{L,max} = 1.90$ at $\alpha = 20.5°$), stall through $\alpha = 14.9°$ on the downstroke ($C_{L,min} = 0.78$), and reattachment before the downstroke is completed. The increase in lift is also accompanied by a momentary increase in the lift-induced drag ($C_{D,max} = 0.74$, $\alpha = 20.9°$), and the drag during the downstroke (when the flow is stalled) is slightly higher than during the upstroke. The base airfoil undergoes moment stall at $\alpha = 19.4°$ on the upstroke when the dynamic stall vortex begins its streamwise advection and the shift in the center of pressure leads to a nose-down moment and negative pitch damping within $19.0° < \alpha < 20.1°$. Note that the negative peak in nose-down moment ($C_{M,max} = -0.33$, $\alpha = 20.8°$) lags $C_{L,max}$ ($\alpha = 20.5°$) slightly because the reduction in pressure that is associated with the formation and advection of the dynamic stall vortex over the suction surface leads to maximum lift as the vortex advects near midchord and

maximum (nose-down) moment as it passes over the trailing edge.

As the cycle oscillation frequency increases, the formation, advection, and shedding of the dynamic stall vortex and flow reattachment are shifted to later phases in the pitching cycle with significant effects on the aerodynamic loads. The cycle lift hysteresis increases as $C_{L,max}$ and $C_{L,min}$ progress through $\alpha = 20.5°$ (1.90), 21.0° (2.12), and 22.0° (2.27) and through $\alpha = 14.9°$ (0.78), 14.2° (0.65), and 13.9° (0.63), respectively (Figures 5.11a, b, and c). The concomitant increase in $dC_L/d\alpha$ during the upstroke indicates that the rate at which vorticity accumulates and the strength of the dynamic stall vortex also increase with k. Figures 5.11a-c also demonstrate that the pitch stability decreases precipitously with increasing k as is evidenced by the increased ranges of clockwise variation with α (i.e., negative damping). In fact, by $k = 0.25$ (Figure 5.11c), the *entire* pitch cycle is unstable.

Bleed actuation leads to several changes in base flow. The advection and shedding of the dynamic stall vortex begins *earlier* in the pitch cycle while the magnitude of maximum induced lift is somewhat diminished (e.g., for $k = 0.08$, $C_{L,max} = 1.67$ at $\alpha = 19.7°$ compared to 1.90 at 20.5° in the base flow), resulting in a less severe moment stall that occurs earlier during the upstroke. In addition, the hysteresis associated with stalled flow during the downstroke is significantly reduced (for $k = 0.08$, $C_{L,min} = 1.10$ at $\alpha = 14.0°$ compared to 0.78 at 14.9° in the base flow). Bleed actuation also suppresses the negative peak in pitch in the base flow and significantly improves the pitch stability with little or no indication of negative damping. Although the effects of the present bleed configuration on the lift diminish somewhat as k increases, the actuation continues to affect the formation and shedding of the dynamic stall vortex, and, in particular, reduces

the momentary increase in lift during its shedding along with some reduction in the hysteresis. However, the effects of the actuation on $C_M(\alpha)$ are more pronounced with increased oscillation frequency. At $k = 0.17$ (Figure 5.11b) and 0.25 (Figure 5.11c), bleed actuation leads to a marked improvement in pitch stability by complete elimination of the domains of negative damping in the base flow ($19.3° < \alpha < 20.7°$, and $14.0° < \alpha < 22.0°$, respectively).

A number of earlier investigations indicated that the reduced pitching frequency has a profound effect on the evolution of dynamic stall (e.g., McCroskey, Carr, and McAlister, 1976, Ericsson and Reding, 1988, Leishman, 1990). These effects are first assessed in the base flow and are illustrated by considering instantaneous cross stream distributions of the spanwise vorticity and velocity vectors over the airfoil during the pitch cycle ($14° < \alpha < 22°$) at $k = 0.08$, 0.17, and 0.25. The changes in the flow are shown in Figure 5.12 for $\alpha = 20.0°$ during the upstroke (Figures 5.12a-c) and 14.5° during the downstroke (Figures 5.12d-f) along with the corresponding effects on the phase-averaged C_M (Figures 5.12g-i). At $k = 0.08$ and $\alpha = 20.0°$ (Figure 5.12a), the quasi-steady flow separates at the leading edge and shows the formation of a large-scale CW vorticity concentration centered near $x/c = 0.70$ and some remnants of CW and CCW concentrations downstream, indicating that the rollup of the dynamic stall vortex is accompanied by shedding of smaller-scale vortices. As shown in Figure 5.12g, at this point during the pitch cycle the rate of change of nose-down C_M ($dC_M/d\alpha \approx -0.25/°$) is highest following moment stall. It is noteworthy that near the end of the downstroke at $\alpha = 14.5°$ (Figure 5.12d) the flow is still partially separated (at $x/c = 0.60$). The distribution of C_M exhibits a small unstable CW domain ($19.0° < \alpha < 19.9°$) and virtually no hysteresis for

$15.5° < \alpha < 19.0°$ until the flow reattaches as the upstroke segment begins ($C_M = 0$), with an overall damping coefficient of $E_\alpha = 0.29$. As the reduced frequency is increased to $k = 0.17$ at $\alpha = 20.0°$ (Figure 5.12b), the vorticity layer develops a small recirculation domain downstream of the leading edge ($0.25 < x/c < 0.40$), and the large-scale CW vortex is slightly smaller than and centered farther upstream ($x/c = 0.65$) than the corresponding vortex at $k = 0.08$. Furthermore, the flow downstream of this vortex within the streamwise domain $x/c > 0.88$ is deflected towards the surface of the airfoil. At this reduced frequency, the vortex is somewhat delayed relative to the slower pitch cycle (Figure 5.12a) as is evidenced by the position relative to the transient peak in C_M (Figure 5.12h) before the sharp nose-down moment that accompanies the shedding of the dynamic stall vortex. During downstroke, the flow attaches only through $x/c = 0.32$ (Figure 5.12e, $C_M = -0.02$). The trace of $C_M(\alpha)$ exhibits pitch instabilities for $19.6° < \alpha < 20.7°$, and the overall damping coefficient decreases to $E_\alpha = 0.05$. Finally, when $k = 0.25$ at $\alpha = 20.0°$ (Figure 5.12c), the surface vorticity layer becomes curved and is deflected towards the surface at $x/c = 0.55$ and spreads in the cross stream direction with some evidence of reversed flow near the trailing edge. The formation of the dynamic stall vortex is clearly delayed, although the curved vorticity layer appears to be a precursor to its rollup. The delayed formation of the dynamic stall vortex also delays further flow attachment, and at the end of the down stroke, the flow is separated nearly up to the leading edge. The phase-averaged C_M (Figure 5.12i) shows that at this reduced frequency moment stall does not occur until $\alpha = 21.4°$. Perhaps the most salient feature of Figure 5.12i is that the sense of the phase-averaged C_M during the pitch cycle is entirely CW, indicating a degradation of the pitch stability, and the cycle damping

coefficient decreases to E_α = -0.61.

The presence of bleed actuation (St_{act} = 1.1) leads to some profound changes in the base flow as shown in Figures 5.13a-i. At k = 0.08 and α = 20.0° (Figure 5.13a), the actuation leads to a local deflection of the separating vorticity layer towards the surface (x/c < 0.42) that is ostensibly induced by the layer of CCW vorticity that is lifted off the surface by the rollup of a large CW vortical structure advecting towards the trailing edge of the airfoil. The temporal variations in the surface pressure distribution associated with the regulation of the vorticity flux by the bleed lead to significant reduction in the rate and magnitude of the nose-down C_M associated with moment stall ($dC_M/d\alpha \approx$ -0.1/° compared to -0.25/° in the absence of bleed), which is also accompanied by a decrease in the magnitude and CCW hysteresis of the nose-down C_M and by improved pitch stability. This sense changes to CW at α = 15.2° on the downstroke in response to the partially separated flow just ahead of the upstroke segment of the cycle as shown in Figure 5.13d, with an overall damping coefficient of E_α = 0.39. As the reduced frequency is increased to k = 0.17, at α = 20.0° (Figure 5.13b) the flow in the presence of bleed appears to be very similar to the base flow, except that the induced vorticity concentration occurs somewhat earlier in the pitch cycle. However, unlike the base flow, at the end of the downstroke (Figure 5.13e), the flow in the presence of bleed is nearly fully attached. These changes in the evolution of the vorticity distributions lead to further mitigation of moment stall and to a phase-averaged $C_M(\alpha)$ (Figure 5.13h) that is nearly completely CCW, in contrast to the corresponding curve for the base flow. As a result, the damping coefficient in the presence of bleed is E_α = 0.72 (compared to 0.05 for the base flow). When k = 0.25 at α = 20.0° (Figure 5.13c), the distribution of the spanwise vorticity

shows further evidence of segmentation and thereby regulation of the accumulation and advection of vorticity concentrations that also helps attachment earlier in the downstroke (Figure 5.13f). Even though there is a steep increase in the magnitude of the nose-down C_M associated with moment stall (Figure 5.13i), it is still considerably milder than the change of C_M in the base flow, and entire CCW phase curve is stable resulting in a damping coefficient of $E_\alpha = 0.60$. These data indicate that it might be possible to improve this performance by further adjustment of the timing of bleed actuation relative to the pitch cycle.

The shift in the timing of vorticity production and shedding in the presence of bleed is manifested by a reduction in the angle at which moment stall occurs. Figure 5.14 shows the variations of α_{ms}, the angle at which the C_M begins to decrease sharply as a result of the advection of the dynamic stall vortex, with reduced frequency for the base airfoil and in the presence of time-periodic bleed. As shown by McCroskey (1982) and by Ericsson and Reding (1988), the increase in leading edge acceleration with k prolongs the attachment of the suction-side vorticity layer and delays of the formation of the dynamic stall vortex. Consequently, the base airfoil exhibits a gradual increase in α_{ms} with k, and by $k \approx 0.3$, moment stall occurs as the airfoil reaches the apex of the cycle. Beyond this pitch rate, moment stall occurs during the downstroke, which results in a reduction in pitch stability and severe level of negative damping (cf. Figure 5.19b below) as the shedding of the dynamic stall vortex and the downward acceleration of the airfoil's surface produce a rapid decrease in the pitching moment. By shifting the timing of the formation of the dynamic stall vortex to an earlier instant in the cycle and segmenting the surface vorticity layer, the airfoil in the presence of time-periodic bleed experiences

moment stall earlier in the cycle relative to the base flow for $k < 0.42$. These data indicate that a different bleed configuration may be able to perform better at higher k.

As noted in connection with Figure 5.7, time-periodic bleed regulates the production, accumulation, and shedding of vorticity concentrations into the wake. It is instructive to consider the effects of bleed on the vorticity flux into the wake and therefore on the time-dependent circulation over the airfoil that in turns affects the aerodynamic loads. Figure 5.15 shows color raster plots of cross stream distributions of spanwise vorticity flux $u(x,y,t)\cdot\zeta(x,y,t)$ into the near wake (measured $0.3c$ downstream from the trailing edge using phase-locked PIV) in the absence (Figures 5.15a-c) and presence (Figures 5.15d-f) of time-periodic bleed actuation. These data are acquired at 20 equally-spaced phase increments during the pitch cycle for $0.08 < k < 0.34$, beginning at $\alpha = 18.0°$ during the upstroke (the excursion of the trailing edge is marked for reference). Figure 5.15a (quasi-steady pitch rate, $k = 0.08$) shows that when the base flow, is nominally attached ($t/T_{cyc} = 0$, $\alpha = 18.0°$, cf. Figure 5.7a), the opposite sense streamwise fluxes of CW and CCW vorticity concentrations (from the suction and pressure surfaces, respectively) are concentrated within a relatively narrow cross stream domain about the trailing edge ($0.10 < y/c < 0.30$). As the vorticity layer near the leading edge begins to deflect from the surface, a CW vorticity concentration that is a precursor to the dynamic stall (e.g., McAlister and Carr, 1979) is shed at $t/T_{cyc} = 0.05$ and is marked by a near-discontinuity in the CCW flux and by a concomitant change in the CCW flux that results from adjustment of the circulation about the airfoil. The dynamic stall vortex sheds shortly thereafter, between $0.10 < t/T_{cyc} < 0.15$ (i.e., prior to $\alpha_{max} = 22°$), and its signature is evident in the rapid cross stream displacement of the layer of CW flux that bounds from

above a weaker layer of *upstream* flux of CW vorticity within $0.35 < y/c < 0.45$ (corresponding to the stalled flow). The cross stream center of the band of streamwise CW flux decreases slightly from $y/c = 0.65$ to 0.62 throughout most of the downstroke until $t/T_{cyc} = 0.62$, when flow abruptly reattaches and the CW band of flux returns to its pre-stall cross stream elevation centered near $y/c = 0.25$. Following the shedding of the dynamic stall vortex, the layer of CCW streamwise flux is deflected upward, indicating a reduction in α, and bounds a weak layer of upstream flux of CCW vorticity that is associated with the recirculating flow over the stalled airfoil from below. Narrowing and weakening of the CCW streamwise flux accompany the abrupt attachment and reduction in overall lift at the low end of the pitch cycle.

In the presence of bleed, the sharp discontinuities in the vorticity flux are virtually eliminated, resulting in significant temporal changes in the global circulation. Figure 5.15d shows that at $k = 0.08$, the CW vortex that is a precursor to dynamic stall (Figure 5.15a) is suppressed in the presence of bleed. The abrupt excursion of CW flux in the base wake between the band centered at $y/c = 0.25$ ($t/T_{cyc} = 0.05$) and $y/c = 0.65$ as a result of the shedding of the dynamic stall vortex is significantly smoothed, and its cross stream width is considerably more uniform during the cycle. These changes are also accompanied by smoothing of the steamwise flux of the CCW vorticity and the disappearance of the discrete concentrations that are associated with the shedding of the precursor and the dynamic stall vortices ($t/T_{cyc} = 0.05$ and 0.15 in Figure 5.15a, respectively). Of particular note is a reduction in the time rate of change in the cross stream elevation of the CW flux compared to the base flow, indicating a slower slew rate in aerodynamic loads. The data in Figure 5.15d also show that the cross stream widths of

the opposite sense CW and CCW flux layers are considerably wider in the presence of bleed than in the base flow.

The delay in the onset of dynamic stall in the base flow as the pitch frequency increases, evidenced by the sharp excursion in cross stream extent in CW flux during upstroke, is manifested by a phase delay of the vorticity flux during the pitch cycle. For $k = 0.04$, 0.17, and 0.34, the cross stream change in the steamwise flux of the CW vorticity is visible in the near wake of the base airfoil at $t/T_{cyc} = 0.10$, 0.18, and 0.34 (Figures 5.15a-c, respectively). The shedding of the precursor shear layer vortex also becomes more pronounced with k, particularly in the breakup of the CCW vorticity layer within $0.1 < t/T_{cyc} < 0.21$ at $k = 0.34$ (Figure 5.15c). The duration of stalled flow remains similar (nearly $\Delta t/T_{cyc} = 0.50$) for each pitch rate, although its collapse migrates towards the end of the downstroke segment of the cycle (e.g., $t/T_{cyc} = 0.60$ at $k = 0.04$ and 0.90 at $k = 0.34$). The streamwise CW vorticity flux in the presence of bleed at higher pitch rates (Figures 5.15e and f) is significantly smoother with lower slew rates, and sharp transitions between attachment and separation for the base airfoil are muted [although the cross stream width during stall and reattachment at $k = 0.17$ (Figure 5.15e) and 0.34 (Figure 5.15f) are somewhat narrower than at $k = 0.08$]. Perhaps one of the more important features of the streamwise flux of CW vorticity in Figures 5.15d-f is that the (slower) transition to dynamic stall (marked by the cross stream excursions in flux) leads the stall in the base flow by $\Delta t/T_{cyc} \approx 0.10$, indicating *earlier* stall transition that reduces the sharp peak in C_L and negative peak in C_M (cf. trends in Figures 5.11a-c) and thereby increases pitch stability.

The global effects of the changes in vorticity flux in the presence of bleed on the aerodynamic loads on the pitching airfoil are investigated by evaluating the phase-locked circulation about the airfoil using the PIV measurements in the near wake. The circulation is computed by integration of the phase-locked vorticity flux through $x = 0.3c$ downstream from the trailing edge:

$$\Gamma(t) = -\int_0^t \int_{-\infty}^{\infty} u \cdot \zeta \, dy \, dt \tag{5.6}$$

Figures 5.16a, b, and c show the normalized circulation ($\hat{\Gamma} = \Gamma/U_\infty c + \tilde{\Gamma}_0$, where $\tilde{\Gamma}_0$ is the circulation computed from the cycle-averaged lift) for k = 0.08, 0.17, and 0.34, respectively ($t/T_{cyc} = 0$ corresponds to $\alpha = 18.0°$ during upstroke), along with the corresponding cycle-averaged C_L (shown using dotted lines). When $k = 0.08$ (Figure 5.16a) in the absence of bleed, the peak in C_L precedes the peak in $\hat{\Gamma}$ ($t/T_{cyc} = 0.12$ and 0.15 respectively, ostensibly due to the advection time to the wake) as CW vorticity accumulates and is advected along the surface of the airfoil. The shedding of the vortex into the near wake is accompanied by sharp decreases in C_L and circulation that persist through $t/T_{cyc} = 0.65$, when the flow reattaches and circulation begins to increase again. Time-periodic bleed actuation alters both the phase and magnitude of circulation of the base flow with no discernible peak during dynamic stall and considerably faster recovery during the downstroke. While C_L in the presence of bleed during the upstroke is smaller than that of the base flow ($0.07 < t/T_{cyc} < 0.20$), it exceeds the base flow C_L following the base flow stall and during the upstroke $0.20 < t/T_{cyc} < 0.70$ so that the cycle averaged lift is virtually unchanged. Towards the end of the pitch cycle, the circulation in the presence of bleed becomes nearly invariant ($t/T_{cyc} > 0.55$) until dynamic stall occurs during the upstroke of the following pitch cycle. The phase change in vorticity transport in the

presence of bleed is even more pronounced at $k = 0.17$ (Figure 5.16b), where $\hat{\Gamma}_{max}$ and C_L precede the corresponding peaks in the base flow by $\Delta t/T_{cyc} = 0.1$ and 0.05, respectively. As noted in connection with Figure 5.15, bleed leads to an overall reduction in the *variation* of circulation during the pitch cycle, including the abrupt loss in circulation following the shedding of the dynamic stall vortex ($t/T_{cyc} > 0.1$). During downstroke, the bleed improves circulation and lift recovery ($0.50 < t/T_{cyc} < 0.75$) by promoting an earlier collapse of the stalled wake domain (cf. Figure 5.15e). Although the effects of the actuation on the lift and circulation are somewhat more subtle when the pitch frequency is increased to $k = 0.34$ (Figure 5.16c), there is still a strong effect on the pitching moment and pitch stability (cf. Figure 5.19b below) as is evident from the change in timing of the shedding of the dynamic stall vortex in the presence of bleed.

Despite the changes in the dynamics of the vorticity concentrations over the airfoil and consequently in vorticity flux during the pitch cycle that lead to alteration of the instantaneous (phase-averaged) dynamic loads on the base airfoil (cf. Figure 5.11), variations of the *cycle-averaged* C_L, C_M, and C_D in the absence and presence of bleed actuation are remarkably small. This is demonstrated in Figures 5.17a-c that show the cycle-averaged loads over a wide range of pitch rates ($k < 0.42$, corresponding to $f_{cycle} < 10$ Hz, and $14° < \alpha < 22°$). Bleed produces a slight increment in lift at lower pitch rates [e.g., $\Delta\langle C_L\rangle/\langle C_{L,0}\rangle = 0.04$ at $k = 0.04$] that is accompanied by a small increase in drag [$\Delta\langle C_D\rangle/\langle C_{D,0}\rangle = 0.09$ at $k = 0.04$] relative to base airfoil. As k increases, $\langle C_L\rangle$ becomes virtually identical to the base airfoil, and $\langle C_D\rangle$ begins to increase. Over this range of pitch frequencies, bleed results in an average nose-down moment increment of $\Delta\langle C_M\rangle/\langle C_{M,0}\rangle = -0.17$ between $k = 0.04$ and 0.42.

However, as discussed in connection with Figures 5.13 and 5.15, bleed leads to significant cyclical alterations of the flow over the airfoil and in its near wake during the pitch cycle that affect both the cycle's integral measures of the lift hysteresis and pitch stability. To illustrate these effects, Figure 5.18 compares the phase-averaged lift for the base flow (top row) and in the presence of bleed (bottom row, $St_{act} = 1.1$) during the pitch cycle. For clarity, the range of pitch frequencies is split to $0.04 < k < 0.25$ (Figure 5.18a) and $0.29 < k < 0.42$ (Figure 5.18b). It is noted that corresponding variations in $C_M(\alpha)$ are complex (cf. Figure 5.11) and are analyzed in terms of the integrated pitch stability in Figure 5.19b. Figure 5.18a shows that during dynamic stall on the base airfoil, both $C_{L,max}$ and $\alpha_{CL,max}$ increase with k, as does the rate of change in C_L with α prior to the onset of dynamic stall, which is indicative of accumulation of CCW vorticity. It is noteworthy that these changes in the lift curve are accompanied by a significant increase in lift hysteresis. However, the migration of the dynamic stall towards α_{max} ($k \geq 0.25$) means that the formation of the dynamic stall vortex is incomplete (cf. Figure 5.15c), and the abrupt loss in lift and vortex shedding are triggered by the reversal in the direction of pitch motion. The most salient feature of the lift curves in Figure 5.18b is the strong diminution in hysteresis with increasing k, even though the flow reattaches at the later stages of the downstroke closer to α_{min}. It is remarkable that beginning at $k = 0.29$ (Figure 5.18b), the magnitude of lift at the beginning of the downstroke exceeds that of the upstroke (e.g., $C_L = 2.06$ at $\alpha = 21.8°$ on the upstroke and 2.27 on the downstroke), indicating that dynamic stall occurs *after* α_{max} is reached and that the lift can continue to increase after the downstroke motion commences (e.g., Leishman, 1990).

In the presence of bleed (St_{act} = 1.1), the magnitudes of C_L and $dC_L/d\alpha$ during the upstroke are diminished compared to the base flow (Figures 5.18a-b). As with the base airfoil, $\alpha_{CL,max}$ increases with k in the presence of bleed (Figure 5.18a), although dynamic stall occurs at lower α (e.g., at k = 0.04, $C_{L,max}$ = 1.62 for the bleed at α = 18.1° and 1.79 for the base airfoil at α = 20.0°). Note that for low pitch rate, transient reattachment and the formation of a second stall-like vortex can occur (e.g., near α = 20° at k = 0.04). In the presence of bleed, $C_{L,max}$ is somewhat lower; however, $C_{L,min}$ before reattachment on the downstroke is higher, leading to lower lift hysteresis (cf. Figure 5.19a below). It is also noteworthy that unlike the base flow, the nominal $dC_L/d\alpha$ during the upstroke is nearly invariant with increasing k in the presence of bleed (0.09/° at k = 0.04 to 0.11/° at k = 0.25). The presence of bleed also diminishes the strong reduction in hysteresis that characterizes the base flow at higher pitch rates ($0.29 < k < 0.42$), and C_L remains higher during upstroke than downstroke for $k < 0.42$. The prevention of dynamic stall during the downstroke at high k apparently improves the pitch stability of the airfoil, as discussed in connection with Figure 5.19b.

The effects of bleed actuation on the lift hysteresis and the pitch stability are compared by considering the cycle integral lift hysteresis coefficient $H_\alpha = \frac{\int C_L d\alpha}{\pi \bar{\alpha}^2}$ and damping coefficient (Figures 5.19a-b, respectively). In the base flow, H_α (Figure 5.19a) increases rapidly with k and has a local maximum at k = 0.17 (H_α = 8.10) before decreasing monotonically and even becoming negative for $k > 0.35$, which is indicative of higher lift during downstroke (cf. Figure 5.18b). In the presence of bleed, the hysteresis peak is significantly reduced (H_α = 5.77) and occurs at higher k (0.25) compared to the base flow. The integral pitch stability measure E_α in the absence and

presence of bleed actuation is shown in Figure 5.19b. For this range of pitch angles, the base flow is most stable in the quasi-steady range (E_α = +0.29 at k = 0.08). Stability diminishes with increasing k as moment stall advances to higher angles (cf. Figure 5.14), the sign of E_α changes at k = 0.18, and it has a local minimum E_α = -1.13 at k = 0.34. As alluded to in connection with Figure 5.13, the regulation of vorticity flux using bleed actuation results in significant stability enhancement. Figure 5.19b shows that in the presence of bleed, pitch stability is enhanced with increasing k, with a peak of E_α = +0.72 at k = 0.17 (in the quasi-unsteady regime) and the crossover to negative damping occurring at k = 0.31 (compared to 0.18 in the base flow). It appears that the timing of the formation and advection of the dynamic stall vortex (cf. Figure 5.13) plays a crucial role in the severity of moment stall. In particular, the migration of the formation and shedding of the stall vortex closer to α_{max} and ultimately its transition to the downstroke segment of the pitch cycle of the base flow lead to significant penalty in pitch stability. In contrast, the regulation of the vorticity flux up to and during dynamic stall by bleed actuation significantly improves pitch stability. Of course, although the bleed configuration can be further tuned to optimize these effects, such optimization was beyond the scope of the present investigations. These results indicate that bleed actuation leads to significant improvements in pitch stability and lift hysteresis while maintaining nearly-identical cycle-averaged performance to the base airfoil across a range of pitching frequencies.

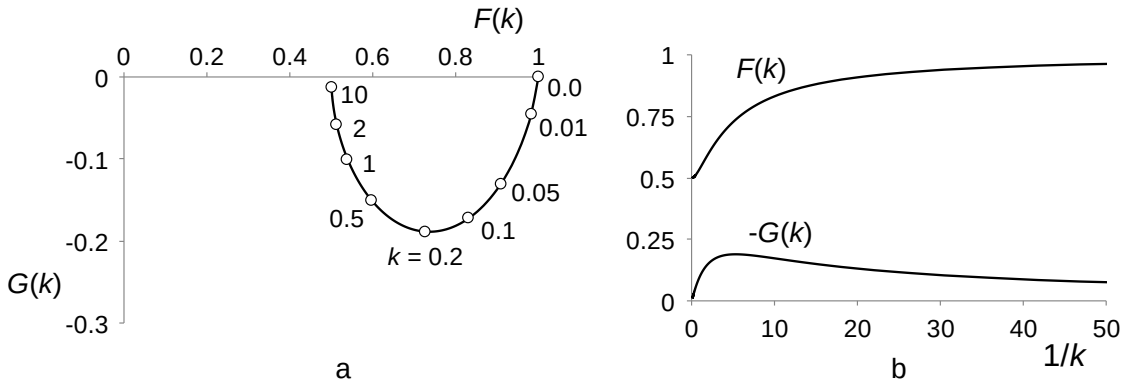

Figure 5.1. Variation in real [$F(k)$] and imaginary [$G(k)$] components of Theodorsen's function $C(k)$ with k (a) and reduced frequency (b).

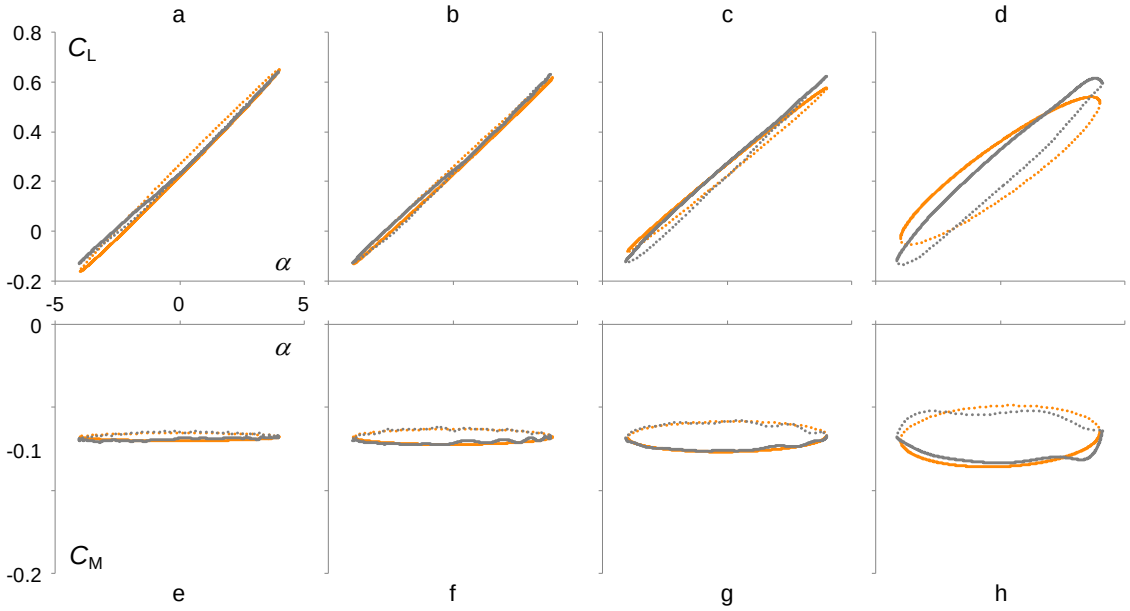

Figure 5.2. Variations in lift (a-d) and pitching moment (e-h) at reduced frequencies k = 0.04 (a, e), 0.08 (b, f), 0.17 (c, g), and 0.34 (d, h) measured for the base airfoil (—) and compared with Theodorsen's predicted loads (—). Upstroke and downstroke motions are shown with solid and dotted lines, respectively.

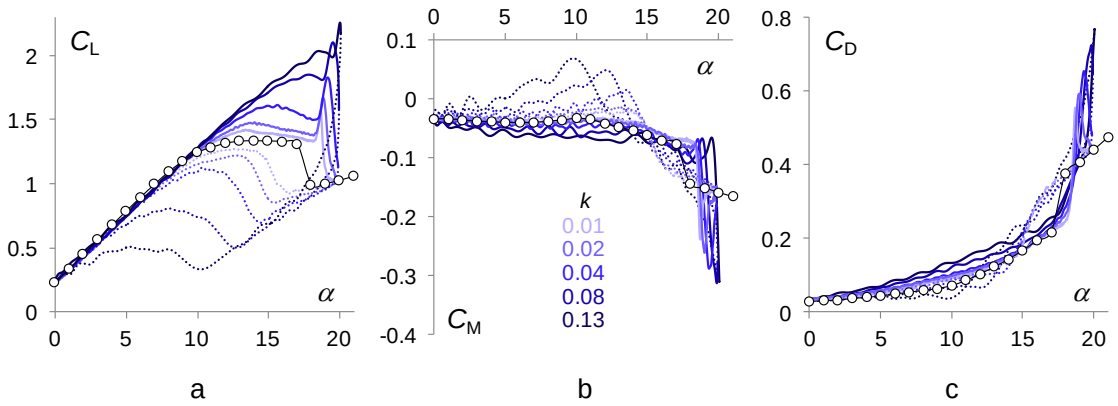

Figure 5.3. Variations of C_L (a), C_M (b), and C_D (c) with α for the base airfoil during pitch oscillations ($0° < \alpha < 20°$) at k = 0.01 (—), 0.02 (—), 0.04 (—), 0.08 (—), and 0.13 (—). Static measurements (○) are shown for reference, and downstroke motion is shown using dotted lines.

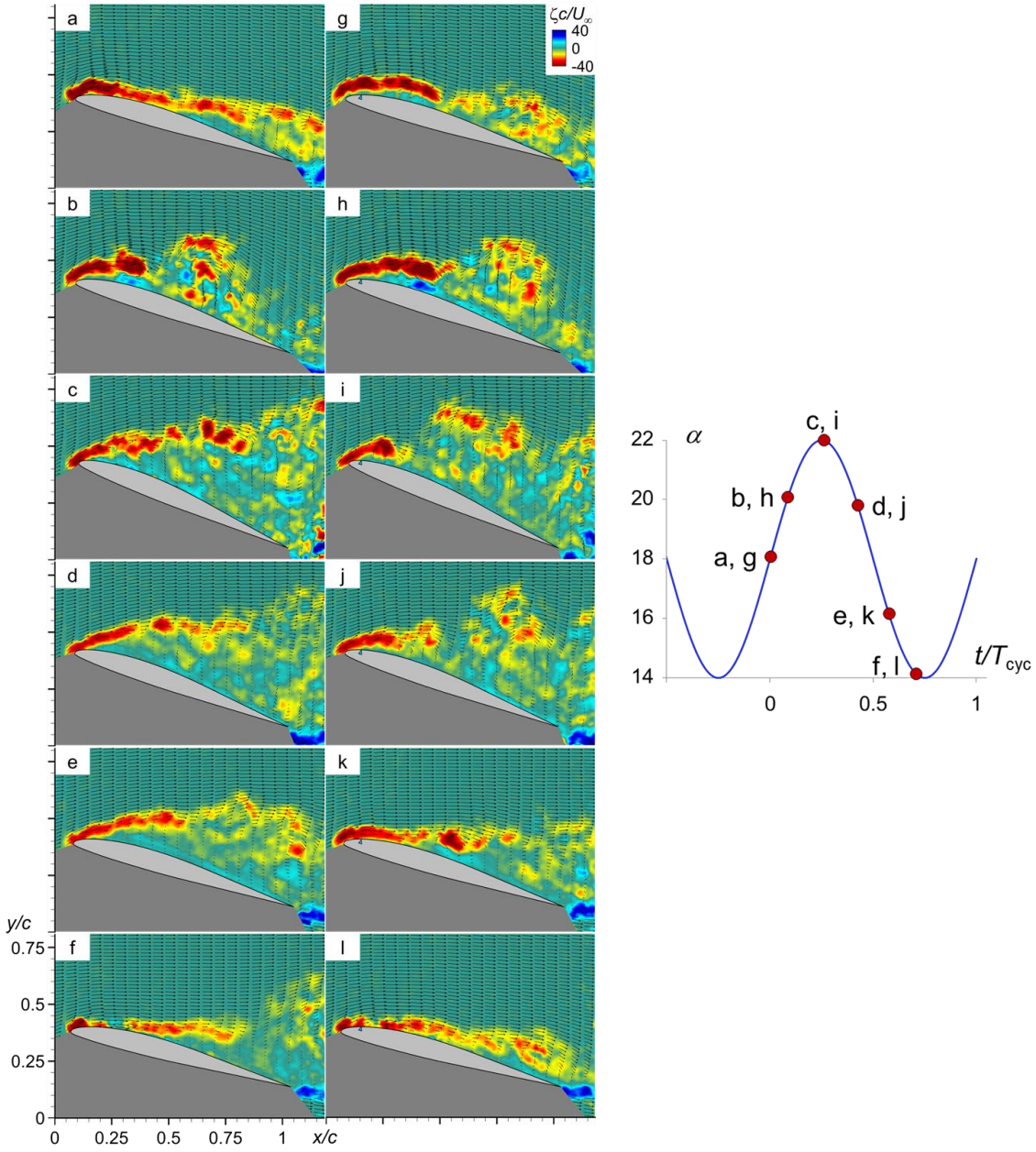

Figure 5.4. Instantaneous flow over the pitching airfoil ($14° < \alpha < 22°$, $k = 0.17$) in the absence (a-f) and presence (g-l) of time-periodic bleed-actuation ($St_{act} = 1.1$). The timing of each frame within the pitch cycle T_{cyc} is shown above: $t/T_{cyc} = 0$ (a, g), 0.09 (b, h), 0.26 (c, i), 0.43 (d, j), 0.58 (e, k), and 0.71 (f, l).

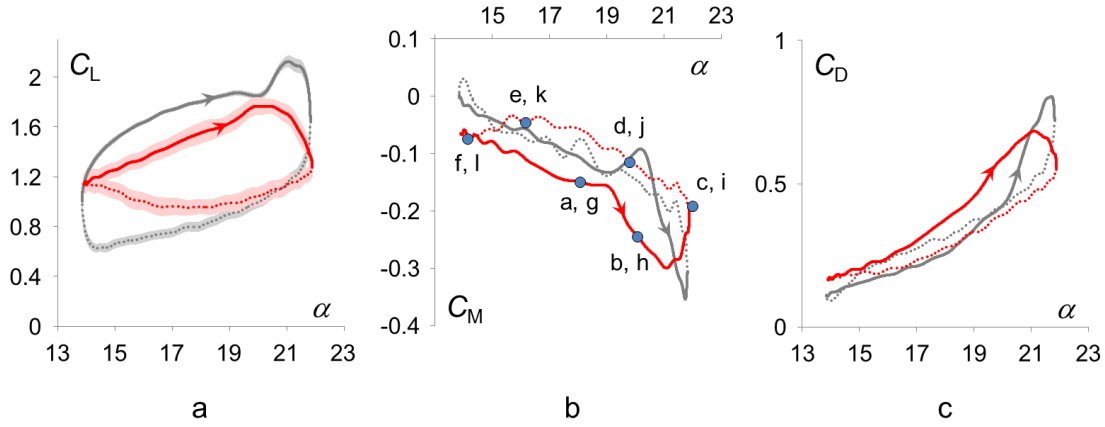

Figure 5.5. Phase-averaged $C_L(\alpha)$ (a), $C_M(\alpha)$ (b), and $C_D(\alpha)$ (c) (k = 0.17) in the absence (—) and presence of bleed (St_{act} = 1.1, —). Upstroke and downstroke motion are indicated by solid and dotted lines, respectively. The RMS variations in C_L are shown in (a) using shaded bands, and angles corresponding to the bleed phases in Figure 5.4 are marked in (b) with circles.

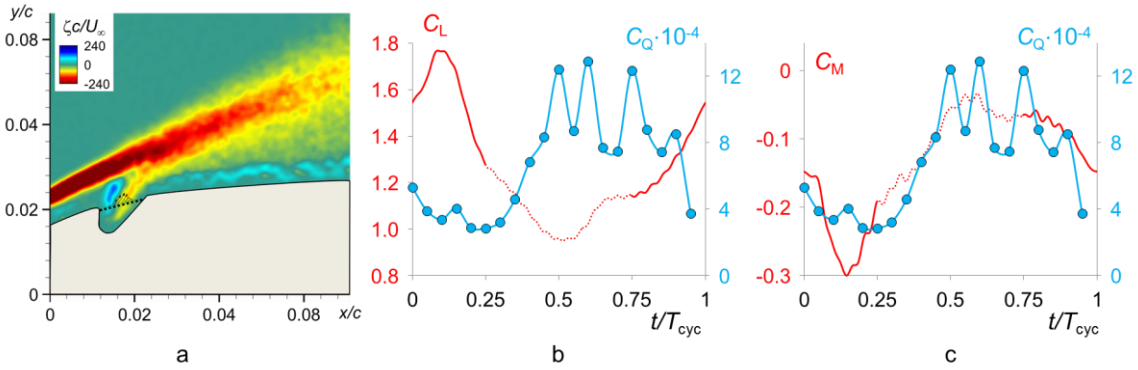

Figure 5.6. Phase-averaged distribution of spanwise vorticity concentrations near the bleed outlet (x/c = 0.03) over the suction surface during pitch oscillations (k = 0.17, t/T_{cyc} = 0.45). The black dashed line spanning the outlet (0.012 < x/c < 0.022) depicts the control surface through which the bleed mass flow rate is calculated. Variations in phase-averaged C_L (—, b) and C_M (—, c) during the pitching cycle are shown alongside C_Q (—). Downstroke motion is indicated with dotted lines.

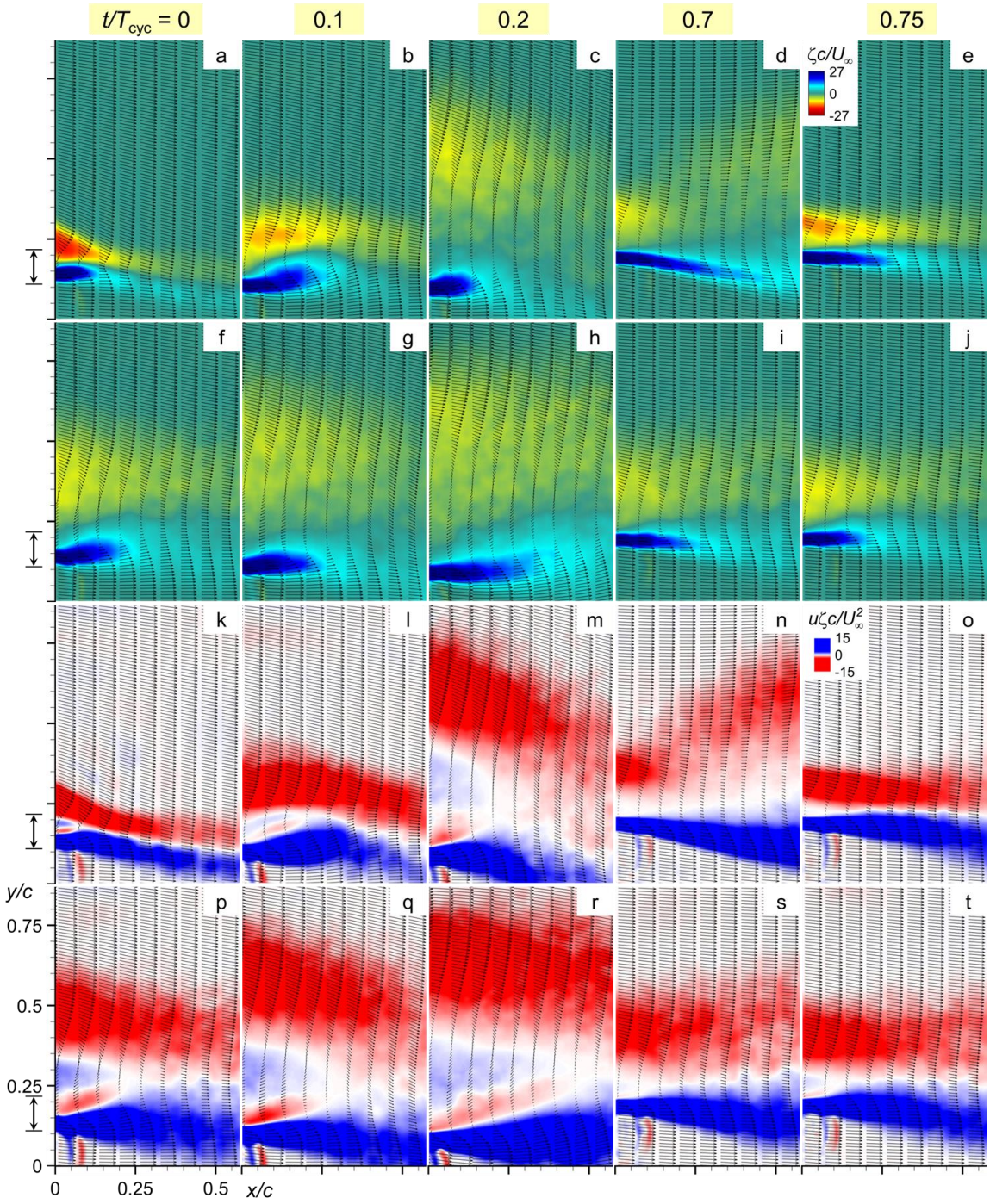

Figure 5.7. Phase-locked distributions of velocity vectors and spanwise vorticity concentrations during pitch oscillations (k = 0.17) of the base airfoil (a-e) and in the presence of bleed (f-j) along with corresponding distributions of vorticity flux for the base airfoil (k-o) and in the presence of bleed (p-t), measured at x/c = 0.05 downstream of the trailing edge. Times for each column are shown above, and the vertical excursion of the trailing edge of the airfoil is shown on the ordinate.

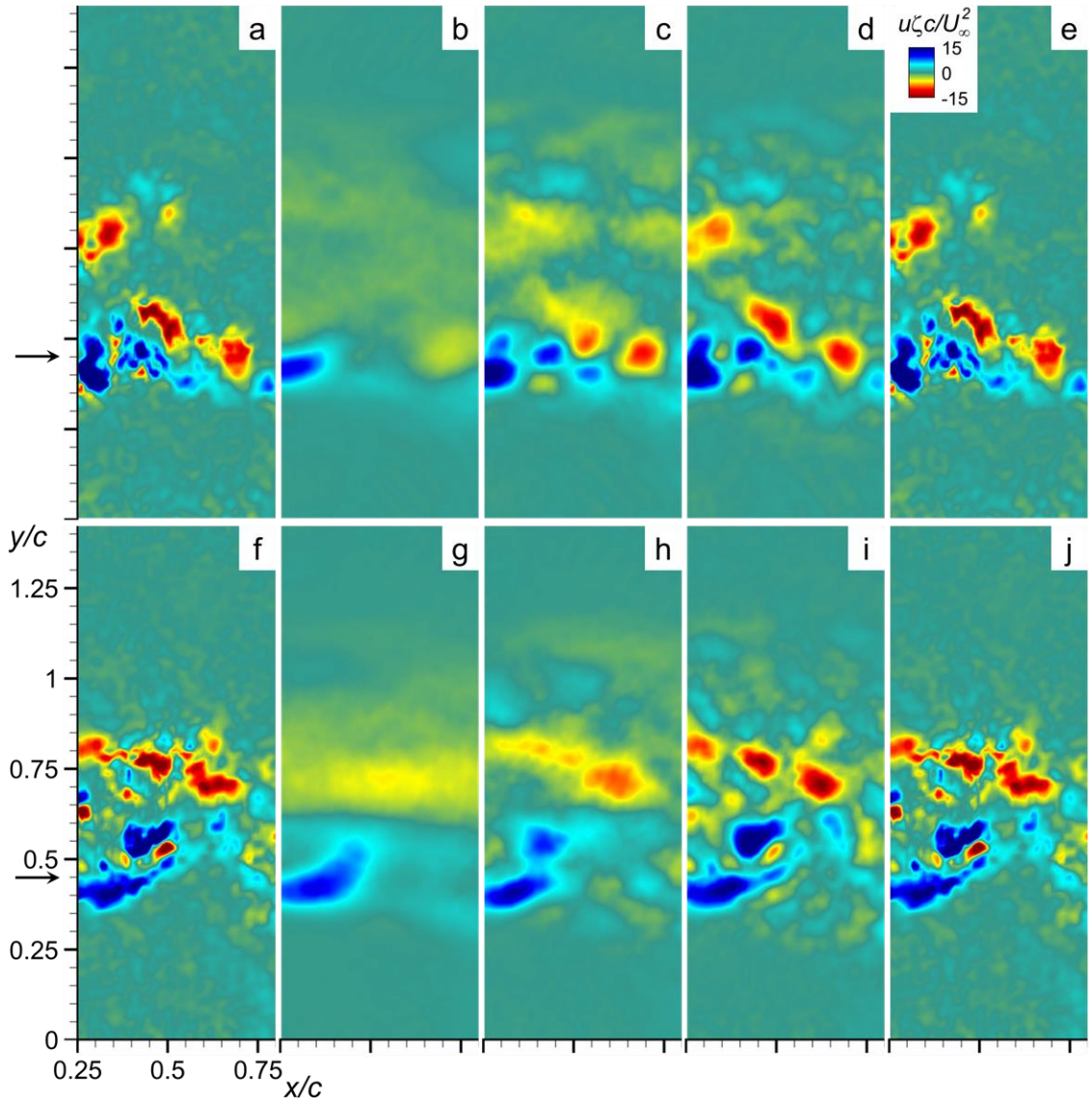

Figure 5.8. POD reconstructions of instantaneous fields of spanwise vorticity flux (t/T_{cyc} = 0.20 and α = 21.8° during upstroke at k = 0.17) over the base airfoil (a-e) and in the presence of bleed (f-j): (a, f) the actual snapshots , and POD reconstructions using 25% of the total energy (6 modes, b; 8 modes, g), 50% (31 modes, c; 33 modes, g), 75% (104 modes, d; 106 modes, i), and 100% (2,500 modes, e and j). The location of the trailing edge of the airfoil 0.25c upstream is marked on the ordinate with an arrow.

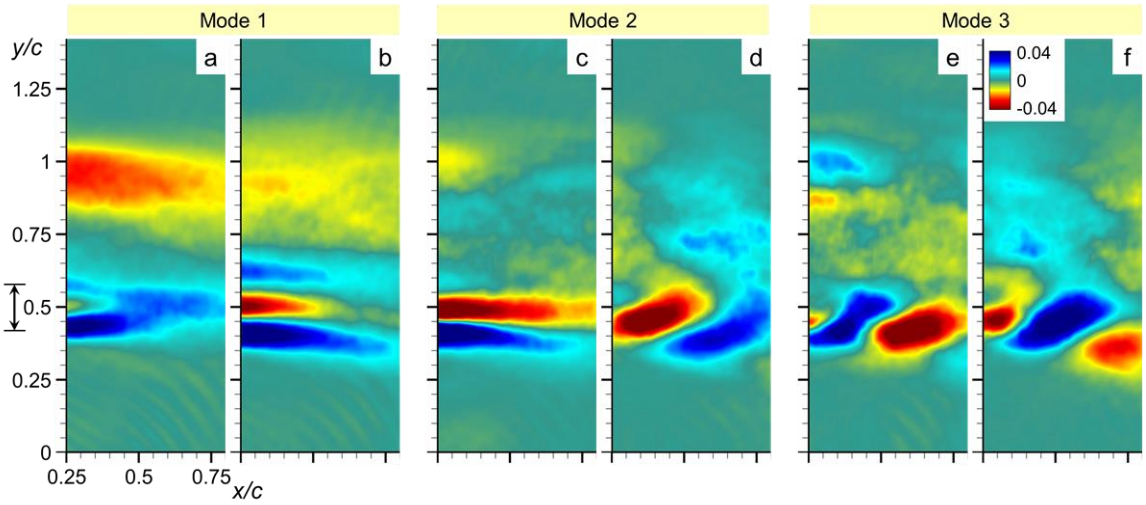

Figure 5.9. Contours of POD modes of spanwise vorticity flux in the near wake during pitch oscillations (k = 0.17, 0.25c downstream of the trailing edge) for the base flow (a, c, and e) and with bleed (St_{act} = 1.1; b, d, and f). The vertical excursion of the trailing edge of the airfoil is shown on the y axis.

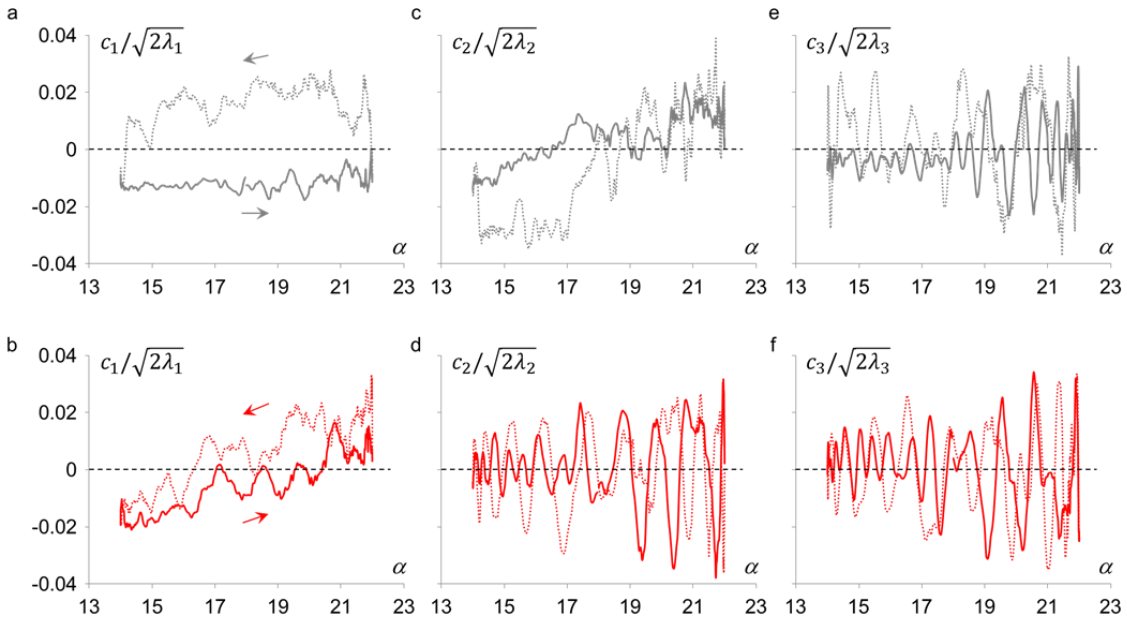

Figure 5.10. Normalized POD time coefficients of the flux of spanwise vorticity during the pitch cycle corresponding to the POD modes in Figure 5.9 for the base flow (—) and in the presence of bleed (—). Solid and dotted curves show upstroke and downstroke motions, respectively.

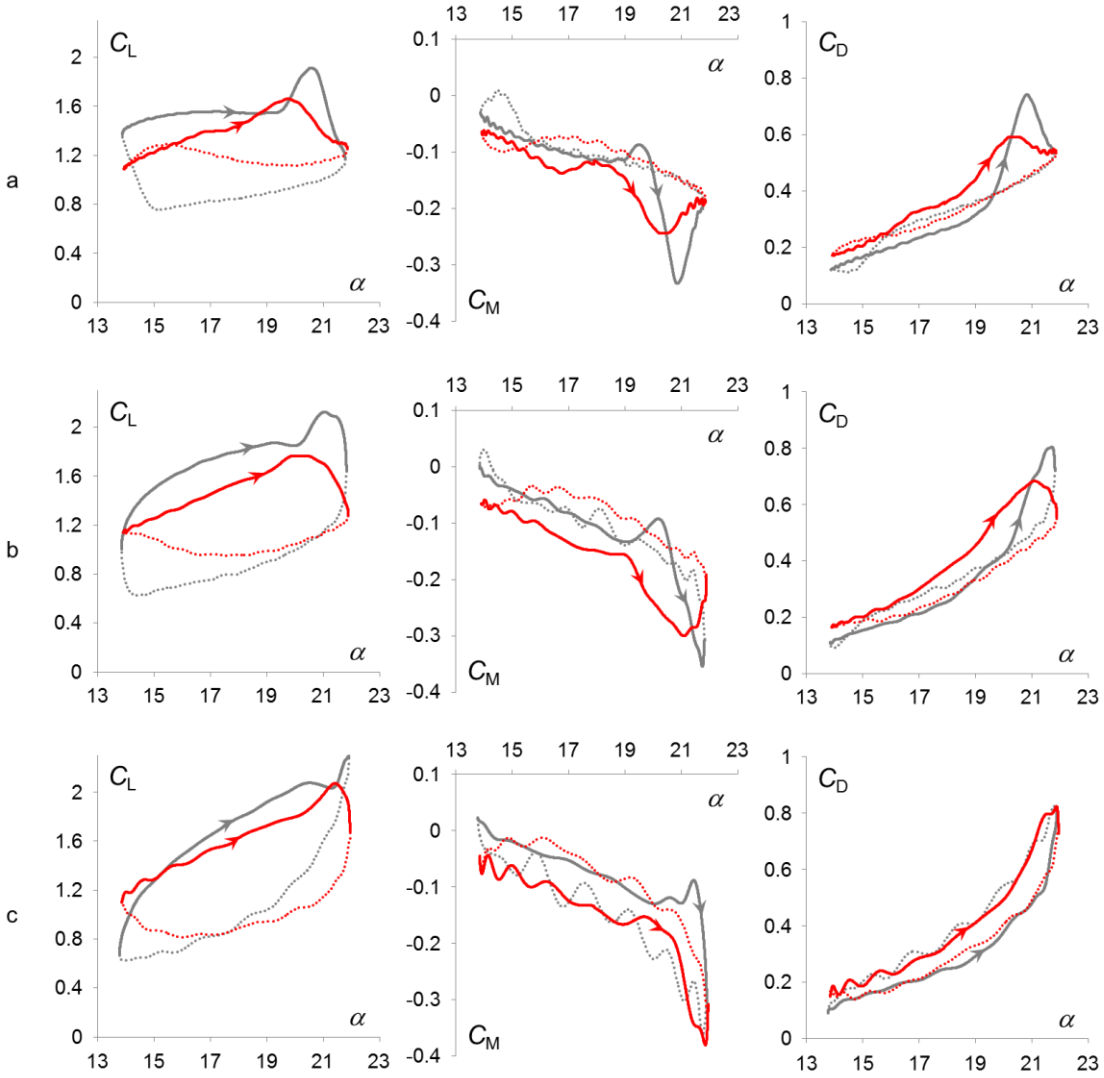

Figure 5.11. Variation of $C_L(\alpha)$, $C_M(\alpha)$, and $C_D(\alpha)$ for the base airfoil (—) and in the presence of time periodic bleed (St_{act} = 1.1, —) during a pitching cycle at k = 0.08 (row a), 0.17 (b), and 0.25 (c) for 14° < α < 22°. The bleed configuration uses one spanwise row located at 0.03 < x/c < 0.04. The downstroke motion is shown using dotted lines.

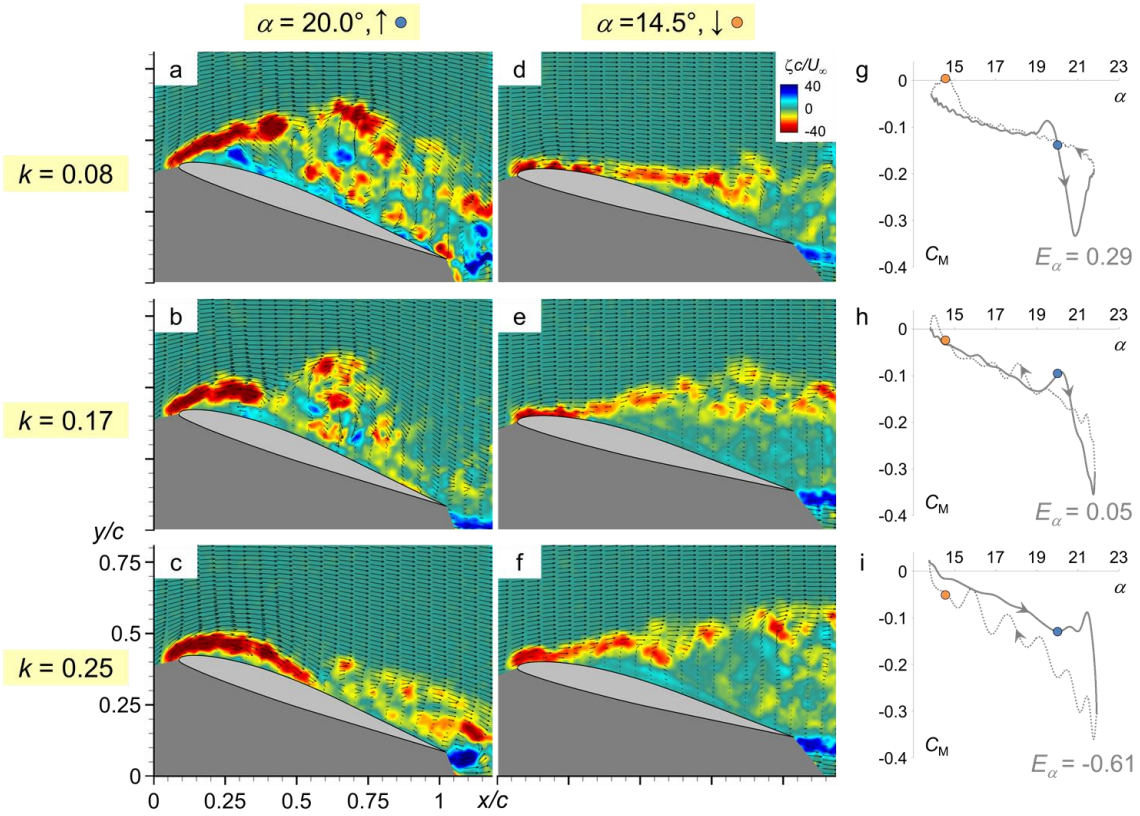

Figure 5.12. Instantaneous distributions of velocity and spanwise vorticity for the base airfoil during time-periodic pitch ($14° < \alpha < 22°$). Upstroke through $\alpha = 20.0°$ and down stroke through $\alpha = 14.5°$, respectively, are shown for $k = 0.08$ (a, d), $k = 0.17$ (b, e), and $k = 0.25$ (c, f). The corresponding phase-averaged C_M during the cycle is shown in g-i using solid lines for upstroke and dotted for downstroke; $\alpha = 20.0°$ and 14.5° are marked with blue (upstroke) and orange (downstroke) circles, and the damping coefficients are noted.

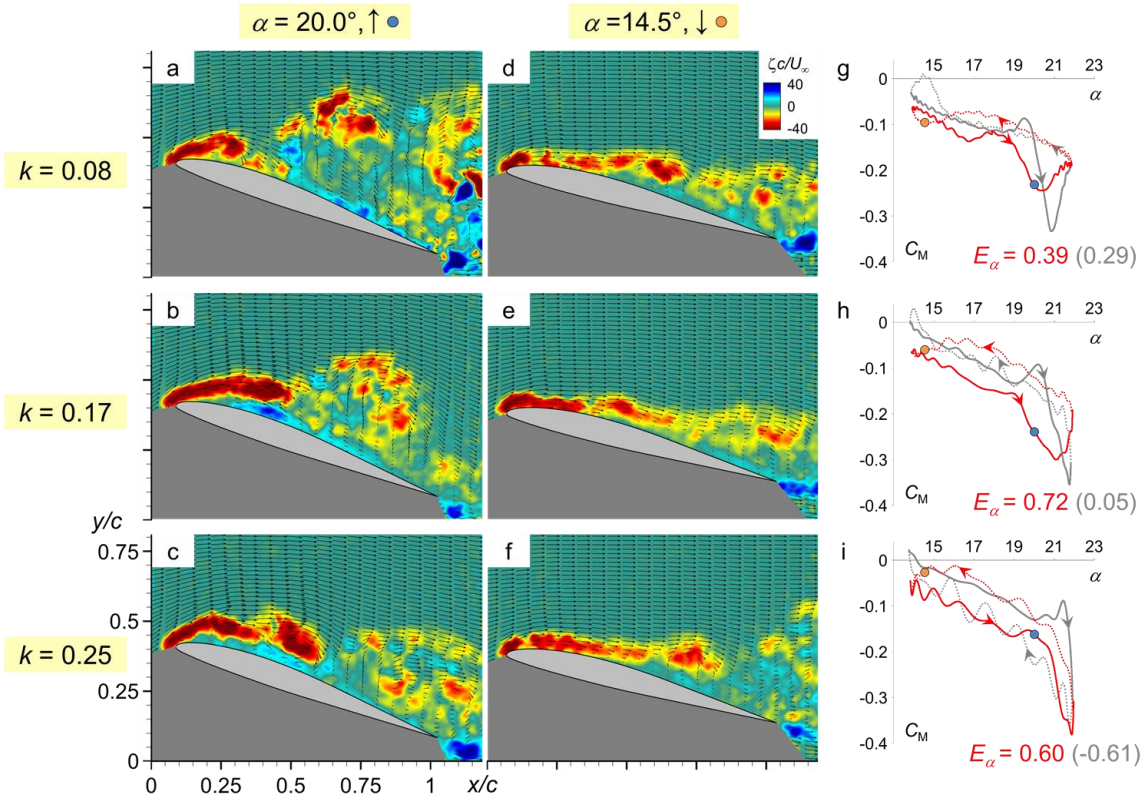

Figure 5.13. As in Figure 5.12 (—) but in the presence of bleed (St_{act} = 1.1, —).

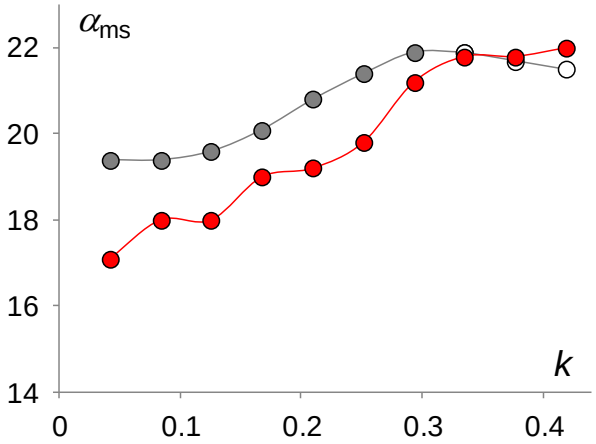

Figure 5.14. Variations in the angle at which moment stall occurs with reduced frequency during pitching from 14° < α < 22° for the base airfoil (● upstroke and ○ downstroke) and with bleed (St_{act} = 1.1, ●).

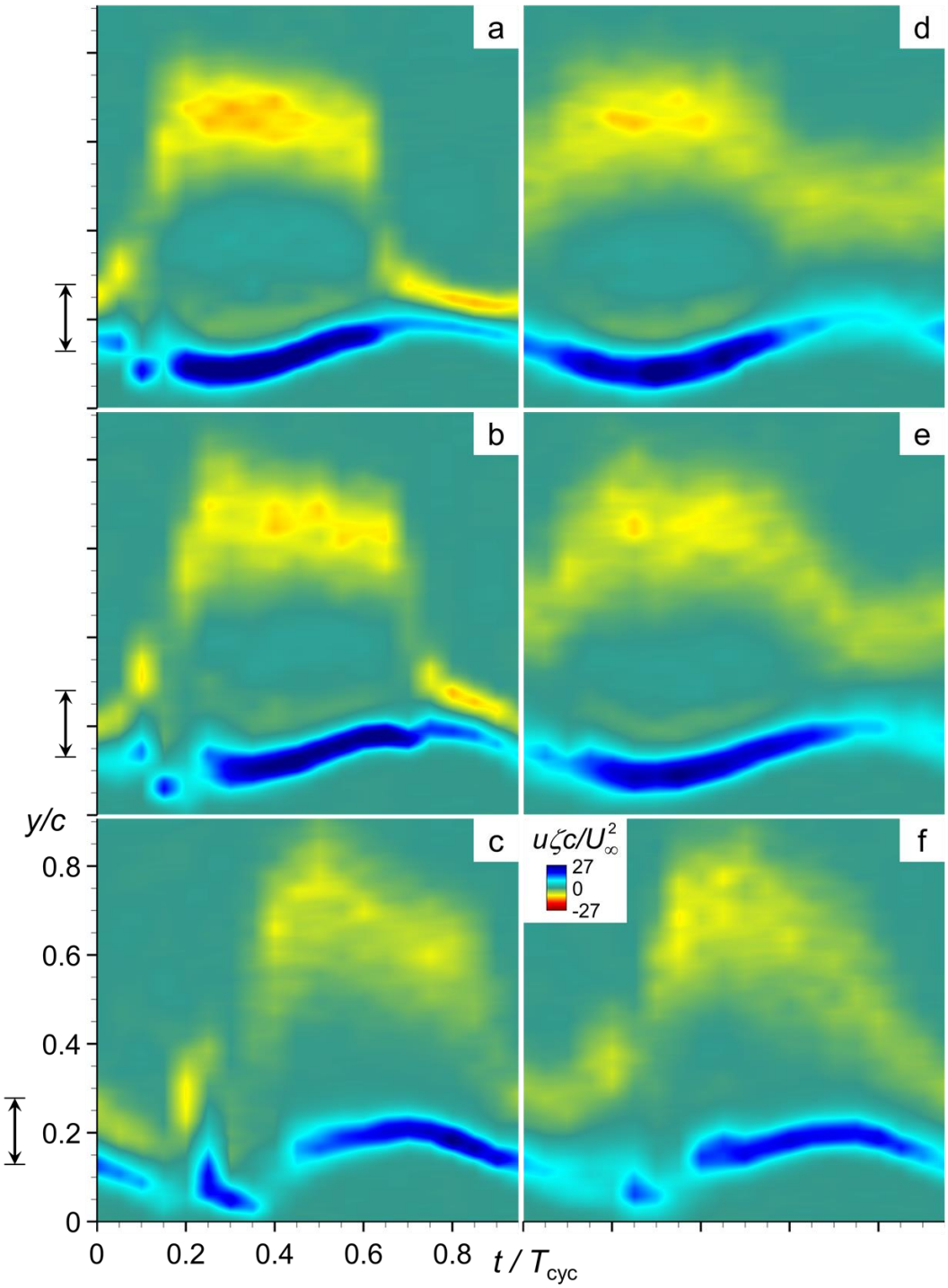

Figure 5.15. Cross stream distributions of the streamwise flux of spanwise vorticity measured 0.3*c* downstream from the trailing edge during the pitch cycle $14° < \alpha < 22°$ in the absence (a-c) and presence (d-f) of bleed: $k = 0.08$ (a, c), 0.17 (b, e), and 0.34 (c, f). The excursion of the trailing edge is marked for reference on the *y* axis.

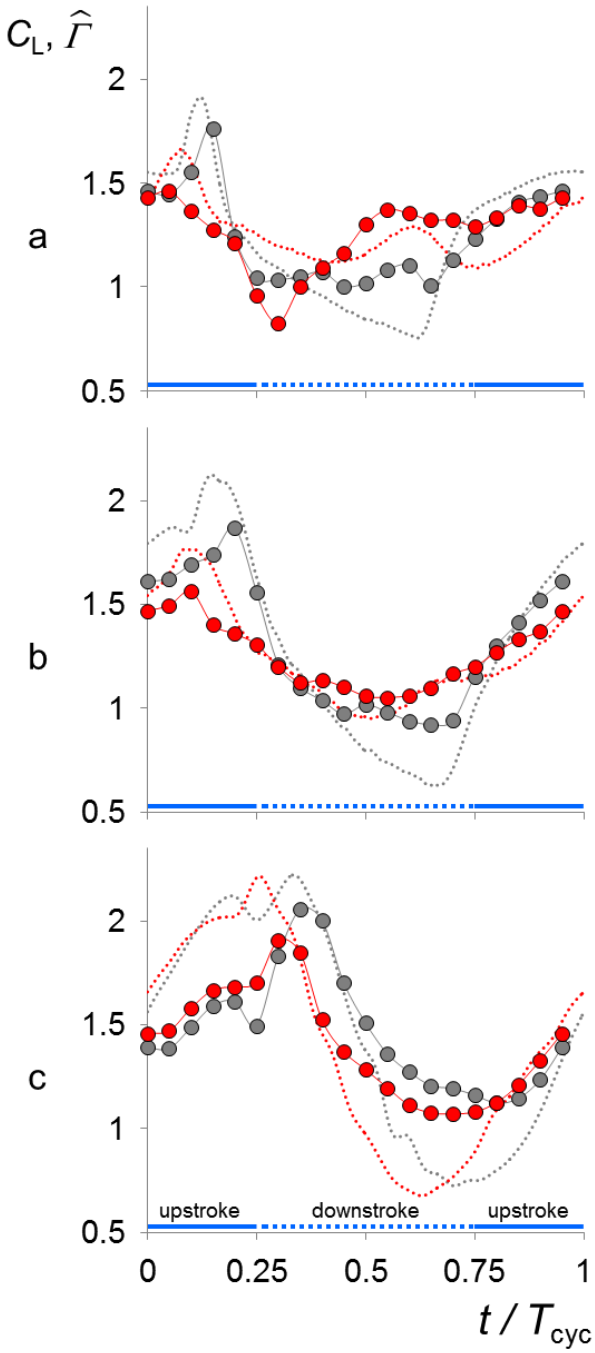

Figure 5.16. Normalized airfoil circulation in the absence (●) and presence (●) of time-periodic bleed actuation ($St_{act} = 1.1$) during the pitch cycle $14° < \alpha < 22°$ at $k = 0.08$ (a), 0.17 (b), and 0.34 (c). Corresponding phase-averaged measurements of C_L for the base flow (gray) and in the presence of bleed (red) are shown using dotted lines.

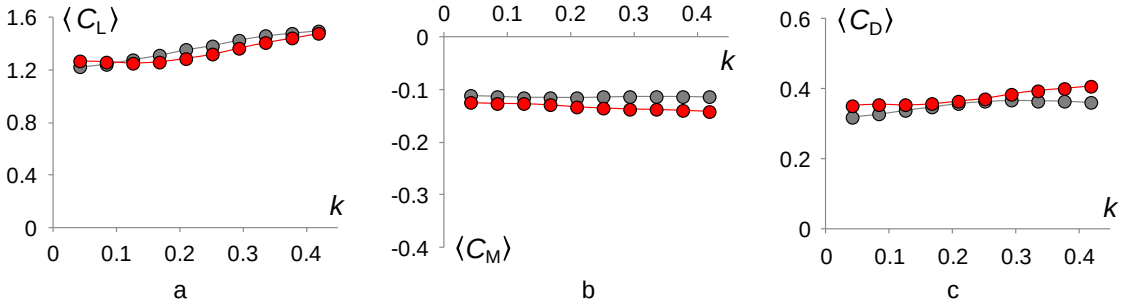

Figure 5.17. Variation of cycle-averaged C_L (a), C_M (b), and C_D (c) with reduced frequency for the base airfoil (●) and time-periodic bleed actuation (St_{act} = 1.1, ●) for oscillations within 14° < α < 22°.

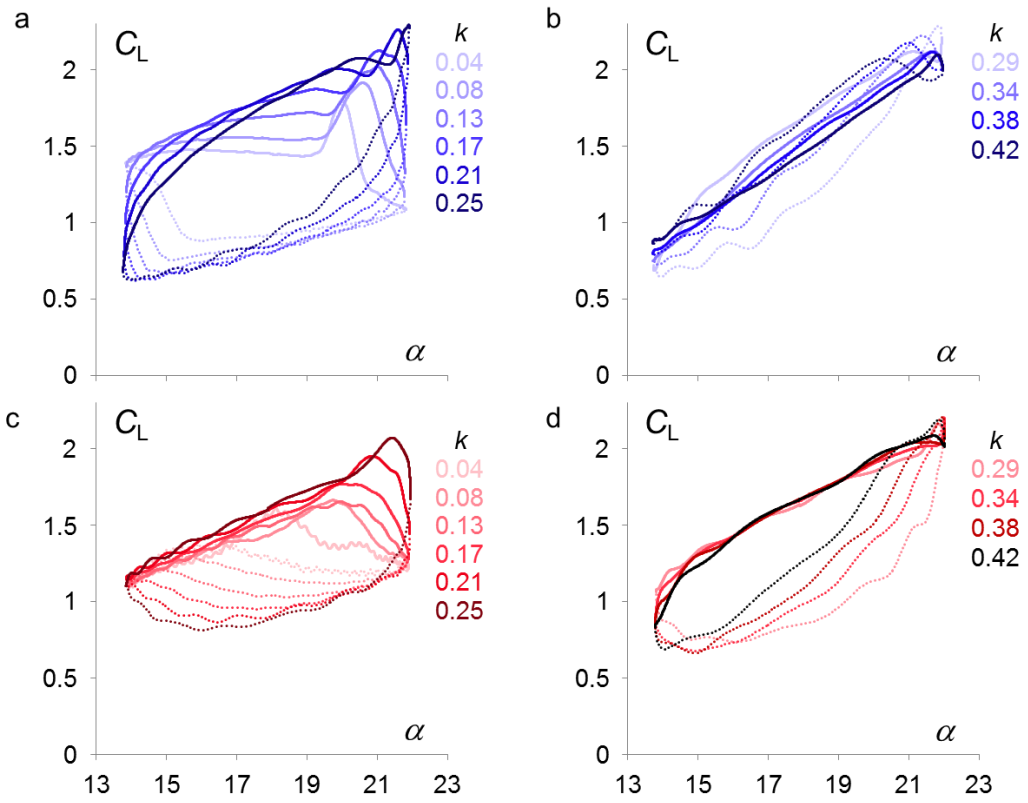

Figure 5.18. Variation of C_L with angle of attack for the base airfoil (top row) and with time-periodic bleed ($St_{act} = 1.1$, bottom row) for oscillations within $14° < \alpha < 22°$: $0 < k < 0.25$ (a) and $0.29 < k < 0.42$ (b).

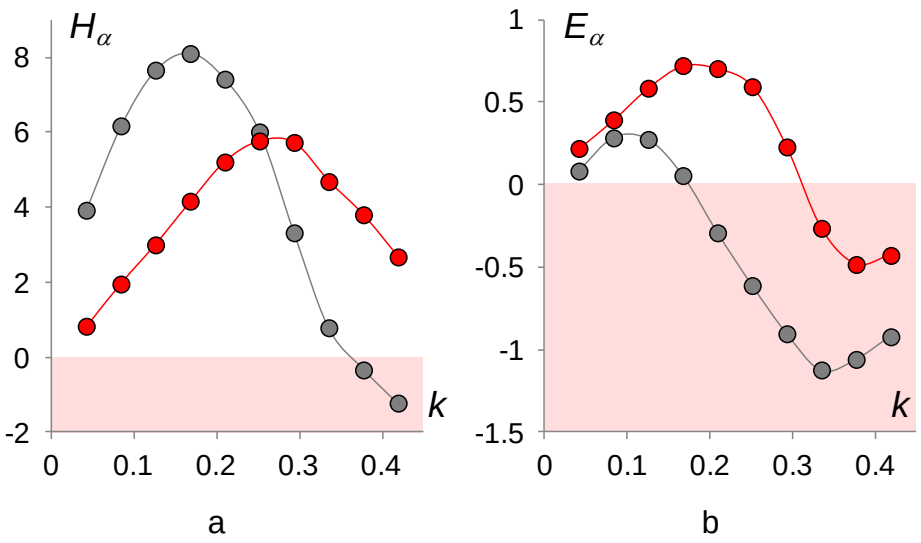

Figure 5.19. Variations in hysteresis (a, negative values shaded red) and damping (b) coefficients for time-periodic pitch oscillations ($14° < \alpha < 22°$) over a range of reduced frequencies: base flow (●) and with time-periodic bleed ($St_{act} = 1.1$, ●).

CHAPTER VI

SUMMARY AND CONCLUSIONS

6.1 Overview

The aerodynamic effects of large-area bleed that is driven through surface openings by the pressure differences across airfoil surfaces are studied with the objective of modifying the aerodynamic loads without external control surfaces. The interactions between the bleed and the cross flow over the airfoil's surface alter the distributions of vorticity concentrations and therefore its apparent aerodynamic shape and aerodynamic forces and moments. Since bleed is driven by the pressure differences between inlet and outlet ports, it is continuously regulated and affected by variations in the angle of attack and by the dynamics of the flow over the surface. The bleed flow can be also time-regulated using externally controlled surface-integrated valves at the inlet or outlet ports. Multiple bleed configurations using different combinations of inlet and outlet ports can be implemented. While the effects of several combinations of such ports on the aerodynamic loads are considered, attention is primarily restricted to combinations of quasi-steady and time-dependent bleed through outlet ports on the suction surface near the leading edge and inlet ports combined with piezoelectric louvers on the pressure surface upstream of the trailing edge.

The effects of the bleed on the outer flow and consequently on the aerodynamic loads are investigated over a range of angles of attack beyond the static stall margin of both static airfoils and on dynamically pitching airfoils. The aerodynamic forces and moments

are measured using load cells. Phase-locked and time-resolved PIV measurements in the cross stream plane over the airfoil are used to investigate the time-dependent evolution of the interactions between the bleed and the cross flows and to resolve the transitory production and advection of vorticity concentrations in the absence and presence of bleed. The measured flow field is also analyzed using proper orthogonal decomposition (POD) to identify the highest energy modes of the flow and to elucidate mechanisms of the evolution and transport of vorticity concentrations. The present investigations demonstrate that bleed actuation alters the production, accumulation, and advection of vorticity concentrations near the surface with significant effects on the evolution, and, in particular, the timing of the dynamic stall vortex. The time-periodic changes in aerodynamic loads during the pitch cycle of an oscillating airfoil can be affected, leading to alteration of lift hysteresis that is accompanied by increased pitch stability.

This chapter presents a brief synopsis followed by concluding remarks for each of the main parts of the present investigation, including bleed actuation at static angles of attack (§6.2) and bleed actuation during pitch oscillations (§6.3). Finally, §6.4 includes some recommendations for future research in bleed-based aerodynamic flow control.

6.2 Bleed Actuation at Static Angles of Attack

6.2.1 Summary

Quasi-steady bleed actuation is used to demonstrate controlled alteration of the aerodynamic forces and moments on static Clark-Y and VR-7 airfoils over a wide range of angles of attack. These changes are effected with relatively low bleed momentum coefficient of $O(10^{-4})$ (estimated from PIV measurements on both airfoils). It is shown that the bleed-induced changes in the aerodynamic loads can be roughly divided to pre-

and post-stall ranges with some overlap as the flow over the base airfoil begins to separate from the trailing edge. For $\alpha < 10°$, measurements on the VR-7 airfoil indicate that louver-regulated quasi-steady bleed can be used to reduce the lift (e.g., by up to $\Delta C_L = 0.21$ or 88% of the base level at $\alpha = 0°$ with an attendant increases in drag of up to $\Delta C_D = 0.04$), and can effectively vary the rate of change lift with α ($dC_L/d\alpha$ between 0.03/° and 0.10/°). At moderate and high angles of attack ($8° < \alpha < 20°$), quasi-steady bleed is manifested by significant decrements in C_L (up to $\Delta C_L = -0.71$ at $\alpha = 16°$ on the Clark-Y and $\Delta C_L = -1$ at $\alpha = 11°$ on the VR-7 airfoils) with a relatively small penalty in drag (up to 0.14). Furthermore, an increase or decrease in the fractional louver opening Λ can decrease or increase the lift, respectively, relative to $\Lambda = 0$, which can enable some of maneuvering for a given bleed configuration. For the Clark-Y airfoil, lift decrements reach nearly $\Delta C_L = -0.5$ relative to $\Lambda = 0$ so that rapid variations in the rate of change of C_L with Λ can be realized (e.g., at $\alpha = 18°$, $dC_L/d\Lambda = -0.26$ for $\Lambda = 0.25$). Quasi-steady bleed enables bi-directional (nose-up or down) changes in C_M at pre-stall (e.g., $-0.06 < \Delta C_M < 0.01$ for the Clark-Y airfoil and $-0.04 < \Delta C_M < 0.06$ and for the VR-7 airfoil at $\alpha = 12°$).

Measurements of pressure distributions (on the Clark-Y airfoil) show that in the presence of quasi-steady bleed, time-averaged trailing edge separation commences at lower angles of attack compared to the base flow, and for a given α over about 10°, the separation migrates upstream with increasing quasi-steady bleed. Therefore, for a given angle of attack, the quasi-steady bleed can be used to bi-directionally displace (upstream or downstream) the location of the time-averaged separation (e.g., at $\alpha = 10°$, an increase in Λ from 0 to 0.5 advances separation from the trailing edge to $x/c = 0.68$). These results

indicate that as long as the flow is not dominated by strong unsteady effects, *prescribed* separation may be maintained as α varies (e.g., separation can be maintained near $x/c = 0.40$ for $12° < \alpha < 16°$ and $0 < \Lambda < 0.5$).

The present investigations demonstrate that the changes in the aerodynamic loads with Λ are associated with corresponding changes in the deflection of the time-averaged surface vorticity layer into the outer flow. In fact, measurements of time-averaged distributions of the streamwise velocity show that the bleed may lead to an inviscid instability rendering the flow extremely susceptible to time-dependent actuation. The characteristic response time scales of the flow to time-dependent actuation are investigated using a step change in quasi-steady bleed actuation. As shown by PIV measurements, at $\alpha = 16°$, step actuation leads to the formation and subsequent advection of the CW vortex and to transitory increases in lift and nose-down moment of $\Delta C_L = 0.31$ and $\Delta C_M = -0.20$ relative to the unactuated flow within $5T_{conv}$ following the onset of bleed.

The receptivity of the flow to time-dependent actuation is exploited for sustained increases in lift and in nose-down moment beyond the levels of the base airfoil to expand the effective operating range of bleed actuation for $\alpha > 14°$. Time-periodic bleed over the range of actuation frequencies $0.13 < St_{act} < 1.6$ (10-120 Hz) leads to a monotonic increase in lift which becomes nearly invariant for $St_{act} > 0.5$ (up to 47% above the base lift at $\alpha = 18°$) with slight reductions in nose-down C_M and in C_D for $St_{act} > 1$ and 1.33, respectively. Static pressure distributions (measured on the Clark-Y airfoil), indicate that time-periodic bleed ($St_{act} = 1.2$) results in both a partial restoration of the leading edge suction peak and increased suction over the majority of the chord relative to base flow.

These changes in C_L and C_M are accompanied by large variations in drag (e.g., up to $-0.27 < \Delta C_D/C_{D,0} < +1.25$ between $4° < \alpha < 8°$) with significant changes in the corresponding lift-to-drag ratio $[-0.94 < \Delta(L/D)/(L/D)_0 < +0.39]$ for some bleed configurations.

6.2.2 Discussion

Quasi-steady and time-periodic bleed modify the aerodynamic loads on an airfoil at static angles of attack by altering the production and spatio-temporal evolution of vorticity concentrations over the suction surface. These effects are assessed in the present work from measurements of the velocity field at pre- and post-stall angles of attack. Time-averaged measurements of the velocity field over the airfoil show that the interaction between the bleed and cross flow leads to proportional, bi-directional deflection of the predominantly CW vorticity layer over the suction surface of the airfoil away from the surface when the base flow is fully attached. In addition, time-dependent actuation can lead to controlled deflection of the vorticity layer when the base flow is partially or fully stalled. This bi-directional deflection is accompanied by significant changes in the thickness and curvature of the vorticity layer and the formation of a thin CCW vorticity layer over the surface as a result of induced (time-averaged) reversed flow.

Considering the relatively low momentum associated with the bleed [the present measurements indicate characteristic speeds of $0.1U_\infty$, and $C_\mu \sim O(10^{-4})$], it appears that its primary function is to *slightly* displace the low-speed (but higher momentum) fluid near the surface of the airfoil by forming a (relatively thin) wall-jet along the surface. The flow appears to be extremely susceptible to the actuation that leads to bifurcation of the CW vorticity layer, ostensibly as a result of induced local changes in the streamwise

pressure gradient, and to its ultimate deflection downstream. The receptivity of the flow may be the result of a local instability owing to the actuation that is associated with the presence of extrema in spanwise vorticity *off the surface*, corresponding to distortion of the time-averaged cross-stream distribution of the streamwise velocity and the appearance of inflection points in $u(y)$ that may be indicative of an inviscid shear layer instability. It is conjectured that the bleed-induced bifurcation and subsequent off-surface deflection of the vorticity layer are the result of amplification of this inviscid instability, similar to the growth of such instabilities in wall jets and free shear layers. In fact, the response of the base flow to time-periodic bleed actuation with non-zero mean that leads to the time-averaged deflection of the detached vorticity layer towards the surface may be related to the same stability mechanism.

The time-averaged vorticity layer does not fully reflect the dynamics of the flow over the surface. Instantaneous concentrations of spanwise vorticity show that the instability associated with the bleed leads to the formation of a train of discrete CW vortices (e.g., nominal passage period $\tau = 0.21T_{\text{conv}}$ or $St = 4.76$ at $\alpha = 3°$). It may be argued that the instability (and hence the formation frequency) is associated with modulation dynamics of the quasi-steady bleed which are affected by changes in the local pressure above the bleed ports. The cross stream scale of these vortices increases with angle of attack ostensibly due to the increase in flux of CW vorticity and in the strength of the actuation, and deflection of the time-averaged vorticity layer from the surface is, in fact, a manifestation of the increase in the cross stream scale of the discrete vortices. It is shown that a step change in bleed by louver activation when the local flow is nominally attached prior to the onset of the actuation leads to the formation of a large-scale CW vortex and

to momentary increases in C_L and in the nose-down C_M ($\Delta C_L = 0.31$ and $\Delta C_M = -0.20$, at $\alpha = 16°$). As the bleed is terminated during the actuation cycle, the vorticity layer collapses onto the surface and the flow becomes attached, and C_L and C_M relax to their original levels. This transient increase in lift can be exploited by repeated, time-periodic actuation ($St_{act} > 0.5$) for sustained changes in the aerodynamic loads. The periodic formation of a train of large-scale vortices that are advected along the surface within 1 to $2T_{conv}$ contribute to the accumulation of CW vorticity over the airfoil and thereby a net increase in lift during the actuation cycle and in the time-averaged lift.

The effects of bleed actuation on the transport of vorticity concentrations over the airfoil are investigated using the streamwise flux of spanwise vorticity concentrations. The time-averaged distributions of the vorticity flux exhibit countercurrent vorticity flux across a domain of upstream flux of CW vorticity that is bounded from above by the streamwise flux of CW vorticity and below by the upstream flux of CCW vorticity. The dynamic effects of time-periodic bleed on the spatial and temporal characteristics of advection of vorticity concentrations over the suction surface and, in particular, the bifurcation of the vorticity layer are analyzed using proper orthogonal decomposition (POD) of the vorticity flux. The first four modes of the base flow (20% of the energy) show that vorticity flux in the absence of bleed is confined to a relatively thin band along the suction surface ($\Delta y/c < 0.1$ for $x/c < 0.5$) associated with vorticity production in the attached boundary layer. In the presence of bleed, the first four modes (29% of the energy) show bifurcated layers associated with countercurrent vorticity flux that advect vorticity upstream and deflect the surface vorticity layer near the leading edge into the cross flow. Reconstruction of the flow using the highest-energy modes captures large-

scale features of the vorticity flux that are not obscured by small-scale motions and reveal the bifurcation of the vorticity layer that leads to the rollup of the large-scale CW vortex and to the accumulation of vorticity as it is advected over the surface.

These findings show that the spatial and temporal modulation of the vorticity flux by controlled bleed that is also partially tuned by the local flow dynamics form the underlying mechanisms for alteration and control of the global aerodynamic forces and moments. This ability to continuously manipulate of the aerodynamic loads can be exploited for aerodynamic maneuvering (e.g., roll by differential spanwise lift), direct lift control (DLC), and airframe stabilization.

6.3 Bleed Actuation during Pitch Oscillations

6.3.1 Summary

The global aerodynamic loads and distributions of vorticity concentrations over an airfoil model (VR-7) undergoing time-periodic pitch oscillations are investigated in the absence and presence of bleed actuation. The dynamic performance of the base airfoil ($-4° < \alpha < 4°$, $0.04 < k < 0.34$) is in good agreement with Theodorsen's (1935) thin airfoil theory despite small deviations due to the airfoil camber. The dynamic loads when the airfoil's oscillations exceed the static stall margin exhibit significant hysteresis in the lift, pitching moment, and drag ($k \sim 0.1$ is a reasonable limit for quasi-steady pitching). For these pitching rates, dynamic stall on the base airfoil is accompanied by increases of up to a 70% in $C_{L,max}$, 190% in nose-down C_M, and 160% in C_D.

The interaction of time-dependent bleed with the cross flow that leads to temporal and spatial modulation of the surface vorticity concentrations and to significant variations in aerodynamic loads is investigated in detail in the quasi-unsteady range ($k = 0.17$).

Dynamic stall on the base airfoil during pitch ($14° < \alpha < 22°$ at $k = 0.17$) causes a rapid rise in C_L (2.12 at $\alpha = 21.0°$) accompanied by a sharp nose-down peak in the pitching moment ($C_M = -0.35$) and followed by a precipitous drop in C_L during the downstroke segment ($\Delta C_L = -0.84$ at $\alpha = 21.5°$ between up and down strokes). However, in the presence of time-periodic bleed ($St_{act} = 1.1$), the aerodynamic loads are significantly different. Although C_L is reduced by $\Delta C_L \approx -0.25$ during the upstroke, the rapid increase in C_L during dynamic stall is muted, and the regulation of shed vorticity during downstroke leads to earlier flow attachment and higher, nearly invariant C_L for $14° < \alpha < 20°$. Furthermore, the rate of change of nose-down C_M with α during upstroke and the maximum nose-down moment are reduced ($dC_M/d\alpha$ and C_M are reduced from -0.19/° to 0.08/° and from -0.35 to -0.30, respectively). Consequently, the stability of the cycle as assessed by the damping coefficient is significantly higher in the presence of bleed ($E_\alpha = 0.72$) than in its absence ($E_\alpha = 0.05$).

The oscillation frequency has significant effects on the aerodynamic loads due to temporal shifts in the formation, advection, and shedding of the dynamic stall vortex and flow reattachment. At $k = 0.08$ and 0.25, as with $k = 0.17$, bleed reduces $C_{L,max}$ during dynamic stall (by $\Delta C_L = -0.23$ and -0.20, respectively) and increases $C_{L,min}$ during the downstroke (by $\Delta C_L = +0.32$ and +0.15, respectively) so that lift hysteresis is reduced compared to the base airfoil. For these pitch rates, *bleed significantly improves the damping coefficient and pitch stability* ($\Delta E_\alpha = 0.10$, 0.67, and 1.21 at $k = 0.08$, 0.17, and 0.25, respectively) leading to CCW variation of $C_M(\alpha)$ and, for a given pitch rate ($k < 0.42$), reducing α at which moment stall occurs. Although the airfoil experiences slightly higher drag during upstroke with bleed, the peak drag is reduced (by $\Delta C_D = -0.15$

and -0.12 at $k = 0.08$ and 0.17, respectively), and drag is typically lower during downstroke than for the base airfoil. These changes are related to the segmentation of the separating shear layer and the shift in timing of vorticity transport during the pitch cycle due to bleed that smooths abrupt transitions in forces and alters the global circulation about the airfoil (discussed below).

Despite the changes in the dynamics of the vorticity concentrations over the airfoil and consequently in vorticity flux during the pitch cycle that lead to alteration of the instantaneous dynamic loads on the base airfoil, variations of the cycle-averaged C_L, C_M, and C_D in the absence and presence of bleed actuation are remarkably small. Bleed produces a slight increment in lift at lower pitch rates [e.g., $\Delta\langle C_L\rangle/\langle C_{L,0}\rangle = 0.04$ at $k = 0.04$] that diminishes with increasing k and that is accompanied by a small increase in drag [$\Delta\langle C_D\rangle/\langle C_{D,0}\rangle = 0.09$] that increases with k. For $k < 0.42$, the average nose-down moment increment is $\Delta\langle C_M\rangle/\langle C_{M,0}\rangle = -0.17$ relative to the base airfoil.

The present investigations demonstrate that bleed actuation also leads to significant cyclical alterations of the flow over the airfoil and in its near wake that affect both the cycle's integral measures of the lift hysteresis and of pitch stability. While for the base airfoil, $C_{L,max}$, $\alpha_{CL,max}$, and $dC_L/d\alpha$ increase with k, the dynamic stall $C_{L,max}$ occurs at a lower angle in the presence of bleed, and the nominal $dC_L/d\alpha$ during the upstroke is nearly invariant with k (0.09/° at $k = 0.04$ to 0.11/° at $k = 0.25$). The presence of bleed also diminishes the strong reduction in hysteresis that characterizes the base flow at higher pitch rates ($0.29 < k < 0.42$), and with bleed, C_L remains higher during upstroke than downstroke for $k < 0.42$. These effects profoundly affect the lift hysteresis H_α and the pitch stability of the cycle. In the base flow, H_α increases rapidly with k and has a

local maximum at $k = 0.17$ ($H_\alpha = 8.10$) before decreasing monotonically and even becoming negative for $k > 0.35$. In the presence of bleed, the hysteresis peak is significantly reduced ($H_\alpha = 5.77$) and occurs at higher k (0.25) compared to the base flow. The damping of the base flow is most stable in the quasi-steady range ($E_\alpha = +0.29$ at $k = 0.08$), though stability diminishes with increasing k as moment stall advances to higher α. E_α becomes negative at $k = 0.18$ ($E_{\alpha,\min} = -1.13$ at $k = 0.34$). In the presence of bleed, pitch stability is enhanced with increasing k ($E_{\alpha,\max} = +0.72$ at $k = 0.17$), and the crossover to net negative damping is extended compared to the base airfoil (to $k = 0.31$).

6.3.2 Discussion

The regulation of vorticity concentrations within the surface vorticity layer during pitch oscillations by bleed actuation is exploited to alter the evolution of the dynamic stall vortex during the upstroke segment and the characteristics of flow separation and attachment during the downstroke segment of the pitch cycle. These modifications have a profound impact on integral measures of the cycle lift hysteresis and pitch stability. Time-resolved PIV measurements over the airfoil during pitch at a quasi-unsteady rates ($k = 0.17$) beyond the static stall angle show that the interactions of the bleed with the cross flow during upstroke displace the leading edge vorticity layer from the suction surface and cause streamwise rollup of CW vorticity segments. The production and advection of these discrete vortices disrupt the formation of a single large-scale dynamic stall vortex that, in the absence of bleed, generates destabilizing transient increases in lift and in nose-down pitching moment as it advects over the surface and sheds into the wake. *By mitigating the severity of moment stall and the associated nose-down peak, bleed actuation improves pitch stability*. During the downstroke segment in which the base

airfoil is fully stalled, the bleed-induced segmentation of the vorticity layer leads to the collapse of the vorticity layer onto the suction surface, resulting in earlier flow reattachment than occurs for the base flow, in a nearly invariant C_L, and hence in significant reduction in cycle hysteresis. It is noteworthy that the bleed flow rate [nominal $C_Q \sim O(10^{-4})$] varies significantly during the pitch cycle nearly out of phase with C_L (with a minimum at $C_{L,max}$) and in phase with C_M ($C_Q \approx 4 \cdot 10^{-4}$ at $C_{M,min}$).

The transitory accumulation and shedding of vorticity concentrations during dynamic stall assessed using phase-locked PIV measurements in the wake are markedly different in the absence and presence of time-periodic bleed. The base flow sheds concentrated layers of CW and CCW vorticity from the suction and pressure surfaces, respectively, during the upstroke prior to dynamic stall, while bleed results in a nearly three-fold increase in the cross stream spreading of the CW domain. Furthermore, the outer layers of streamwise flux of CW and CCW vorticity bound inner layers of upstream flux of alternating sense that contribute to the time rate of change of circulation and appear to scale with the overall width of the wake. Moment stall corresponds to a counterclockwise rotation of the inner layers of wake flux in the base flow but to a gradual cross stream migration of the flux in the presence of bleed, mitigating the rate of change of pitching moment. Dynamic stall is accompanied on the base airfoil by a sharp transition to fully separated flow and an increase in the strength of the inner layer of upstream flux of CW vorticity. With bleed, however, the streamwise segmentation of the shear layer over the surface diffuses the abrupt transition in shed vorticity and therefore in the pitching moment, thus improving pitch stability. During reattachment on the downstroke, streamwise flux of CCW vorticity from the base airfoil becomes intense,

vectored downward, and elongated across the wake while the cross stream width of the wake in the presence of bleed collapses gradually. These topological changes in the flux are accompanied by differences in the rates of increase in lift between the base flow and the (much slower rate) in the presence of bleed ($dC_L/d\alpha \approx 0.96/°$ compared to 0.09/°). These findings are corroborated by POD analysis of the time-resolved vorticity flux in the wake that highlights the shift in timing of vorticity transport in the presence of bleed and further emphasizes the ability of bleed to temporally modulate the flux and affect the global circulation about the airfoil and aerodynamic loads.

The shift in the timing of vorticity production and shedding in the presence of bleed is assessed by considering instantaneous cross stream distributions of the spanwise vorticity and velocity vectors over the airfoil during the pitch cycle. That bleed alters the formation of the dynamic stall vortex that is manifested by CCW variation of $C_M(\alpha)$ and a reduction in the angle at which moment stall occurs (for $k < 0.42$), indicating increased pitch stability. At $k = 0.08$, the temporal variations in the surface pressure distribution associated with the regulation of the vorticity flux by the bleed lead to significant reduction in the rate and magnitude of the nose-down C_M associated with moment stall ($dC_M/d\alpha \approx -0.1/°$ compared to -0.25/° in the absence of bleed), which is also accompanied by a decrease in the magnitude and CCW hysteresis of the nose-down C_M and by improved pitch stability. As the reduced frequency is increased to $k = 0.17$, the flow in the presence of bleed appears to be very similar to the base flow, except that the induced vorticity concentration occurs somewhat earlier in the pitch cycle. However, unlike the base flow, at the end of the downstroke, the flow in the presence of bleed is nearly fully attached. When $k = 0.25$, the distribution of the spanwise vorticity shows

further evidence of segmentation and thereby regulation of the accumulation and advection of vorticity concentrations that also helps attachment earlier in the downstroke and contributes to positive pitch stability.

Analysis of cross stream distributions of vorticity flux show that sharp discontinuities in the wake of the base airfoil owing to the shedding of the precursor and dynamic stall vortices and abrupt reattachment on the downstroke are virtually eliminated in the presence of bleed. The abrupt excursion of CW flux in the base wake as a result of the shedding of the dynamic stall vortex, is significantly smoothed with bleed, and its cross stream width is considerably more uniform during the cycle. The delay in the onset of dynamic stall in the base flow as the pitch frequency increases, evidenced by the sharp excursion in cross stream extent in CW flux during upstroke, is manifested by a phase delay in the shedding of vorticity flux during the pitch cycle by $\Delta t/T_{cyc} \approx 0.10$. The global effects that are investigated by evaluating the phase-locked circulation about the airfoil corroborate the phase shift due to bleed. In particular, vorticity accumulation due to dynamic stall occurs earlier in the pitch cycle in the presence of bleed and with no discernible peak, and circulation recovery during the downstroke occurs considerably faster than for the base airfoil. Although the effects of the actuation on the lift and circulation are somewhat more subtle when the pitch frequency is increased to $k = 0.34$, bleed leads to an overall reduction in the *variation* of circulation during the pitch cycle, and there is a still strong effect on the pitching moment and pitch stability.

These effects of bleed actuation, namely, reduction in moment stall α, disruption of the formation of the dynamic stall vortex, and promotion of early flow reattachment, smooth the abrupt transitions in forces and in shed vorticity, lead to improved stability of

the pitch cycle, and reduce hysteresis. Furthermore, that the present actuation timing and port configurations are not specifically tuned for these effects suggests that further improvements are possible. Other excitation programs (not presented here) including asynchronous bleed pulsing and combinations of quasi-steady and time-periodic actuation show that bleed may be used for control of specific aspects of the pitch cycle (e.g., mitigation of the sharp nose-down spike in C_M) for more efficient aerodynamic control.

6.4 Recommendations for Future Work

The findings of this thesis lay the basis for future investigations of distributed active bleed in a number of areas:

- *Closed-loop control of aerodynamic forces and moments*

  As demonstrated in the present work, bleed has the capability to control aerodynamic forces and moments relative to a trimmed operating point and could therefore be implemented in a closed-loop control system to prescribe aerodynamic maneuvers (e.g., pitch, roll, yaw) or suppress or induce aeroelastic behavior. Such investigations would require suitable sensors (e.g., surface pressure or shear sensors to detect load thresholds or the degree of flow attachment) and control logic. Advances in louver technology (e.g., miniaturization, enhanced flexibility) and improvements to louver integration within the surface skin could enable faster time response and dynamic switching between bleed inlet and outlet locations for a wider range of control authority.

- *Thrust augmentation*

  Airfoil oscillations at sufficiently high rates have been shown to generate thrust

via the Knoller-Betz effect (e.g., Platzer et al., 2008). Given the range of unsteadiness demonstrated in the present work, bleed holds potential for artificially inducing a reverse von Kármán street of vortices to shed and modulating their strength, sense, and formation location along the chord or span. Such an approach may be suitable for small-scale vehicles that utilize flapping-wing (or fin) aero or hydrodynamics for locomotion.

- *Extension to other geometries and flow conditions*

  The scope of the present experiments is limited to active bleed on a two-dimensional airfoil in subsonic flow at a moderate Reynolds number; however, the concept of vorticity regulation using active bleed is clearly not limited to low speeds. The bleed flow rate depends on the pressure difference between inlet and outlet ports and thus scales with Reynolds number, although these effects were not assessed in the current investigations. Further study of bleed actuation in compressible flow and on other geometries can contribute to the control of rotorcraft blades, munitions wings or bodies, re-entry spacecraft, etc. (quasi-steady bleed has already been demonstrated on parafoils, e.g., Gavrilovski, Ward, and Costello, 2012). Bleed actuation could also be combined with miniature obstructions (e.g., DeSalvo and Glezer, 2007) to trap and manipulate vorticity concentrations for aerodynamic control.

APPENDIX A

AIRFOIL AND PRESSURE PORT COORDINATES

Table A.1. Coordinates for the Clark-Y airfoil profile.

x/c	*y/c*	*x/c*	*y/c*	*x/c*	*y/c*
0	0	0.66	0.067605	0.64	-0.01382
0.0005	0.002339	0.68	0.064584	0.62	-0.01456
0.001	0.003727	0.7	0.061433	0.6	-0.01529
0.002	0.005803	0.72	0.05816	0.58	-0.01602
0.004	0.008924	0.74	0.054767	0.56	-0.01676
0.008	0.013735	0.76	0.051257	0.54	-0.01749
0.012	0.017858	0.78	0.047628	0.52	-0.01823
0.02	0.025374	0.8	0.043884	0.5	-0.01896
0.03	0.033022	0.82	0.040024	0.48	-0.0197
0.04	0.039128	0.84	0.036054	0.46	-0.02044
0.05	0.044275	0.86	0.031974	0.44	-0.02117
0.06	0.048757	0.88	0.027789	0.42	-0.0219
0.08	0.056431	0.9	0.023502	0.4	-0.02263
0.1	0.062998	0.92	0.019116	0.38	-0.02336
0.12	0.06862	0.94	0.014624	0.36	-0.02409
0.14	0.073436	0.96	0.010023	0.34	-0.02482
0.16	0.077571	0.97	0.007687	0.32	-0.02556
0.18	0.081069	0.98	0.005333	0.3	-0.02631
0.2	0.08392	0.99	0.002969	0.28	-0.02707
0.22	0.086143	1	0.000599	0.26	-0.02782
0.24	0.087831	1	-0.0006	0.24	-0.02852
0.26	0.089084	0.99	-0.00097	0.22	-0.02915
0.28	0.090002	0.98	-0.00133	0.2	-0.02967
0.3	0.09068	0.97	-0.0017	0.18	-0.03005
0.32	0.091186	0.96	-0.00207	0.16	-0.03026
0.34	0.091508	0.94	-0.0028	0.14	-0.03024
0.36	0.091627	0.92	-0.00354	0.12	-0.02996
0.38	0.091521	0.9	-0.00427	0.1	-0.02938
0.4	0.091171	0.88	-0.00501	0.08	-0.02846
0.42	0.090566	0.86	-0.00574	0.06	-0.02713
0.44	0.089718	0.84	-0.00648	0.05	-0.02605
0.46	0.088643	0.82	-0.00721	0.04	-0.02452
0.48	0.087357	0.8	-0.00794	0.03	-0.02261
0.5	0.085877	0.78	-0.00868	0.02	-0.02027
0.52	0.084214	0.76	-0.00941	0.012	-0.01697
0.54	0.082371	0.74	-0.01015	0.008	-0.01429
0.56	0.080348	0.72	-0.01088	0.004	-0.01051
0.58	0.078145	0.7	-0.01162	0.002	-0.00781
0.6	0.075763	0.68	-0.01235	0.001	-0.00594
0.62	0.073206	0.66	-0.01309	0.0005	-0.00467
0.64	0.070482				

Table A.2. Coordinates for the VR-7 airfoil profile.

x/c	y/c	x/c	y/c	x/c	y/c
0	0	0.08521	0.05937	0.50597	0.07975
0.00001	0.0013	0.08963	0.0608	0.51609	0.0785
0.00007	0.00259	0.09425	0.06224	0.52624	0.0772
0.00017	0.00387	0.09908	0.06367	0.53641	0.07584
0.00034	0.00514	0.10414	0.06509	0.5466	0.07443
0.00055	0.0064	0.10945	0.06649	0.55682	0.07297
0.00083	0.00765	0.11501	0.06788	0.56706	0.07145
0.00116	0.00888	0.12082	0.0693	0.57733	0.06987
0.00156	0.01011	0.12688	0.07075	0.58766	0.06823
0.00203	0.01131	0.13317	0.0722	0.59805	0.06656
0.00256	0.01251	0.13968	0.07363	0.60851	0.06484
0.00317	0.01369	0.14644	0.07501	0.61903	0.06311
0.00386	0.01485	0.15345	0.07633	0.62959	0.06137
0.00463	0.016	0.16072	0.07763	0.64018	0.05962
0.00549	0.01713	0.16825	0.0789	0.65078	0.05787
0.00643	0.01824	0.176	0.08016	0.6614	0.05612
0.00745	0.01934	0.18395	0.08142	0.67202	0.05438
0.00855	0.02043	0.19205	0.08266	0.68265	0.05262
0.0097	0.02152	0.20029	0.08384	0.69328	0.05085
0.01089	0.02261	0.20867	0.08491	0.70391	0.04907
0.01214	0.0237	0.21721	0.08589	0.71455	0.04729
0.01343	0.02478	0.22589	0.08679	0.7252	0.0455
0.01476	0.02587	0.23472	0.08762	0.73585	0.04373
0.01615	0.02697	0.24365	0.08837	0.74653	0.04196
0.01759	0.02806	0.25267	0.08904	0.75722	0.0402
0.01909	0.02916	0.26178	0.08963	0.76792	0.03844
0.02065	0.03025	0.27098	0.09013	0.77863	0.03668
0.02227	0.03136	0.28026	0.09055	0.78934	0.03491
0.02396	0.03246	0.28961	0.09089	0.80005	0.03315
0.02571	0.03357	0.29903	0.09115	0.81075	0.03138
0.02754	0.03469	0.3085	0.09132	0.82144	0.0296
0.02943	0.03582	0.31801	0.09141	0.83211	0.02784
0.0314	0.03695	0.32757	0.09141	0.84276	0.02607
0.03344	0.03809	0.33719	0.09133	0.85338	0.02431
0.03557	0.03924	0.34689	0.09115	0.86397	0.02256
0.03778	0.04039	0.35667	0.09091	0.87452	0.02081
0.04009	0.04154	0.36652	0.09062	0.88501	0.01906
0.0425	0.04269	0.37641	0.09028	0.89544	0.01732
0.04501	0.04385	0.38629	0.08989	0.90581	0.0156
0.04763	0.04502	0.39616	0.08945	0.9161	0.01389
0.05037	0.04621	0.406	0.08894	0.92631	0.01221
0.05321	0.04743	0.41584	0.08833	0.93642	0.01054
0.05617	0.04868	0.42571	0.08763	0.94642	0.00888
0.05926	0.04995	0.43563	0.08684	0.95629	0.00723
0.06249	0.05124	0.4456	0.08599	0.96602	0.00562
0.06586	0.05255	0.45563	0.08509	0.97558	0.00404
0.06939	0.05387	0.46568	0.08413	0.98493	0.00249
0.07308	0.05522	0.47575	0.08312	0.99406	0.00098
0.07694	0.05658	0.48581	0.08206	1	0
0.08098	0.05796	0.49588	0.08094		

Table A.2. (Continued)

x/c	y/c	x/c	y/c	x/c	y/c
0.98587	-0.00072	0.49603	-0.02572	0.08946	-0.02033
0.9771	-0.00117	0.48631	-0.02616	0.08573	-0.01993
0.96813	-0.00163	0.4766	-0.02657	0.08216	-0.01951
0.959	-0.0021	0.46689	-0.02694	0.07873	-0.01908
0.94972	-0.00257	0.45718	-0.02727	0.07545	-0.01867
0.94031	-0.00305	0.44746	-0.02758	0.07228	-0.0183
0.93079	-0.00353	0.43773	-0.02786	0.06923	-0.01797
0.92117	-0.00402	0.42801	-0.02811	0.06628	-0.01769
0.91148	-0.00451	0.41829	-0.02833	0.06344	-0.01744
0.90172	-0.00501	0.40858	-0.02853	0.06069	-0.01717
0.89191	-0.00552	0.39888	-0.0287	0.05804	-0.01688
0.88205	-0.00603	0.3892	-0.02883	0.05548	-0.01657
0.87216	-0.00653	0.37953	-0.02894	0.053	-0.01625
0.86224	-0.00703	0.36987	-0.029	0.0506	-0.01593
0.8523	-0.00754	0.36021	-0.02902	0.04827	-0.01561
0.84234	-0.00805	0.35055	-0.02901	0.04602	-0.0153
0.83238	-0.00856	0.34087	-0.02897	0.04383	-0.01499
0.82241	-0.00907	0.33118	-0.02891	0.04171	-0.01469
0.81245	-0.00958	0.3215	-0.02883	0.03965	-0.0144
0.80248	-0.01008	0.31182	-0.02874	0.03766	-0.01411
0.79253	-0.01057	0.30217	-0.02864	0.03572	-0.01382
0.78257	-0.01106	0.29256	-0.02853	0.03384	-0.01353
0.77263	-0.01157	0.28301	-0.02842	0.03201	-0.01324
0.76269	-0.01208	0.27355	-0.0283	0.03023	-0.01294
0.75277	-0.0126	0.26418	-0.02816	0.0285	-0.01263
0.74284	-0.01313	0.25492	-0.028	0.02682	-0.01232
0.73292	-0.01365	0.24578	-0.02781	0.02518	-0.012
0.72301	-0.01415	0.23676	-0.0276	0.02358	-0.01168
0.71309	-0.01465	0.22787	-0.02738	0.02203	-0.01135
0.70319	-0.01514	0.21914	-0.02714	0.02052	-0.01102
0.69328	-0.01563	0.21058	-0.0269	0.01905	-0.01068
0.68338	-0.01614	0.20221	-0.02666	0.01761	-0.01034
0.67348	-0.01667	0.19407	-0.02644	0.01621	-0.00999
0.66358	-0.01719	0.18618	-0.02621	0.01485	-0.00962
0.65368	-0.01771	0.17854	-0.02594	0.01352	-0.00924
0.64379	-0.01822	0.17113	-0.02563	0.01222	-0.00885
0.6339	-0.01871	0.16395	-0.02529	0.01095	-0.00843
0.624	-0.0192	0.15702	-0.02496	0.00972	-0.008
0.61412	-0.01969	0.15035	-0.02463	0.00852	-0.00754
0.60423	-0.0202	0.14394	-0.02431	0.00736	-0.00704
0.59435	-0.02072	0.13781	-0.02398	0.00626	-0.0065
0.58448	-0.02124	0.13193	-0.02364	0.00523	-0.0059
0.5746	-0.02176	0.12631	-0.02328	0.00428	-0.00524
0.56474	-0.02227	0.12094	-0.02292	0.0034	-0.00451
0.55487	-0.02276	0.11581	-0.02254	0.00259	-0.00372
0.54502	-0.02325	0.1109	-0.02217	0.00185	-0.00288
0.53517	-0.02374	0.10621	-0.02179	0.00117	-0.00197
0.52534	-0.02424	0.10172	-0.02143	0.00056	-0.00102
0.51554	-0.02474	0.09744	-0.02107		
0.50577	-0.02524	0.09336	-0.02071		

Table A.3. Static pressure port locations on the Clark-Y airfoil model.

Port #	*x/c*	*y/c*
1	0.959	0.011
2	0.903	0.023
3	0.822	0.040
4	0.747	0.054
5	0.685	0.064
6	0.627	0.073
7	0.575	0.079
8	0.515	0.085
9	0.453	0.090
10	0.392	0.092
11	0.332	0.092
12	0.273	0.090
13	0.216	0.086
14	0.159	0.078
15	0.101	0.064
16	0.075	0.055
17	0.049	0.044
18	0.016	0.022
19	0.000	0.000
20	0.029	-0.022
21	0.080	-0.028
22	0.141	-0.030
23	0.228	-0.028
24	0.313	-0.025
25	0.409	-0.022
26	0.509	-0.018
27	0.593	-0.011
28	0.663	-0.008
29	0.726	-0.006
30	0.782	-0.004
31	0.851	-0.006
32	0.899	-0.004

APPENDIX B

EVALUATION OF TWO-DIMENSIONAL FLOW ASSUMPTION

Flow is assumed to be two-dimensional over the airfoil in static and dynamic experiments for the purpose of studying the flow physics, with the magnitude of the streamwise (u) and cross stream (v) velocity components dominating the spanwise component (w). However, the finite width of the test section, presence of the compression endplates, and turbulent nature of the interaction generated from the bleed and the outer flow may introduce finite w. To evaluate the assumption of two-dimensionality, PIV measurements are time-averaged at three spanwise locations in the wake, $z/s = \{0.06, 0.27, 0.48\}$, where z is the spanwise coordinate measured from the airfoil fence, for the airfoil at several static angles of attack. Figure B.1 shows cross stream distributions of u/U_∞ in the wake approximately 0.5c downstream from the trailing edge of the base airfoil at $\alpha = 4°$, 8°, 12°, 16°, and 20° (Figures B.1a-e, respectively; the y/c locations of the trailing edge are marked, and the spanwise positions of the measurement planes are shown schematically at right) and in the presence of time-periodic bleed ($St_{act} = 1.1$) at $\alpha = 12°$, 16°, and 20° (Figures B.1f-h, respectively).

At $\alpha = 4°$, 8°, and 12° (Figures B.1a-c), the deficits in streamwise velocity in the wake due to the presence of the airfoil are nearly identical at $z/s = 0.27$ and 0.48; assuming symmetry about the midspan, flow is essentially spanwise-uniform over at least the domain $0.27 < z/s < 0.73$. The velocity distributions in the $z/s = 0.06$ plane (within 1.4 cm of the airfoil fence in the spanwise direction) at $\alpha = 4°$ and 8° (Figure B.1a-b)

exhibit similar deficits due to the presence of the airfoil but also contain a large deficit from $0.4 < y/c < 0.55$ resulting from the flow's interaction with the airfoil fence. At $\alpha = 12°$, Figure B.1c indicates that the presence of the fence near the $z/s = 0.06$ plane reduces the minimum streamwise velocity by $\Delta u/U_\infty = 0.16$ compared to the $z/s = 0.27$ and 0.48 planes, in addition to spreading the deficit nearly 50% further across the wake ($0.80 < y/c < 2.60$). At $\alpha = 16°$ (Figure B.1d), the domains of velocity deficit indicate that the airfoil is stalled near the fences ($z/s = 0.06$) yet flow remains relatively well attached near the midspan plane ($z/s = 0.48$), with a gradual transition to separation between $z/s = 0.48$ and 0.06. By $\alpha = 20°$ (Figure B.1e), the streamwise velocities at each of the spanwise positions show similar degrees of separation, and each contains a region of recirculating flow near $y/c = 0.20$ with the center plane exhibiting slightly deeper stall than locations closer to the fences.

In the presence of time-periodic bleed at $St_{act} = 1.1$ (Figures B.1f-h), spanwise variations in the distributions of streamwise velocity are again minimal across $0.27 < z/s < 0.48$ and most evident in the region near the airfoil fence. At $\alpha = 12°$ (Figure B.1f), flow in the presence of bleed experiences a time-averaged deficit $\Delta y/c = 0.35$ wide (nearly centered about the trailing edge) across $z/s = 0.27$ and 0.48, while flow in the plane $z/s = 0.27$ demonstrates attachment similar to that of the base airfoil at $\alpha = 12°$ (cf. Figure B.1c), suggesting that the effects of bleed do not propagate across the entire span at this angle of attack. Variations in spanwise planes are reduced through $\alpha = 16°$ and 20° (Figures B.1g-h) as the airfoil stalls, and flow separates essentially uniformly across the span.

Therefore, in the data presented in this thesis, flow field measurements are taken at or

near the midspan to avoid the influence of the fences. Note that the load cell measurements are "blind" to the dimensionality of the flow and simply reflect the net forces on the airfoil.

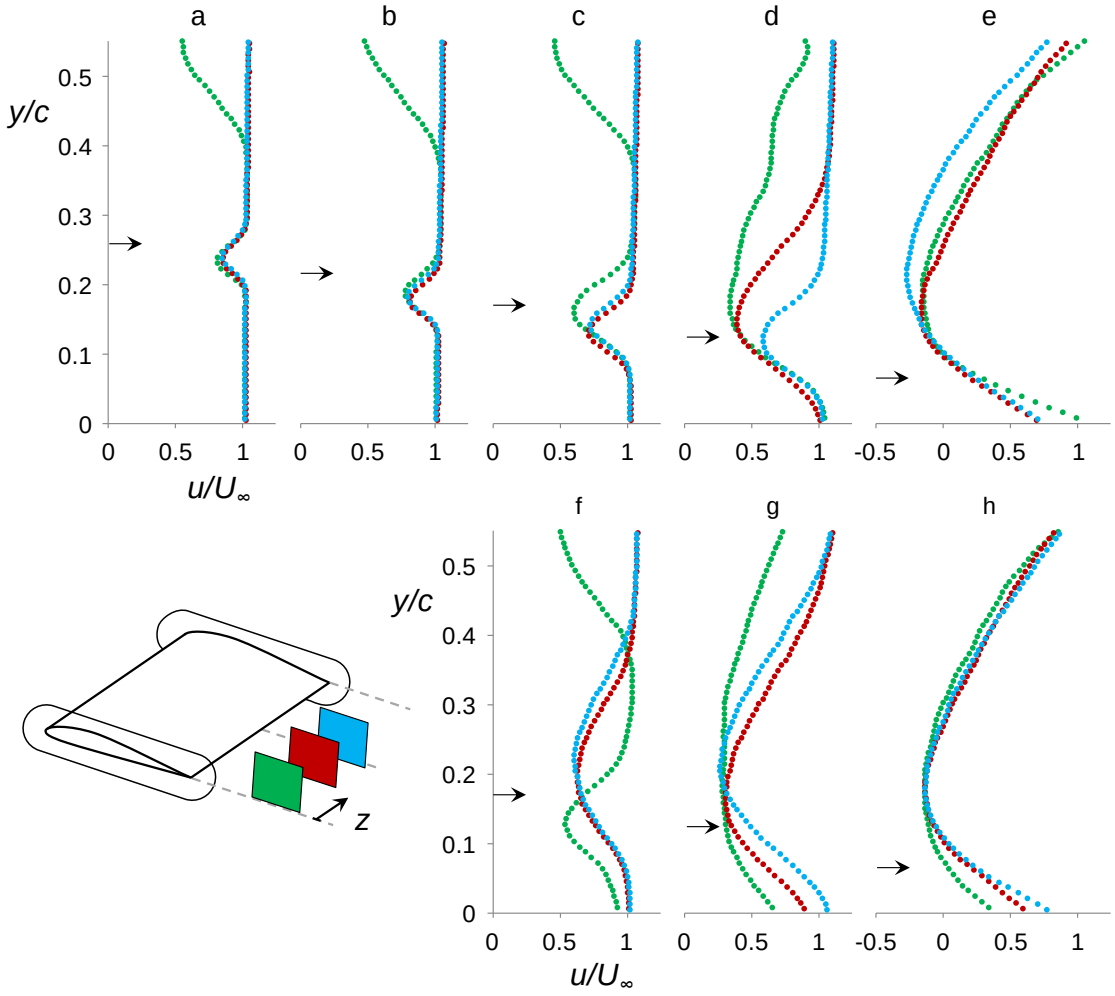

Figure B.1. Cross stream distributions of streamwise velocity in the wake 0.5*c* downstream from the trailing edge at spanwise locations *z*/*s* = 0.06 (●), 0.27 (●), and 0.48 (●) for the base airfoil at $\alpha = 4°$ (a), 8° (b), 12° (c), 16° (d), and 20° (e) and in the presence of time-periodic bleed ($St_{act} = 1.1$) at $\alpha = 12°$ (f), 16° (g), and 20° (g). The elevation of the trailing edge at each α is indicated with a black arrow, and the positions of the measurement planes are shown schematically on the left.

APPENDIX C

TRANSFORMATION OF FORCE DATA REFERENCE FRAME

All force and moment measurements in the present investigations are reported in the (static) wind tunnel reference frame. However, because the load cells are aligned to the airfoil chord such that they rotate with angle of attack, data sampled from each load cell must be transformed to the wind tunnel frame. The transformation for each load cell is determined as follows, with prime and no prime denoting the airfoil reference frame and wind tunnel reference frame, respectively (Figure C.1; note the airfoil is mounted "upside-down" in the wind tunnel to facilitate PIV). A force balance on the "R" side load cell results in:

$$\sum F_{\mathrm{x}} = D = F_{\mathrm{x}}' \cos(\alpha) + F_{\mathrm{y}}' \sin(\alpha) \tag{C.1}$$

$$\sum F_{\mathrm{y}} = L = -F_{\mathrm{x}}' \sin(\alpha) + F_{\mathrm{y}}' \cos(\alpha) \tag{C.2}$$

$$\sum M_{\mathrm{z}} = M_{\mathrm{z}} = M_{\mathrm{z}}' \tag{C.3}$$

where D is drag, L is lift, M_{z} is the moment about the pitch axis, and α is angle of attack. The transformation is to the wind tunnel reference frame is

$$\begin{bmatrix} \cos(\alpha) & \sin(\alpha) & 0 & 0 & 0 & 0 \\ -\sin(\alpha) & \cos(\alpha) & 0 & 0 & 0 & 0 \\ 0 & 0 & 1 & 0 & 0 & 0 \\ 0 & 0 & 0 & \cos(\alpha) & \sin(\alpha) & 0 \\ 0 & 0 & 0 & -\sin(\alpha) & \cos(\alpha) & 0 \\ 0 & 0 & 0 & 0 & 0 & 1 \end{bmatrix} \begin{bmatrix} F_{\mathrm{x}}' \\ F_{\mathrm{y}}' \\ F_{\mathrm{z}}' \\ M_{\mathrm{x}}' \\ M_{\mathrm{y}}' \\ M_{\mathrm{z}}' \end{bmatrix} = \begin{bmatrix} F_{\mathrm{x}} \\ F_{\mathrm{y}} \\ F_{\mathrm{z}} \\ M_{\mathrm{x}} \\ M_{\mathrm{y}} \\ M_{\mathrm{z}} \end{bmatrix} \tag{C.4}$$

For the "L" side load cell, which is mounted in mirror orientation to "R,"

$$\sum F_{\mathrm{x}} = D = F_{\mathrm{x}}' \cos(\alpha) - F_{\mathrm{y}}' \sin(\alpha) \tag{C.5}$$

$$\sum F_{\mathrm{y}} = L = -F_{\mathrm{x}}' \sin(\alpha) - F_{\mathrm{y}}' \cos(\alpha) \tag{C.6}$$

$$\sum M_{\mathrm{z}} = M_{\mathrm{z}} = -M_{\mathrm{z}}' \tag{C.7}$$

and its transformation is

$$\begin{bmatrix} \cos(\alpha) & -\sin(\alpha) & 0 & 0 & 0 & 0 \\ -\sin(\alpha) & -\cos(\alpha) & 0 & 0 & 0 & 0 \\ 0 & 0 & -1 & 0 & 0 & 0 \\ 0 & 0 & 0 & \cos(\alpha) & -\sin(\alpha) & 0 \\ 0 & 0 & 0 & -\sin(\alpha) & -\cos(\alpha) & 0 \\ 0 & 0 & 0 & 0 & 0 & -1 \end{bmatrix} \begin{bmatrix} F_{\mathrm{x}}' \\ F_{\mathrm{y}}' \\ F_{\mathrm{z}}' \\ M_{\mathrm{x}}' \\ M_{\mathrm{y}}' \\ M_{\mathrm{z}}' \end{bmatrix} = \begin{bmatrix} F_{\mathrm{x}} \\ F_{\mathrm{y}} \\ F_{\mathrm{z}} \\ M_{\mathrm{x}} \\ M_{\mathrm{y}} \\ M_{\mathrm{z}} \end{bmatrix} \tag{C.8}$$

The transformations are applied to the measured forces in real-time to resolve the lift, drag, and pitching moment on the airfoil.

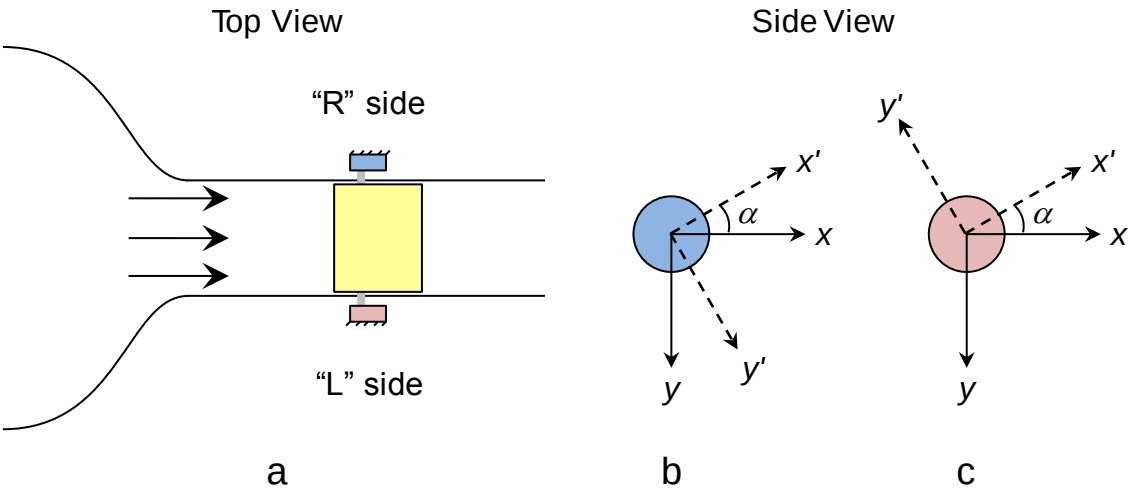

Figure C.1. (a) Top view of the wind tunnel showing the airfoil (yellow) suspended between the load cells ("R," blue, b, and "L," red, c). The wind tunnel and load cells' frames of reference are *x*-*y* (solid lines) and *x*′-*y*′ (dashed lines).

REFERENCES

Abbott, I. H., "Experiments with an Airfoil Model on which the Boundary Layer is Controlled Without the Use of Supplementary Equipment," NACA Technical Note No. 371, 1931.

Abbott, I. H., and von Doenhoff, A. E., *Theory of Wing Sections*, McGraw-Hill Book Company, 1949, reprinted by Dover Publications, Mineola, New York, 1959.

Adrian, R. J., and Westerweel, J., *Particle Image Velocimetry*, Cambridge University Press, New York, New York, 2011.

Amitay, M., and Cohen, J., "Instability of a two-dimensional plane wall jet subjected to blowing or suction," *Journal of Fluid Mechanics*, Vol. 344, 1997, pp. 67–94.

Andersen, P. B., Gaunaa, M., Bak, C., and Hansen, M. H., "A Dynamic Stall Model for Airfoils with Deformable Trailing Edges," *Wind Energy*, Vol. 12, No. 8, 2009, pp. 734–751.

Andrisani, D., Gentry, G. L., and Stickle, J. W., "Wind-Tunnel Study of Slot Spoilers for Direct Lift Control," NASA Technical Note D-6627, 1972.

Bauer, S. X. S., and Hemsch, M. J., "Alleviation of Side Force on Tangent-Ogive Forebodies Using Passive Porosity," *Journal of Aircraft*, Vol. 31, No. 2, 1994, pp. 354–361.

Bisplinghoff, R. L., Ashley, H., and Halfman, R. L., *Aeroelasticity*, Addison-Wesley, 1955, reprinted by Dover Publications, Mineola, New York, 1996.

Bousman, W. G., "Airfoil Dynamic Stall and Rotorcraft Maneuverability," NASA Technical Memo No. 209601, 2000.

Brzozowski, D. P., "Dynamic Control of Aerodynamic Forces on a Moving Platform Using Active Flow Control," PhD Thesis, Georgia Institute of Technology, Department of Mechanical Engineering, 2011.

Brzozowski, D. P., Culp, J. R., Kutay, A. T., Muse, J. A., and Glezer, A., "Closed-Loop Aerodynamic Flow Control of a Free Airfoil," AIAA Paper 2008-4323, 4th Flow Control Conference, Seattle, Washington, 2008.

Carpenter, P., and Porter, L., "Effects of Passive Porous Walls on Boundary-Layer Instability," *AIAA Journal*, Vol. 39, No. 4, 2001, pp. 597–604.

Carr, L. W., "Progress in Analysis and Prediction of Dynamic Stall," *Journal of Aircraft*, Vol. 25, No. 1, 1988, pp. 6–17.

Carr, L. W., Chandrasekhara, M. S., Wilder, M. C., and Noonan, K. W., "The Effect of Compressibility on Suppression of Dynamic Stall Using a Slotted Airfoil," AIAA

Paper 1998-332, 36th Aerospace Sciences Meeting, Reno, Nevada, 1998.

Carta, F. O., "An Analysis of the Stall Flutter Instability of Helicopter Rotor Blades," *Journal of the American Helicopter Society*, Vol. 12, No. 4, 1967, pp. 1–18.

Carta, F. O., Commerford, G. L., and Carlson, R. G., "Determination of Airfoil and Rotor Blade Dynamic Stall Response," *Journal of the American Helicopter Society*, Vol. 18, No. 2, 1973, pp. 31–39.

Chandrasekhara, M. S., Martin, P. B., and Tung, C., "Compressible Dynamic Stall Performance of a Variable Droop Leading Edge Airfoil with a Gurney Flap," AIAA Paper 2004-41, 42nd Aerospace Sciences Meeting, Reno, Nevada, 2004.

Dadone, L. U., "Design and Analytical Study of a Rotor Airfoil," NASA Contractor Report 2988, 1978.

DeSalvo, M. E., and Glezer, A., "Control of Airfoil Aerodynamic Performance using Distributed Trapped Vorticity," AIAA Paper 2007-0708, 45th Aerospace Sciences Meeting, Reno, Nevada, 2007.

DeSalvo, M., Whalen, E., and Glezer, A., "High-Lift Enhancement using Fluidic Actuation," AIAA Paper 2010-0863, 48th Aerospace Sciences Meeting, Orlando, Florida, 2010.

Ericsson, L. E., and Reding, J. P., "Fluid Mechanics of Dynamic Stall Part I. Unsteady Flow Concepts," *Journal of Fluids and Structures*, Vol. 2, No. 1, 1988, pp. 1–33.

Feszty, D., Gillies, E. A., and Vezza, M., "Alleviation of Airfoil Dynamic Stall Moments via Trailing-Edge-Flap Flow Control," *AIAA Journal*, Vol. 42, No. 1, 2004, pp. 17–25.

Florea, R., and Wake, B. E., "Parametric Analysis of Directed-Synthetic Jets For Improved Dynamic-Stall Performance," AIAA Paper 2003-216, 41st Aerospace Sciences Meeting, Reno, Nevada, 2003.

Frink, N. T., Bauer, S. X. S., and Hunter, C. A., "Simulation of Flows with Passive Porosity," International Council of the Aeronautical Sciences (ICAS) Congress, 2002.

Gad-el-Hak, M., *Flow Control: Passive, Active, and Reactive Flow Management*, Cambridge University Press, New York, NY, 2000.

Gardner, A. D., Richter, K., Mai, H., and Neuhaus, D., "Experimental investigation of high-pressure pulsed blowing for dynamic stall control," *CEAS Aeronautical Journal*, Vol. 5, No. 2, 2014, pp. 185–198.

Gavrilovski, A., Ward, M., and Costello, M., "Parafoil Control Authority with Upper-Surface Canopy Spoilers," *Journal of Aircraft*, Vol. 49, No. 5, 2012, pp. 1391–1397.

Gerontakos, P., and Lee, T., "Dynamic Stall Flow Control via a Trailing-Edge Flap," *AIAA Journal*, Vol. 44, No. 3, 2006, pp. 469–480.

Greenblatt, D., and Wygnanski, I., "Dynamic Stall Control by Periodic Excitation, Part 1: NACA 0015 Parametric Study," *Journal of Aircraft*, Vol. 38, No. 3, 2001, pp. 430–438.

Han, Y. O., and Leishman, J. G., "Investigation of Helicopter Rotor-Blade-Tip-Vortex Alleviation Using a Slotted Tip," *AIAA Journal*, Vol. 42, No. 3, 2004, pp. 524–535.

Heine, B., Mulleners, K., Joubert, G., and Raffel M., "Dynamic Stall Control by Passive Disturbance Generators," *AIAA Journal*, Vol. 51, No. 9, 2013, pp. 2086–2097.

Ho, C.-M., and Huerre, P., "Perturbed Free Shear Layers," *Annual Review of Fluid Mechanics*, Vol. 16, 1984, pp. 365–424.

Ho, S., Nassef, H., Pornsinsirirak, N., Tai, Y.-C., and Ho, C.-M., "Unsteady Aerodynamics and Flow Control for Flapping Wing Flyers," *Progress in Aerospace Sciences*, Vol. 39, No. 8, 2003, pp. 635–681.

Honohan, A. M., "The Interaction of Synthetic Jets with Cross Flow and the Modification of Aerodynamic Surfaces," PhD Thesis, Georgia Institute of Technology, Department of Mechanical Engineering, 2003.

Hu, T., Wang, Z., and Gursul, I., "Passive Control of Self-Induced Roll Oscillations Using Bleed," AIAA Paper 2014-1266, 52nd Aerospace Sciences Meeting, National Harbor, Maryland, 2014.

Huerre, P., and Monkewitz, P. A., "Absolute and convective instabilities in free shear layers," *Journal of Fluid Mechanics*, Vol. 159, 1985, pp. 151–168.

Hunter, C. A. Viken, S. A., Wood, R. M., and Bauer, S. X. S., "Advanced Aerodynamic Design of Passive Porosity Control Effectors," AIAA Paper 2001-0249, 39th AIAA Aerospace Sciences Meeting, Reno, Nevada, 2001.

Jategaonkar, R. V., "Identification of Actuation System and Aerodynamic Effects of Direct-Lift-Control Flaps," *Journal of Aircraft*, Vol. 30, No. 5, 1993, pp. 636–643.

Johnson, W., and Ham, N. D., "On the Mechanism of Dynamic Stall," *Journal of the American Helicopter Society*, Vol. 17, No. 4, 1972, pp. 36–45.

Joo, W., Lee, B., Yee, K., and Lee, D., "Combining Passive Control Method for Dynamic Stall," *Journal of Aircraft*, Vol. 43, No. 4, 2006, pp. 1120–1128.

Joslin, R. D., and Miller, D. N., *Fundamentals and Applications of Modern Flow Control*, Progress in Astronautics and Aeronautics Volume 231, AIAA, Reston, Virginia, 2009.

Kearney, J. M., and Glezer, A., "Aero-Effected Flight Control Using Distributed Active Bleed," AIAA Paper 2011-3099, 41st Fluid Dynamics Conference, Honolulu, Hawaii, 2011.

Kearney, J. M., and Glezer, A., "Aerodynamic Control using Distributed Bleed," AIAA Paper 2012-3246, 6th Flow Control Conference, New Orleans, Louisiana, 2012a.

Kearney, J. M., and Glezer, A., "Active Flight Control using Distributed Bleed," 52nd Israel Annual Conference on Aerospace Sciences (IACAS), Tel Aviv and Haifa, Israel, 2012b.

Kearney, J. M., and Glezer, A., "Aerodynamic Control of a Pitching Airfoil using Distributed Active Bleed," 8th International Symposium on Turbulence and Shear Flow Phenomena (TSFP), Poitiers, France, 2013a.

Kearney, J. M., and Glezer, A., "Aero-Effected Control of a Pitching Airfoil by Bleed Actuation," AIAA Paper 2013-2519, 31st Applied Aerodynamics Conference, San Diego, California, 2013b.

Kearney, J. M., and Glezer, A., "Aerodynamic Control by Regulation of Surface Vorticity Flux using Active Bleed," 10th ERCOFTAC Symposium on Engineering, Turbulence, Modelling, and Measurements (ETMM), Marbella, Spain, 2014a.

Kearney, J. M., and Glezer, A., "Aerodynamic Control of a Pitching Airfoil by Active Bleed," AIAA Paper 2014-2045, 32nd Applied Aerodynamics Conference, Atlanta, Georgia, 2014b.

Kraushaar, S., and Chokani, N., "Afterbody Separation Control Using Passive Porosity," AIAA Paper 1997-3003, 33rd Joint Propulsion Conference, Seattle, Washington, 1997.

Krzysiak, A., "Control of Flow Separation Using Self-Supplying Air-Jet Vortex Generators," *AIAA Journal*, Vol. 46, No. 9, 2008, pp. 2229–2234.

Lachmann, G. V., *Boundary Layer and Flow Control: Its Principles and Application, Volume 1*, Pergamon Press, New York, New York, 1961.

Lachmann, G., "Experiments with Slotted Wings," NACA Technical Note No. 71, 1921.

Lachmann, G., "Results of Experiments with Slotted Wings," NACA Technical Memo No. 282, 1924.

Lee, T., and Gerontakos, P., "Investigation of flow over an oscillating airfoil," *Journal of Fluid Mechanics*, Vol. 512, 2004, pp. 313–341.

Leishman, J. G., "Dynamic Stall Experiments on the NACA 23012 aerofoil," *Experiments in Fluids*, Vol. 9, No. 1-2, pp. 49–58.

Leishman, J. G., *Principles of Helicopter Aerodynamics*, Second Edition, Cambridge University Press, New York, New York, 2006.

Liiva, J., "Unsteady Aerodynamic and Stall Effects on Helicopter Rotor Blade Airfoil Sections," *Journal of Aircraft*, Vol. 6, No. 1, 1969, pp. 46–51.

Lopera, J., Ng, T. T., and Patel, M. P., "Experimental Investigations of Reconfigurable

Porosity for Aerodynamic Control," AIAA Paper 2004-3695, 2nd Flow Control Conference, Portland, Oregon, 2004.

Mai, H., Dietz, G., Geißler, G., Richter, K., Bosbach, J., Richarch, H., et al., "Dynamic Stall Control by Leading Edge Vortex Generators," *Journal of the American Helicopter Society*, Vol. 53, No. 1, 2008, pp. 26–36.

Marpu, R. P., Sankar, L. N., Makinen, S. M., Egolf, T. A., Baeder, J. D., Wasikowski, M., "Physics-Based Modeling of Maneuver Loads for Rotor and Hub Design," *Journal of Aircraft*, Vol. 51, No. 2, 2014, pp. 377–389.

Martin, P. B., McAlister, K. W., Chandrasekhara, M. S., and Geissler W., "Dynamic Stall Measurements and Computations for a VR-12 Airfoil with a Variable Droop Leading Edge," AHS International Forum 59, Phoenix, Arizona, 2003.

Martin, P. B., Wilson, J. S., Berry, J. D., Wong, T.-C., and Moulton, M., "Passive Control of Compressible Dynamic Stall," AIAA Paper 2008-7506, 26th Applied Aerodynamics Conference, Honolulu, Hawaii, 2008.

McAlister, K. W., and Carr, L. W., "Water Tunnel Visualizations of Dynamic Stall," *Journal of Fluids Engineering*, Vol. 101, No. 3, 1979, pp. 376–380.

McAlister, K. W., Carr, L. W., and McCroskey W. J., "Dynamic Stall Experiments on the NACA 0012 Airfoil," NASA Technical Paper No. 1100, 1978.

McCroskey, W. J., "The Phenomenon of Dynamic Stall," NASA Technical Memorandum No. 81264, 1981.

McCroskey, W. J., "Unsteady Airfoils," *Annual Review of Fluid Mechanics*, Vol. 14, 1982, pp. 285–311.

McCroskey, W. J., Carr, L. W., and McAlister, K. W., "Dynamic Stall Experiments on Oscillating Airfoils," *AIAA Journal*, Vol. 14, No. 1, 1976, pp. 57–63.

Merat, R., "Study of a Direct Lift Control System Based on the A380 Aircraft," AIAA Paper 2008-1432, 46th AIAA Aerospace Sciences Meeting, Reno, Nevada, 2008

Page, F. H., "Developments in Aircraft Design by the Use of Slotted Wings," *Flight* Magazine, Dec. 22, 1921, pp. 844–861.

Patel, M. P., DiCocco, J. M., Prince, T. S., and Ng, T. T., "Flow Control Using Reconfigurable Porosity," AIAA Paper 2003-3665, 21st Applied Aerodynamics Conference, Orlando, Florida, 2003.

Patil, S. K. R., Ng, T. T., and Patel, M. P., "Trajectory Control of a Small Caliber Projectile Using Active Transpiration," AIAA Paper 2007-3811, 25th Applied Aerodynamics Conference, Miami, Florida, 2007.

Picirrillo, A. C., "The Clark Y Airfoil: A Historical Retrospective," AIAA Paper 2000-

01-5517, World Aviation Conference, San Diego, California, 2000.

Platzer, M. F., Jones, K. D., Young, J., and Lai, J. C. S., "Flapping Wing Aerodynamics: Progress and Challenges," *AIAA Journal*, Vol. 46, No. 9, 2008, pp. 2135–2149.

Post, M. L., and Corke, T. C., "Separation Control Using Plasma Actuators: Dynamic Stall Vortex Control on Oscillating Airfoil," *AIAA Journal*, Vol. 44, No. 12, 2006, pp. 3125–3135.

Raffel, M., Willert, C. E., and Kompenhans, J., *Particle Image Velocimetry, A Practical Guide*, Springer, Berlin, Germany, 1998.

Raghav, V., and Komerath, N., "An Exploration of Radial Flow on a Rotating Blade in Retreating Blade Stall," *Journal of the American Helicopter Society*, Vol. 58, No. 2, 2013, pp. 1–10.

Rainey, G., "Preliminary Study of Some Factors which Affect the Stall-Flutter Characteristics of Thin Wings," NACA Technical Note No. 3622, 1956.

Savu, G., and Trifu, O., "Porous Airfoils in Transonic Flow," *AIAA Journal*, Vol. 22, No. 7, 1984, pp. 989–991.

Schreck, S., and Robinson, M., "Rotational Augmentation of Horizontal Axis Wind Turbine Blade Aerodynamic Response," *Wind Energy*, Vol. 5, No. 2-3, 2002, pp. 133–150.

Simão Ferreira, C., van Kuik, G., van Bussel, G., and Scarano, F., "Visualization by PIV of dynamic stall on a vertical axis wind turbine," *Experiments in Fluids*, Vol. 46, No. 1, 2009, pp. 97–108.

Singh, C., Peake, D. J., Kokkalis, A., Khodagolian, V., Coton, F., and Galbraith, R. A. M^{c}D., "Control of Rotorcraft Retreating Blade Stall Using Air-Jet Vortex Generators," *AIAA Journal*, Vol. 43, No. 4, 2006, pp. 1169–1176.

Sirovich, L., "Turbulence and the dynamics of coherent structures," Parts I-III, *Quarterly of Applied Mathematics*, Vol. 45, No. 3, 1987, pp. 561–571, 573–590.

Tanner, M., "Reduction of Base Drag," *Progress in Aerospace Sciences*, Vol. 16, No. 4, 1975, pp. 369–384.

Theodorsen, T., "General Theory of Aerodynamic Instability and the Mechanism of Flutter," NACA Report No. 496, 1935.

Tinetti, A. F., Kelly, J. J., Bauer, S. X. S., and Thomas, R. H., "On the Use of Surface Porosity to Reduce Unsteady Lift," AIAA Paper 2001-2921, 31st AIAA Fluid Dynamics Conference, Anaheim, California, 2001.

Visbal, M. R., "Numerical Investigation of Deep Dynamic Stall of a Plunging Airfoil," *AIAA Journal*, Vol. 49, No. 10, 2011, pp. 2152–2170.

Weaver, D., McAlister, K. W., and Tso, J., "Control of VR-7 Dynamic Stall by Strong

Steady Blowing," *Journal of Aircraft*, Vol. 41, No. 6, 2004, pp. 1404–1413.

Weick, F. E., and Shortal, J. A., "The Effect of Multiple Fixed Slots and a Trailing Edge Flap on the Lift and Drag of a Clark Y Airfoil," NACA Report No. 427, 1932.

Williams, D. R., and Papazian, H., "Forebody Vortex Control with the Unsteady Bleed Technique," *AIAA Journal*, Vol. 29, No. 5, 1991, pp. 853–855.

Williams, D., El-Khabiry, S., and Papazian, H., "Control of Asymmetric Vortices around a Cone-Cylinder Geometry with Unsteady Base Bleed," AIAA Paper 1989-1004, 2nd Shear Flow Conference, 1989.

Woo, G. T. K., and Glezer, A., "Controlled transitory stall on a pitching airfoil using pulsed actuation," *Experiments in Fluids*, Vol. 54, No. 6, 2013, pp. 1–15.

VITA

John Michael Kearney was born in Washington, D. C. to Mary Grace and Michael Kearney. He grew up a very happy child with his four siblings, James, Elisabeth, Christopher, and Kathryn, in Virginia and New Mexico. He attended Duke University in North Carolina and received B.S. degrees in Mechanical Engineering and Psychology in 2008. That summer, he joined Professor Ari Glezer's Fluid Mechanics Research Laboratory at the Georgia Institute of Technology and began his studies in experimental fluid mechanics and aerodynamics. He earned an M.S. in Mechanical Engineering in 2012. John married his high school sweetheart, Jordan, in 2011, and his family grew by two siblings, Nathan and Paxton (and later, Kristine), and two parents, Carla and Noel. John and Jordan currently live in Atlanta but will soon be moving to California, where John will begin a career in product design and engineering with Apple Inc.